

EUROPEAN COMMISSION

Programme Environment and Climate 1994-1998. Topic 3.1.2

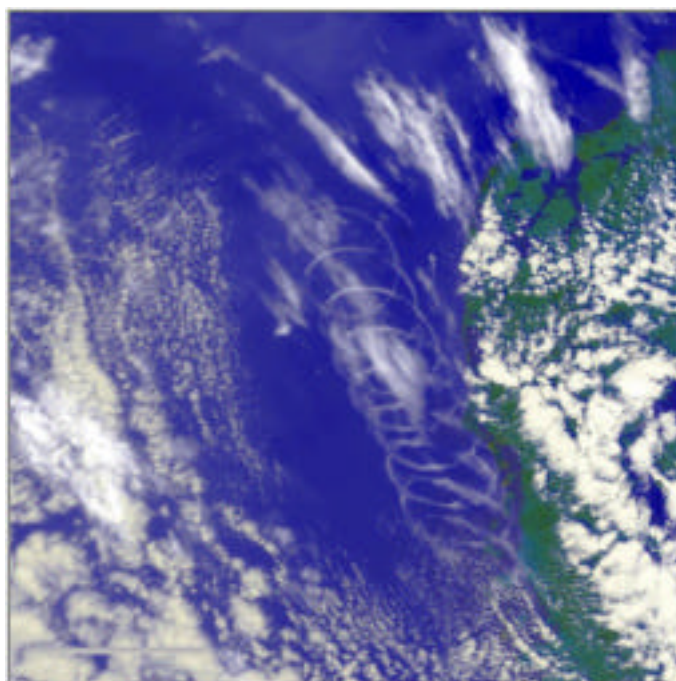
EU Contract no. ENV4 CT97-0399



Cirrus and Contrail cloud-top maps from satellites for
Weather Forecasting and Climate Change Analysis

Second Interim Report

October 1999



Example of aircraft contrails in AVHRR image ©DLR 1998



EXECUTIVE SUMMARY	1
HIGHLIGHTS	1
OBJECTIVES.....	1
CONTEXT	1
OUTLINE OF METHOD	1
PROGRESS TO DATE	2
INTERNAL AND EXTERNAL PUBLICATIONS.....	2
PRELIMINARY CONCLUSIONS.....	4
<i>Progress towards project objectives</i>	4
<i>Implications for the final year</i>	5
INTRODUCTION	5
OBJECTIVES.....	5
CONTEXT	6
BRIEF INTRODUCTION TO THE CLOUDMAP CONSORTIUM.....	6
WORK ACHIEVED OVER THE PERIOD	7
OVERVIEW	7
MILESTONES REACHED	7
PROGRESS BY WORK PACKAGE	7
<i>End user evaluation (KNMI)</i>	7
KNMI Objectives in the Second Year.....	7
Work performed by KNMI.....	8
Assessment of the fulfilment against project objectives	8
Evaluation of ATSR2 CTH maps for the CLARA96 campaign	9
End user evaluation conclusions	18
Project Plan of KNMI activities for the final period	18
<i>Data collection</i>	19
UCL	19
ATSR2 data collection	19
Chilbolton Radar data collection.....	21
Wide-angle sky digital imagery data collection.....	21
Status of the NASA EOS Terra mission	22
AirMISR data acquired during the FIREIII campaign in Alaska	22
DLR-IPE.....	25
Status of the MOSM-PIRODA data collection.....	25
ETH	33
Stereo MOMS data collection.....	33
ATSR2 stereo data collection	35
Ground-based whole-sky stereo digital images	36
MAP Campaign.....	37
DLR-IPA	39
AVHRR data collection over Europe for contrail studies.....	39
ATSR2 data collection over Europe for contrail studies	40
Ground-based data collection for contrail validation.....	40
DLR-IST.....	40
FUB	40
MOS data collection.....	40
Radiosondes	42
<i>Data processing algorithm development and implementation</i>	42
UCL.....	42
ATSR2 Radiance-to-CTH Processing chain.....	42
The stereo matching algorithm	42
The ATSR2 camera model	43
AirMISR Radiance-to-CTH Processing chain.....	44
Deriving heights from AirMISR data (assuming winds=0).....	44
DLR-IPE.....	45
ETH	45
Cloud-Top height from MOMS scenes.....	45
Stereo matching algorithm	49
Camera modelling for ground-based images	49
DLR-IPA	50
AVHRR Contrail detection algorithm implementation	50

CLOUDMAP - Cirrus and Contrail cloud-top maps from satellites for Weather Forecasting and
Climate Change Analysis :Second Interim Report (1998-99)

AVHRR Contrail processing over Europe.....	50
AVHRR Contrail processing over Asia.....	51
Implementation of ATSR2 Contrail detection.....	51
DLR-IST: Decision Directed Estimation of Cirrus and Contrails Based on Property representation by Fuzzy Measures and their Fusion by a Fuzzy Integral.....	53
Introduction.....	53
Contrail Detection.....	53
Difficulties with contrail separation.....	54
Estimation of relevant textural properties.....	54
Pre-processing for contrail detection.....	54
<i>Development of mathematical basis for description of textures</i>	54
<i>Mapping of properties of textures on fuzzy measures and fuzzy function</i>	56
<i>Fusion of fuzzy properties by fuzzy integrals</i>	57
Algorithms for detection of contrails and their present realisation.....	58
Detection of Cirrus clouds.....	59
Algorithms for detection of cirrus clouds and their present realisation.....	60
Open issues and future work.....	60
Example results (no commentary supplied).....	61
Examples of cirrus clouds in MOS images.....	61
Examples of contrail isolation in AVHRR images.....	69
Examples of contrail isolation in MOS images.....	81
Examples of contrail isolation in ATSR 2 images.....	84
FUB.....	87
MOS processing chain.....	87
Level 1b Processor.....	87
Classification algorithm.....	90
Level 2 Processor.....	91
Cloud-top Pressure.....	92
Cloud optical thickness.....	95
Cloud effective radius and cloud droplet concentration.....	98
FUBISS.....	98
Value-added data production.....	99
UCL.....	99
ATSR2 Stereo Cloud-Top Height Maps.....	99
AirMISR Stereo Cloud-top heights.....	100
Stereo measurements of CBH using Fish-eye lens stereo CCD imagery.....	103
DLR-IPE.....	103
Initial experience with Cloud-to-Cloud Matching.....	103
Initial experience with Shadow Matching.....	103
Initial experience with contrail and cirrus matching.....	104
ETH.....	104
DLR-IPA.....	105
Creation of contrail climatology over Europe.....	105
Creation of contrail climatology over non-European areas.....	105
FUB.....	105
Cloud optical thickness regression error.....	105
Validation and scientific evaluation of products.....	109
UCL.....	109
Comparison of ATSR2 CTHs with Chilbolton radar.....	109
Comparison of ground-based CBH with Chilbolton radar.....	109
Comparison of AirMISR CTHs with airborne lidar and ground-based mm-radar.....	110
DLR-IPE.....	112
Validation Plan for the last period.....	112
ETH.....	112
Validation Plan for the last period.....	112
DLR-IPA.....	113
Contrail detection False Alarm Rate.....	113
Validation plans for the last period.....	113
DLR-IST.....	113
FUB.....	113
Comparison of MOS Cloud-top Pressure with radiosonde data.....	113
Validation of cloud droplet concentration.....	115
Departures from Workplan.....	123
PRELIMINARY CONCLUSIONS.....	123
Progress towards project objectives.....	123
Implications for the final period.....	124

CLOUDMAP - Cirrus and Contrail cloud-top maps from satellites for Weather Forecasting and
Climate Change Analysis :Second Interim Report (1998-99)

REFERENCES CITED 125

ANNEX A: REPORT ON THE 2ND CLOUDMAP USER WORKSHOP **126**

Figure 1. August 29 1996. Top: Lidar Bottom Radar	11
Figure 2. August 29 1996. 12Z Radiosonde plot	11
Figure 3. August 29, 1996. METEOSAT CTH (UL), false colour composite using 0.65, 1.6, 11 μm (RGB value).(UR), ATSR 11 μ (LL) and 1.6 μm (LR), A colour bar denotes the CTH scale. White spots indicate areas where the stereo matcher was not able to calculate a height.....	13
Figure 4. September 1, 1996 METEOSAT CTH (UL), false colour composite using 0.65, 1.6, 11 μm (RGB value).(UR), ATSR 11 μ (LL) and 1.6 μm (LR), A colour bar denotes the CTH scale. White spots indicate areas where the stereo matcher was not able to calculate a height.....	14
Figure 5. November 20, 1996 METEOSAT CTH (UL), false colour composite using 0.65, 1.6, 11 μm (RGB value).(UR), ATSR 11 μ (LL) and 1.6 μm (LR), A colour bar denotes the CTH scale. White spots indicate areas where the stereo matcher was not able to calculate a height.....	15
Figure 6: November 29, 1996 METEOSAT CTH (UL), false colour composite using 0.65, 1.6, 11 μm (RGB value).(UR), ATSR 11 μ (LL) and 1.6 μm (LR), A colour bar denotes the CTH scale. White spots indicate areas where the stereo matcher was not able to calculate a height.....	16
Figure 7: September 12, 1996, 10.00 UTC.	17
Figure 8. Left and right views 500m apart taken by the Kodak Megaplus digital cameras of clouds during CLARE98 (23.10.98) showing the effects of differences in contrast, synchronisation and the lack of a sun occulor.....	22
Figure 9. AirMISR Red channel data from An, Af, Aa, Bf, Ba, Cf and Ca reading from left to right and top to bottom.....	24
Figure 10 shows an anaglyph view of a nearly complete anaglyph views (4000 by 4000 pixel out of 5800 by 5920 original image size) of two adjacent MOMS images (23 and 24) of data take T0908 west of Baku with multi-layer cloud fields over land. Figure 10 (left) is combined from channels 1 and 6 and Figure 10 (right) from channels 4 and 7.	28
Figure 11 present similar red/green anaglyph views of three adjacent MOMS images (03 to 05) of data take T08C5 west of the Chilbolton test site in South England. The image 03 shows a single layer field of small Cumuli over land as the dominating feature. The image 05 is dominated by Cirrus type clouds over sea. All images contain aircraft contrails, but the image 04 shows all types of contrails from status nascendi to worn out old ones, mainly in a Cirrus environment over sea. Optically thick clouds are saturated, since the images were stretched to enhance the contrail and Cirrus clouds.	29
Figure 12 shows an anaglyph view of a Cirrus cloud and a persisting contrail over sea. The waves of the sea surface are visible in this image. The example is from image 04 of the data take T08C5.	30
Figure 13 is a side by side presentation of the stereo channels 6 and 7 of a persistent contrail over land casting a clearly visible shadow. The clearly visible displacement of the shadow position within the 40 seconds time interval between the two images by strong winds leads to a 16% difference between the true and the apparent stereo height of this contrail! The example is taken from the MOMS image 16 of the data take T08E2.....	31
Figure 14 are side by side presentations of the stereo channels 6 and 7 of persisting contrails over land and sea casting a clearly visible shadow associated with	

shadow drift. The example is taken from the MOMS image 16 (upper) and 17 (lower) of the data take T08FE 32

Figure 15: MOMS Stereo pair, scenes 25-26. On the left is the aft view, on the right the forward view. The flight direction is from left to right. 34

Figure 16. MOMS sensor on MIR station..... 35

Figure 17: Geometry of MOMS sensor on MIR station. 35

Figure 18: Stereo pair with 18mm lens, 08/08/1999 17:00 GMT; horizontal distance: 800m. Because of the late time of the day, no sun occulter had to be used..... 37

Figure 19: Left: image taken with 18mm lense; right: image taken with 8mm fish-eye lens. Time difference between these two images is 60 seconds..... 37

Figure 20: Sun effects in images without (left) or with (right) a sun occulter..... 37

Figure 21: Target Areas of the Mesoscale Alpine Programme (source: <http://www.map.ethz.ch>) 38

Figure 22. Calendar overview of available and processed AVHRR-HRPT data for 1994 - 1999(valid on Sept. 18 1999). green: already processed, red: not (yet) available, yellow: raw data available in automated archive, dark colours: night passages..... 39

Figure 23: IRS-P3 path map with the radiozone of Neustrelitz, Germany. 41

Figure 24: IRS-P3 path map with the radiozone of Mas Palomas, Canary Island, Spain..... 41

Figure 25: Distribution of GCPs and CPs (in red).. 47

Figure 26: Plot of errors in planimetry for 19 check points. 48

Figure 27: Plot of errors in height for 19 check points. 48

Figure 28: Zooms of saturated areas before (left image) and after (right image) applying the filter. 49

Figure 29: Testfield at ETH for determination of the inner orientation parameters of the cameras..... 50

Figure 30. Stacked Contrails over SE-Asia from 60 scenes in January 1998..... 51

Figure 31. ATSR2 test dataset with contrails (12µm channel) 51

Figure 32. Detected contrails from the nadir view of the test dataset..... 52

Figure 33. Fraction of contrail pixels within the y-displacement classes of different area based matchers: mm and mmm are the UCL matchers, pa is a matcher programmed at DLR-IPA and tuned to handle contrails. All matcher either ignore contrails or overestimate their width..... 53

Figure 34. Cirrus clouds (original MOMS image) where boundaries difficult to see 61

Figure 35. Detection of a cirrus cloud from MOMS with extracted boundary and core 62

Figure 36. Representation of the boundary structure of the cirrus cloud from MOMS 63

Figure 37. Representation and quantification of the boundary of the cirrus cloud from MOMS..... 64

Figure 38. Two different layers of cirrus clouds (original MOMS image)..... 65

Figure 39. Representation of the lower cirrus cloud (blue) from MOMS..... 66

Figure 40. Separation of the upper cirrus cloud (yellow) from MOMS 67

Figure 41. Isolation of no cirrus clouds (green) from MOMS 68

Figure 42. Germany with many contrails (original AVHRR image)..... 69

Figure 43. Isolation of contrails (more flights red) from AVHRR 70

Figure 44. Contrails distinguished by non-linear filtering from AVHRR 71

Figure 45. AVHRR image with contrails (original) from AVHRR..... 72

Figure 46. Enhancement of lines in the AVHRR image	73
Figure 47. Isolation of contrails from AVHRR.....	74
Figure 48. AVHRR image (original).....	75
Figure 49. Separation of clouds by structures (characterised brighter) for masking from AVHRR	76
Figure 50. Characterisation of Baltic Sea by textures (represented brighter) from AVHRR.....	77
Figure 51. Isolated contrails from AVHRR	78
Figure 52. AVHRR of region surrounding Denmark without contrails but small clouds	79
Figure 53. Nearly no contrails are detected from AVHRR.....	80
Figure 54. MOS image original left upper with cloud enhancement and contrail isolation	81
Figure 55. Aged contrails in the middle of the MOS image	82
Figure 56. Examples of enhancement of the structures of aged contrails from MOS	83
Figure 57. Original ATSR2 image (difference image) with contrails.....	84
Figure 58. Enhancement of contrails by differences in stochastic from ATSR2	85
Figure 59. Enhancement of the other region with contrails from ATSR2	86
Figure 60. Isolation of the contrails in the ASTR-image	87
Figure 61: Screenshot of the MOS classification tool for a manual definition of training areas	91
Figure 62. Left: MOS radiance in channel 9 at 750nm. Right: Retrieved cloud top pressure in hPa	92
Figure 63: Sensitivity of the ctp algorithm to cloud optical thickness and surface albedo. A negative BIAS (blue) means overestimation of the cloud top pressure	93
Figure 64: Sensitivity of the ctp algorithm to the error of the surface albedo as a function of the cloud thickness (left) and the surface albedo (right).	94
Figure 65: Sensitivity of the cloud top pressure retrieval to cloud optical thickness and cloud top pressure. The white areas are not represented in the test and training database.....	94
Figure 66: RMSE of cloud optical thickness retrieval as function of cloud optical thickness and cloud top pressure.....	95
Figure 67: BIAS of cloud optical thickness retrieval as function of cloud optical thickness and cloud top pressure.....	96
Figure 68: RMSE of cloud optical thickness retrieval as function of cloud optical thickness and surface albedo	96
Figure 69: BIAS of cloud optical thickness retrieval as function of cloud optical thickness and surface albedo	97
Figure 70: RMSE of cloud optical thickness retrieval as function of cloud optical thickness and instrumental noise.....	97
Figure 71: BIAS of cloud optical thickness retrieval as function of cloud optical thickness and instrumental noise.....	98
Figure 72. ATSR2 stereo-pair (left- nadir, right-forward) acquired on 23.10.98 over the Chilbolton site including a small inset on the nadir around the Chilbolton site.	99
Figure 73. ATSR2 stereo Cloud-Top Heights (left) together with map schematic (right) showing the location of the Chilbolton radar site as a “X”.....	100

Figure 74. Histograms of stereo matched disparities between AnAf, AfAn, AnAa and AaAn	101
Figure 75. Stereo-matched heights from the A and B forward and after cameras showing the bias in the forward CTHs wrt the aft ones.	102
Figure 76: cloud optical thickness retrieval error in percent.....	106
Figure 77: MOS radiance in channel 9 at 750nm.....	107
Figure 78: Retrieved cloud optical thickness	108
Figure 79. Browse products of the Chilbolton 35GHz (top) and GKSS 94 GHz (bottom) radars showing radar reflectivity in dBs for 23.10.98. A visual inspection indicates a CTH around 1km.	109
Figure 80. Stereo-pair of Kodak Megaplus camera images acquired at 11:14Z at the time of the ATSR2 overpass	110
Figure 81. Comparison of stereo-retrieved cloud top height and ER-2 Cloud Lidar System measured cloud top height. Stereo-based results are shown with both the full AirMISR algorithm and M2.	111
Figure 82: The profile of the dew point temperature and the temperature measured by a radio sond for a specific case (left). On the right hand side the corresponding histogram of the retrieved cloud top pressures is shown.....	114
Figure 83: The retrieved cloud top pressures and the corresponding inversion pressures of all cases. The red points are values where the radiosounding was within the MOS track, the gray points are values, where the radiosounding was close to but not within the MOS track.....	115
Figure 84: Retrieved optical thickness from MOS image recorded at March, 4 th 1998	116
Figure 85: Retrieved optical thickness from MOS image recorded at March, 24 th 1998	116
Figure 86: Retrieved cloud top pressure from MOS image recorded at March, 4 th 1998	117
Figure 87: Retrieved cloud top pressure from MOS image recorded at March, 24 th 1998.....	117
Figure 88: Retrieved effective radius from MOS image recorded at March, 4 th 1998	118
Figure 89: Retrieved effective radius from MOS image recorded at March, 24 th 1998	118
Figure 90: Retrieved droplet concentration from MOS image recorded at March, 4 th 1998.....	119
Figure 91: Retrieved droplet concentration from MOS image recorded at March, 24 th 1998.....	119
Figure 92: Back trajectories from March, 4 th 1998	121
Figure 93: Back trajectories from March, 24 th 1998	122

EXECUTIVE SUMMARY

Highlights

CLOUDMAP has further refined user requirements for climate modellers and shown initial very encouraging results of ATSR2 stereo and MOS Oxygen A-band retrievals of cloud-top height validation against traditional cloud-top products used operationally with METEOSAT brightness temperature data.

CLOUDMAP has collected most of the data-sets required for the project with the exception of those from the NASA Terra spacecraft due to a delay in the launch.

CLOUDMAP has produced stereo-derived and Oxygen A-band derived cloud-top heights as well as demonstrated the successful identification of cirrus and contrail clouds using non-thermal sensors.

CLOUDMAP has demonstrated for the first time validation of ATSR2 stereo and brightness temperature cloud-top products using ground-based mm-radars.

CLOUDMAP has demonstrated for the first time validation of AirMISR stereo Cloud-top heights against downward-looking high altitude lidar.

CLOUDMAP has also shown validation of MOS cloud-top pressure products against cloud boundary information derived from radiosondes.

CLOUDMAP has produced the world's first contrail climatology over a 5 year time period over Europe using automated processing methods and AVHRR data.

CLOUDMAP has demonstrated the use of ground-based wide-angle stereo digital imagery for the independent retrieval of cloud-base height.

Objectives

To provide cloud-top parameters (heights or pressures, amounts, types, wind-fields) to Numerical Weather Forecasters and Global Climate Modellers to improve their ability to verify their forecasts including in the long-term the ability to better forecast the impact of natural and anthropogenic changes to the environment.

Context

Current satellite-based products of cloud-top parameters are not well validated and do not meet the requirements of weather forecasters and global climate modellers for either verification or initialisation or assimilation. New sensors launched now and in the near future will provide a far greater potential accuracy than existing products.

Outline of Method

End user workshops will be held by KNMI together with the design, distribution and analysis of questionnaires for professional satellite meteorological data users.

The data producers will process example value-added data products which can be evaluated by KNMI and a team of end users co-ordinated by KNMI.

The data producers will develop a framework for validating these (and existing) satellite data products and test this framework using an agreed set of data with the help of KNMI.

The data producers will research new methods for cirrus and contrail detection in the absence of thermal IR split-window data but given cloud-top parameters, such as height, as additional information layers.

The data producers will provide KNMI validated products for their internal evaluation and for onward external assessment against existing satellite data products.

Progress to date

Significant progress has been made in data product development, in end user requirements' definition and in the researching of new methods for cirrus and contrail detection.

Internal and External Publications

There were no formal internal publications. The following 20 external publications arose directly from the CLOUDMAP project within the second year of the project including 5 peer review papers in international journals, 1 paper in press and 14 abstracts or papers at international conferences. The complete set of external publications will be included in the Final Report.

Diner, D.J., J.C. Beckert, T.H. Reilly, T.P. Ackerman, C.J. Bruegge, J.E. Conel, R. Davies, S.A.W. Gerstl, H.R. Gordon, R.A. Kahn, J.V. Martonchik, J.-P. Muller, R. Myneni, B. Pinty, P.J. Sellers, and M.M. Verstraete, Multi-angle Imaging SpectroRadiometer (MISR): instrument description and experiment overview., *IEEE Trans. Geosci. Rem. Sens.*, 36 (4), 1072-1087, 1998.

Diner, D.J., G.P. Asner, R. Davies, Y. Knyazikhin, J.-P. Muller, A.W. Nolin, B. Pinty, C.B. Schaaf, and J. Stroeve, New directions in Earth Observing: scientific applications of multiangle remote sensing., *Bull. Am. Met. Soc.*, 80 (11), 2209-2228, 1999.

Drescher A., H. Hetzheim u. J. Fischer, New concepts for spaceborne monitoring of drift and 3D-morphology of cloud fields for weather forecast and climate research, Proc. Intern. Symposium on earth observation systems for sustainable development, Bangalore, India, 1998, pp.178-182, 1998

Hetzheim, H., Separation of Different Textures in Images Using Fuzzy Measures and Fuzzy Functions and their Fusion by Fuzzy Integrals, European Symposium on Intelligent Techniques ESIT'99, Crete, June 1999, S. 34-36, 1999

Hetzheim, H., Mathematical Theory and algorithms for the Detection of Contrails, European Geophysical Society, 24th General assembly of the European Geophysical Society, The Hague, April 1999. Geophysical Research Abstracts Vol. 1 No. 2, 1999, p. 542, 1999

- Hetzheim, H, Analysis of hidden stochastic properties in images or curves by fuzzy measure and functions and their fusion by fuzzy or Choquet integrals", Proc. World Multiconf. Systemics, Cybernetics and Informatics, SCI'99 and ISAS'99 , Orlando, vol. 3, pp. 501-508,1999
- Hetzheim, H, A novel method for Estimation of Model Parameters for Noise corrupted Signals, Proc. ICSP'98, Beijing, 1998, Vol. I pp. 156-160, 1998.
- Kästner,M., R. Meyer, and P. Wendling: Influence of weather conditions on the distribution of persistent contrails. Meteorol. Appl., 6:261-271, 1999.
- Kriebel, K.-T., G. Gesell, M. Kästner, and H. Mannstein, The cloud analysis tool APOLLO: Improvements and validations. Report 126, DLR-Oberpfaffenhofen, Institut für Physik der Atmosphäre, D-82234 Wessling, Germany, (ISSN 0943-4771, submitted to Int. J. Remote Sensing), 1999.
- Mannstein, H. and R. Meyer: Contrail coverage derived from NOAA-AVHRR infrared data. In 27th International Symposium on Remote Sensing of Environment, Tromsø, 1998.
- Mannstein, H. and R. Meyer: Automated contrail detection from AVHRR-data. In European Geophysical Society XXIV General assembly, The Hague, The Netherlands, 1999.
- Mannstein, H. and Meyer, R. and Wendling, P., Contrail Coverage over Western Europe derived from {NOAA-AVHRR}-Data, Proceedings of IGARSS, Hamburg, Germany}", IGARSS99, 1999.
- Mannstein, H., R. Meyer, and P. Wendling: Operational detection of contrails from NOAA-AVHRR-data. Int. J. Remote Sensing, 20(8):1641-1660, 1999.
- Meyer, R., H. Mannstein, and P. Wendling: Contrail coverage of Western Europe from 2 years of NOAA-AVHRR-data. In Proceedings of 'The AMS and EUMETSAT Conference on Satellite Meteorology and Oceanography', Paris, France, May 25 - 29 1998, volume 1, pages 266-269, 1998.
- Muller, J.-P., CLOUDMAP - Evaluation of new macroscopic and microphysical cloud parameters from Earth Observation sensors for climate modelling, in *European Geophysical Society XXV General assembly.*, April 25-29 1999, The Hague, Netherlands
- Muller, J.-P., R. Dundas, and D. Bower, An automated processing system for cloud-top height and amount from ATSR(2) stereo., in *International workshop on Applications of the ERS Along Track Scanning Radiometer.*, ESA, 23 - 25 June 1999, ESRIN, Frascati, Italy, 1999.
- Muller, J.-P., R. Dundas, and C. Vogt, Cloud-top height and cloud amount retrieval using digital stereo photogrammetry with ATSR and MISR., in *European*

Geophysical Society XXV General assembly., EGS, April 25-29 1999, The Hague, Netherlands, 1999.

Palikonda, R., P. Minnis, D. R. Doelling, P.W. Heck, H. Mannstein, and U. Schumann: Potential radiative impact of contrail coverage over continental USA estimated from AVHRR data. In Conference on Atmospheric Radiation. AMS, 1999.

Pawlowska, H., Brenguier, J-L., Schuller, L. Microphysical and radiative properties of Stratocumulus. *Phys. & Chem. Earth*.24(8):927-932, 1999

Schumann U., K. Gierens, H. Mannstein, R. Meerkotter, R. Meyer, P. Minnis, R. Sausen and P. Wendling, 1999, "Fernerkundung von Kondensstreifen und ihre Klimawirkung", In 18. Wiss. Techn. Jahrestagung der Deutschen Gesellschaft für Photogrammetrie und Fernerkundung, München, pp 105-110, 1999.

Preliminary Conclusions

Progress towards project objectives

Significant progress was made in defining the requirements of climate modellers through a workshop held at the EGS99 conference in The Hague in April 1999 for CLOUDMAP products and preliminary ATSR2 and MOS products were supplied to KNMI for their own internal evaluation using independent ground-based lidar and radar data.

Significant progress has also been made in developing a processing chain for stereo cloud-top retrieval using ATSR2 and AirMISR as well as Oxygen A-band cloud-top pressure retrieval from MOMS and microphysical products from MOS. Significant progress has also been made in developing camera models for MOMS and stereo cloud-top height retrievals from MOMS.

Significant progress was also made in processing a five year climatological record of AVHRR-derived contrail detection as well as in the development of research algorithms for contrail and cirrus detection based on fuzzy integrals. Significant progress has also been made in modification of the AVHRR contrail detection algorithm for ATSR2.

No progress has been made in METEOSAT or GOES data collection or in the development of automated motion algorithms for geostationary satellite data.

Significant progress has been made in the development of a prototype system for the use of ground-based radars for cloud-top height validation and examples have been demonstrated for a cloud campaign in the Netherlands (CLARA96) and a combined ground-based and airborne campaign in the UK (CLARE98). Significant progress has also been made in the use of radiosonde measurements for cloud-top pressure measurements from MOS. Significant progress has also been made in validating cloud droplet concentration retrieval from MOS using back-calculation of Lagrangian tracers which demonstrated the Twomey effect associated with polluted air-masses.

Significant progress has been made in the use of ground-based visible digital cameras for the retrieval of cloud-base information through the innovative use of GPS-synchronised shuttering within the Swiss MAP campaign. Less progress has been made on reducing these data into usable products.

The continuing delay in the launch of the NASA EOS Terra mission has resulted in a shift of emphasis from MISR and MODIS to the use of AirMISR.

Implications for the final year

A substantial effort is required to create more CLOUDMAP products for use by KNMI in their own internal evaluation and for KNMI to get independent assessments of these cloud-top products from other national meteorological agencies. It is planned that UCL will develop a set of example products from ATSR2 and MOS and validation from the Chilbolton radar. This will take the form of a web-page as part of the general CLOUDMAP web-page and include statistics of the CTHs derived from ATSR2 stereo and brightness temperature, MOS (where available and coincident) and the Chilbolton mm-radar (see <http://www.ge.ucl.ac.uk/research/CLOUDMAP.html>).

A roadshow is planned towards the end of the final period at several national meteorological agencies. This will include an analysis of whether the CLOUDMAP products address future user requirements and an on-line questionnaire will be developed in association with the web-page to provide detailed feedback on the CLOUDMAP products.

If the NASA EOS Terra launch goes ahead as planned in December 1999, substantial effort will be directed at UCL to an early evaluation of the MISR stereo CTHs with and without the wind effect removed. This will also include an initial evaluation of CTHs derived from MODIS using the CO2 slicing technique which will be used with the SEVIRI instrument onboard METEOSAT Second Generation geostationary satellite due for launch in 2000/2001.

Emphasis in the final period will be on a quantitative validation of CLOUDMAP products particularly from ATSR2 and MOS using both radiosondes and ground-based radar and lidar at the Chilbolton radar facility. Evaluations will also be carried out of automated wind field retrieval using METEOSAT rapid-scan stereo during the MAP campaign.

Finally, development of methods will continue on improving the accuracy, reliability and speed of the stereo ATSR2 processing and completing the AVHRR-derived contrail climatology over Europe and Asia.

Introduction

Objectives

In the second year, end user requirements were further refined with emphasis on the global climate modelling community through a workshop held at the EGS99 conference.

Data producers focused their efforts on developing a pre-operational processing chain for automated cloud-top product retrieval from ATSR2 and AirMISR stereo and MOS Oxygen A-band as well as cloud microphysical products from MOS.

Data producers needed to provide several example products from this processing chain for evaluation by KNMI as well as an initial validation using ground-based radars, both ground-based and airborne lidars and traditional radiosondes.

Data producers needed to demonstrate the feasibility of cirrus and contrail detection in non-thermal imagery as well as the retrieval of cloud-base height from wide-angle stereo imagery.

Data producers also needed to demonstrate that a long-term climatology of contrails could be created using AVHRR data over a minimum of 5 years covering the European region.

Context

Clouds play a pivotal role in the interaction between the Earth's climate and anthropogenic inputs, particularly from the increase in greenhouse gases. Clouds play this role by governing the Earth's energy balance as a result of their optical thickness, with high albedo in the solar spectral range and a screening or cooling effect in the thermal infrared regime, and by their large areal extent and variability on all spatial and temporal scales. Radiative forcing by clouds turned out to be an important factor, modifying the large scale dynamics of the Troposphere, with the height of clouds as a crucial observational parameter.

Cirrus clouds influence the radiation budget in a way that enhances the greenhouse effect. A continuous observation of cirrus cloud properties is needed to be able to distinguish between natural and air-traffic contrail related cirrus clouds. Additionally it is believed that an increase in atmospheric temperature correspond to an increase in atmospheric humidity and thus also with an increase in clouds and possibly an increase in cirrus cloud amount. We need to study if an increase in cirrus clouds can be measured from space and to quantify what contribution that sub-sonic air traffic contrails have in any increase observed.

Brief introduction to the CLOUDMAP consortium

The principal end user is KNMI. The principal stereo data producer is UCL with DLR-IPE looking at shadow techniques for validation and the evaluation of existing algorithms for high resolution stereo cloud-top height retrieval and ETH working on developing new techniques for high resolution stereo cloud-top parameter retrieval and cloud-base height from ground-based wide-angle stereo images. The principal cloud-top parameter and cloud microphysical data producer from Oxygen A-band is FUB. Research into fuzzy logic methods for contrail and cirrus detection is being carried out by DLR-IST.

UCL is taking the lead in developing validation methods and for intercomparison of instruments and methods.

Work achieved over the period

Overview

The work achieved in the last reporting period is broken down by work-package and consortium partners as detailed in the technical Annex as follows:

- End User Evaluation (KNMI)
- Data Collection (UCL, DLR-IPE, ETH, DLR-IPA, FUB)
- Data processing Algorithm Development and Implementation (UCL, DLR-IPE, ETH, DLR-IPA, FUB)
- Value-added Data Production (UCL, DLR-IPE, ETH, DLR-IPA, FUB)
- Validation and Scientific Evaluation of Products (UCL, DLR-IPE, ETH, DLR-IPA, FUB)

Milestones reached

For a description of CLOUDMAP milestones, please see section 6 of the Technical Annex.

A statement of user requirements was further refined which included revised success criteria which is given in section 3.3.1.

The implementation report was completed which is given in section 3.3.3.

The first validation report was completed and is given in section 3.3.5.

ATSR2 and MOS products were delivered to the end user KNMI by UCL and FUB respectively and their evaluation is described in section 3.3.1.

Progress by Work Package

End user evaluation (KNMI)

KNMI Objectives in the Second Year

The role of KNMI within the CLOUDMAP project is to assess user aspects of the cloud products to be researched within CLOUDMAP. In other words this role can be described as “bridging” the gap between the “technology driven” CLOUDMAP partners and the “application driven” end users. The anticipated end users of CLOUDMAP products are operational weather forecasters, developers of Numerical Weather Prediction (NWP) models and climate researchers.

In the first year of CLOUDMAP KNMI focused on the collection of user requirements of cloud parameter products in general and of CLOUDMAP products in particular. Furthermore major European developments, relevant to CLOUDMAP, were monitored and evaluated for their cross-links with CLOUDMAP.

The objective of KNMI was to continue this work in the second year of CLOUDMAP in order to refine the work done in the first year. A next objective in the second year was to start the end-user evaluation of CLOUDMAP products.

Work performed by KNMI

To meet the aforementioned objectives KNMI performed the following work:

- *Literature studies.*

In the second year, monitoring of the relevant international literature through journals and Internet /WWW was continued. Again special attention was given to the finding of “user requirement” documents.
- *Attending relevant conferences and workshops.*

In December '98 the EUMETSAT SAF Training Workshop of the Nowcasting SAF in Madrid was attended. This workshop provided an update of the status of the work performed in this SAF (Satellite Application Facility) and was intended to match future development work in the Nowcasting SAF to work done in other projects (like CLOUDMAP) and to requirements of the users attending the workshop. A report of the workshop can be found on the EUMETSAT web site (<http://www.eumetsat.de>).

In September 1999 the EUMETSAT Meteorological Satellite Data Users' Conference in Copenhagen was attended. Again the latest developments in the MSG ground segment (SAFs and MPEF) were presented there.
- *Communication with different expert end users working within KNMI.*

Intensive communication with relevant experts (in all three anticipated end uses of CLOUDMAP) within KNMI was continued during the second year of the project. The third CLOUDMAP Technical Progress Meeting was held at KNMI in April '99 and during the meeting the CLOUDMAP project team took the opportunity to communicate with all three expert end users within KNMI.
- *Organising the second “user requirement” workshop.*

KNMI organised a workshop with the aim to bring together end users and experts working in the field of climate research discussing the needs for cloud information and the role of satellites to provide this information.

To save travel and subsistence costs of participants the workshop was held during the EGS General Assembly in The Hague, The Netherlands on 21 April 1999. A report on the workshop can be found in appendix A.
- *End user evaluation of CLOUDMAP products of CLARA96 campaign.*

ATSR cloud top height (CTH) maps, produced by UCL, were evaluated in relation to “end use” aspects. Eleven cases were analysed. Besides a rough validation of the CTH special attention was given to the added value of the ATSR maps in relation to the operational products, to the limitations and finally to the presentation of the ATSR maps. The analysis work was done with the help of a climate researcher and an operational forecaster. This work is described below in paragraph 3.1.4.
- *Presenting progress of work to CLOUDMAP partners at Technical Progress meetings.*

Progress of work at KNMI was presented at the second Technical Progress meeting at DLR in Oberpfaffenhofen and at the third meeting at KNMI in De Bilt. The results of the work of KNMI until halfway the project were presented at the Mid Term Review meeting at ETH in Zurich in September 1999.

Assessment of the fulfilment against project objectives

The first objective of KNMI, the settlement of a solid user requirement document, has been successfully fulfilled. These user requirements will form the basis for the settlement of success criteria to be used in the evaluation of CLOUDMAP products.

The user requirement document was included as an appendix in the first CLOUDMAP Interim Report.

KNMI continued its efforts to follow and report the developments in the EUMETSAT ground segment which are relevant to the CLOUDMAP project. A first conclusion of this work is that CLOUDMAP products might play an important role in the validation of the Nowcasting SAF and MPEF cloud products (both of MSG and NOAA/METOP AVHRR). Validation procedures for these products are not yet defined and independent data sources, as the CLOUDMAP products, might be used in the future (if the accuracy meets the requirements).

The second CLOUDMAP user workshop was held during the EGS Assembly in The Hague. To complement the first workshop, which focused on operational forecasters, the objective of this second workshop was to obtain user feedback from the climate research community. For this purpose the workshop was partly embedded in the official programme of the symposium AO30 with the title "Use of satellite data in climate studies". The first part included six presentations of CLOUDMAP partners providing the audience a good introduction to the discussion part of the workshop. The presentation part was attended by a rather large audience of about 50 to 70 persons. Unfortunately the starting time of the discussion part was at a rather unfavourable moment of the day (18.30 hours). This heavily influenced the number of participants in the discussion. Still a lively discussion occurred on the basis of prepared (and a little provocative) theses and provided an excellent insight in the opinions of climate researchers. Two main conclusions are derived from the second CLOUDMAP workshop:

- For the purpose of process studies, climate research badly needs long time series of unambiguous data of cloud parameters. The operational meteorological satellite programmes provide long term data continuity. Therefore, the focus in climate studies is very much on the use of the World Weather Watch satellites (METEOSAT, GOES, TIROS, etc.). However, the ambiguous calibration of the sensors on board of these satellites still forms a large drawback with regard to their use in climate studies. CLOUDMAP products might help to derive better calibration of meteorological satellite data.
- The CLOUDMAP products provide helpful information for a better understanding of the role of clouds in global climate change. Independent information on cloud top height and optical thickness (the main CLOUDMAP products) is very useful and valuable to improve the cloud parameterisation in climate models.

A more detailed report of the second CLOUDMAP workshop can be found in appendix B. Workshop Report/s

An evaluation of the ATSR CTH maps of the CLARA96 campaign was performed by KNMI. The result was a preliminary list of conclusions on the usefulness and recommendations for improvement of the product. A description of the work and the results can be found in the next section.

Evaluation of ATSR2 CTH maps for the CLARA96 campaign

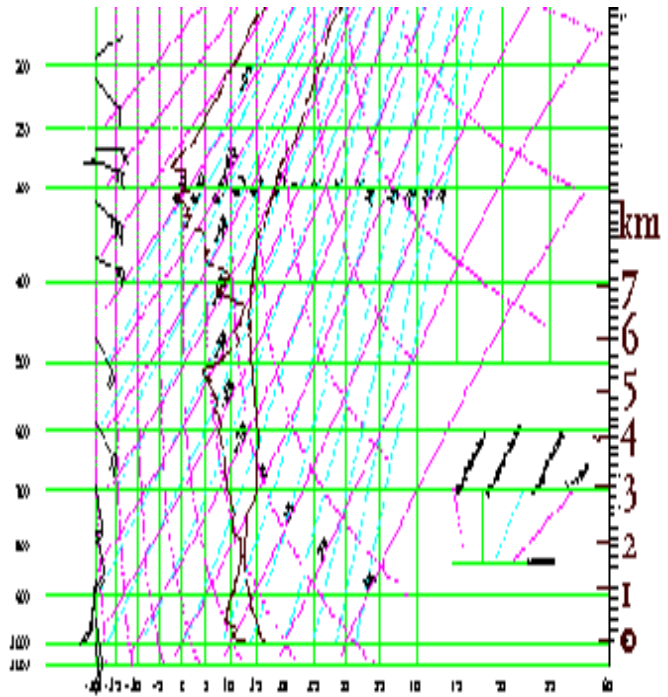
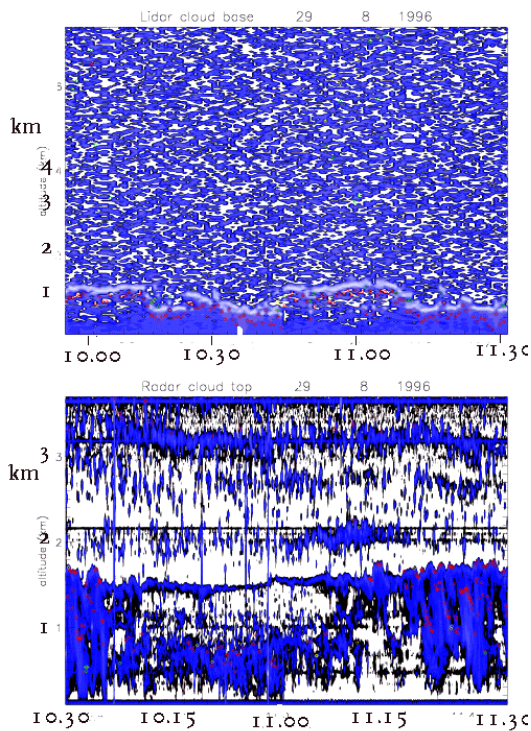
In the second half of 1999 stereoscopic ATSR-CTH results were evaluated for use in operational forecasting and climate research.

The dates for comparison were driven by the availability of independent measurement data. In this the KNMI could rely on the CLARA96 campaign (CLOUDS And RADIATION: Intensive study of clouds and radiation in The Netherlands). A measurement campaign totally dedicated to clouds. More detailed information about the campaign can be found at: <http://www.knmi.nl/CLARA/>

ATSR-CTH results, as processed and delivered by UCL, were compared in a qualitative manner to a number of different data sources and shown to experts, a forecaster and a science team member of the CLARA96 project. The ATSR passes used in this study were all around 11.00 GMT.

From the CLARA campaign observations were obtained by ground based Lidar (1064 and 532 nm) and 3.3 GHz Radar. The Lidar of the RIVM provided information about the cloud base height. The viewing range, however, is limited (< 4km height). The Radar of the University of Delft is able to pick up cloud top height, but it is also sensitive to rainfall and to clear-air turbulence. Moreover, as the Radar and Lidar data are not filtered the interpretation of the data is not straightforward. Therefore the uncertainty of the numbers shown for Lidar and especially Radar is quite significant. In Figure 1 the Lidar and Radar plots of August 29 '96 are shown in order to illustrate these interpretation problems.

Additional information was obtained from radiosonde data at De Bilt. Cloud base and top height extraction from radiosonde profiles usually requires the skill of a forecaster/meteorologist. Moreover, radiosonde data are not easy to collocate in space and time as the balloon drifts with the wind and it takes about 1 to 1_ hours before the sonde has reached the tropopause. In Figure 2 an example of a radiosonde profile (of August 29 '96) is presented.



<p>Figure 1. August 29 1996. Top: Lidar Bottom Radar <i>White line indicates the height of the cloud base Red spots indicate the CTH</i></p>	<p>Figure 2. August 29 1996. 12Z Radiosonde plot <i>Left curve is dry bulb temperature. Right curve is wet bulb temperature Clouds exist where $T_{dry} \approx T_{wet}$ (→ at 2 and 6.5 km</i></p>
---	--

Other satellite information was obtained from the METEOSAT satellite. The algorithm MetClock, developed at KNMI, determines corrected cloud top brightness temperatures that can be converted to cloud top heights using radiosonde or NWP model information.

The comparison results are shown in two tables one for the measurement campaign in Delft (Table 1) and one for the radiosonde location in De Bilt (Table 2).

Table 1. Comparison of CTH at the Delft site. Heights are given in km.

The question marks relate to undetermined cloud base/ top heights.

Date	Lidar (cloud base	Radar	METEOSAT	ATSR 1.6 μ m	ATSR 11 μ m
29 Aug '96	0.5 - 1	1-2	2.3	1-2	1-2
1 Sep '96	2.5	1-2	1.1	3-4	3-4
19 Nov '96	?	?	6.4	8-9	8-9
23 Nov '96	3	?	3.2	4-6	4-6
29 Nov '96	1	2 / 4.5	7	8-9	8-9
2 Dec '96	1	?	2.5	2-4	2-4

The general impression of Table 1 is that there is agreement between the different CTH. Striking is the good agreement between the ATSR maps. However, the ATSR results have the tendency to overestimate the CTH in comparison to the other information sources.

The table clearly shows the limitations of the Lidar and Radar data for purposes of CTH validation. The Lidar measured cloud base heights match the ATSR CTH values but of course do not prove the correctness of the CTH values. E.g. in the case of November 29th obviously (at least) two layers of clouds exist. The Radar does not provide clear CTH values in four of the seven cases. This is due to the fact that the 3.3 GHz frequency is not ideal for cloud height detection (94 GHz is much more suitable). Two of the three cases contain a “clear” Radar signal are still questionable. On September 1st the Radar signal suggested a CTH between 1 and 2 km where the Lidar clearly shows a cloud base height at 2.5 km. On November 29th the Radar signal “sees” two cloud layers which can be confirmed by the false colour METEOSAT image. According to the Radar the CTH of the top layer is 4.5 km. This seems to be much too low for this type of cloud (Cirrus). The radiosonde of De Bilt indeed suggests a Cirrus layer at 7 km.

Table 2. Comparison of CTH at De Bilt. Heights are given in km.

Date	Radiosonde lowest layer	Radiosonde Cirrus layer	METEOSAT	ATSR 1.6 μm	ATSR 11 μm
26 Aug '96	2	-	-	3-4	4-5
29 Aug '96	2	6.5	3.1	2-3/5-9	3-4/7-9
1 Sep '96	3	-	3.2	3-4	3-4
20 Nov '96	2	8.5	3.6	3-5	9-11
23 Nov '96	3.5	-	3.0	4-6	4-8
29 Nov '96	4.5	7	7	7-9	6-8
2 Dec '96	2.5	-	2.5	2-4	3-5

Similar to table 1 the ATSR stereo technique seems to overestimate the CTH in most cases. Opposite to table 2 there are some differences between the 1.6 μm and the 11 μm CTH maps. The 11 μm CTH values are little higher than the 1.6 μm results. November 20th shows an extreme difference between 1.6 μm and the 11 μm results. The 11 μm channel probably detects a very thin high Cirrus layer, which is missed by the 1.6 μm channel.

Four cases were selected for a more extensive analysis: August 29 '96 (figure 3), September 1 '96 (figure 4), November 20 '96 (figure 5) and November 29 '96 (figure 6).

Case 1: August 29, 1996

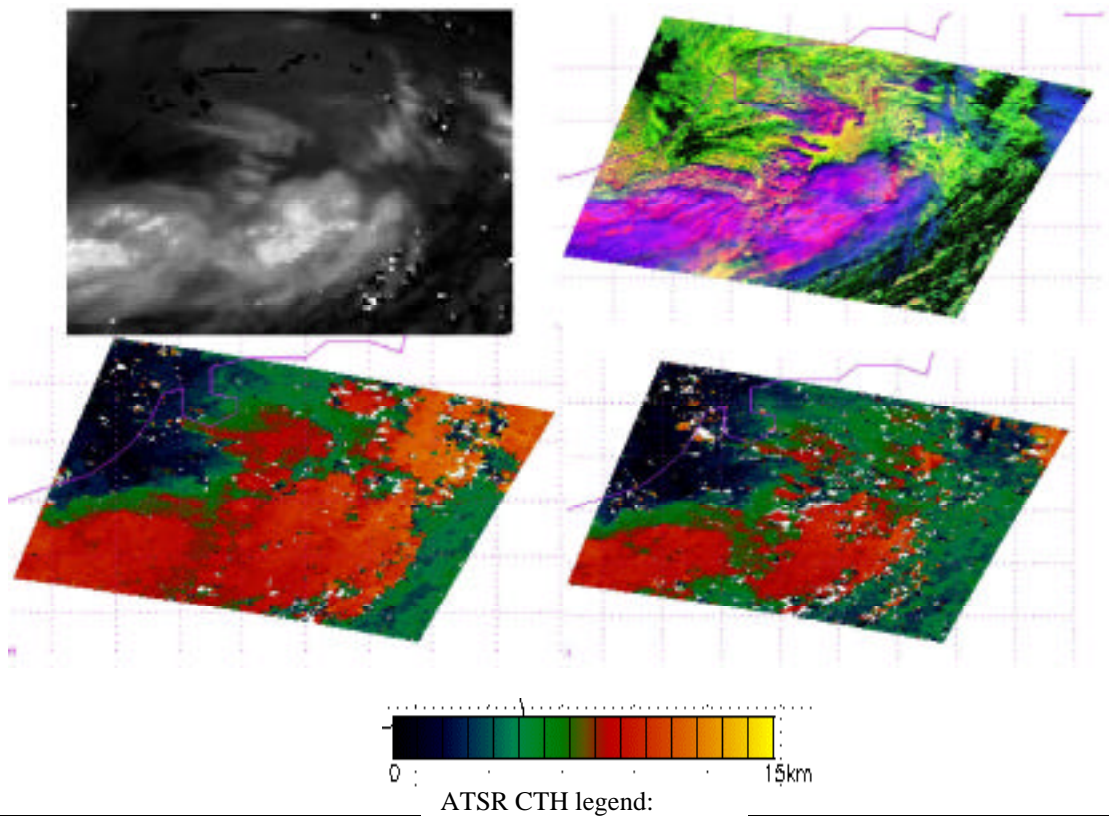


Figure 3. August 29, 1996. METEOSAT CTH (UL), false colour composite using 0.65, 1.6, 11 μm (RGB value).(UR), ATSR 11 μ (LL) and 1.6 μm (LR), A colour bar denotes the CTH scale. White spots indicate areas where the stereo matcher was not able to calculate a height.

All views contain roughly the same area. In the ATSR RGB image the high clouds appear as blue (Cirrus) and purple, low clouds as yellow/green (ATSR results supplied by UCL).

Discussion

Both 1.6 μm and the 11 μm CTH results above Delft match with the Lidar and Radar signals. The 1.6 μm CTH values around De Bilt also match very well with the radiosonde profile: a two-layer cloud system at 2 and 6.5 km. The 11 μm channel overestimates the CTH for both layers. More differences between the 1.6 μm and the 11 μm CTH results are visible. E.g. the 11 μm channel map shows very high clouds in the north east part of the map that are not mapped by the 1.6 μm channel. The RGB image suggests high Cirrus clouds in this area that are difficult to detect by the 1.6 μm channel.

Case 2: September 1, 1996

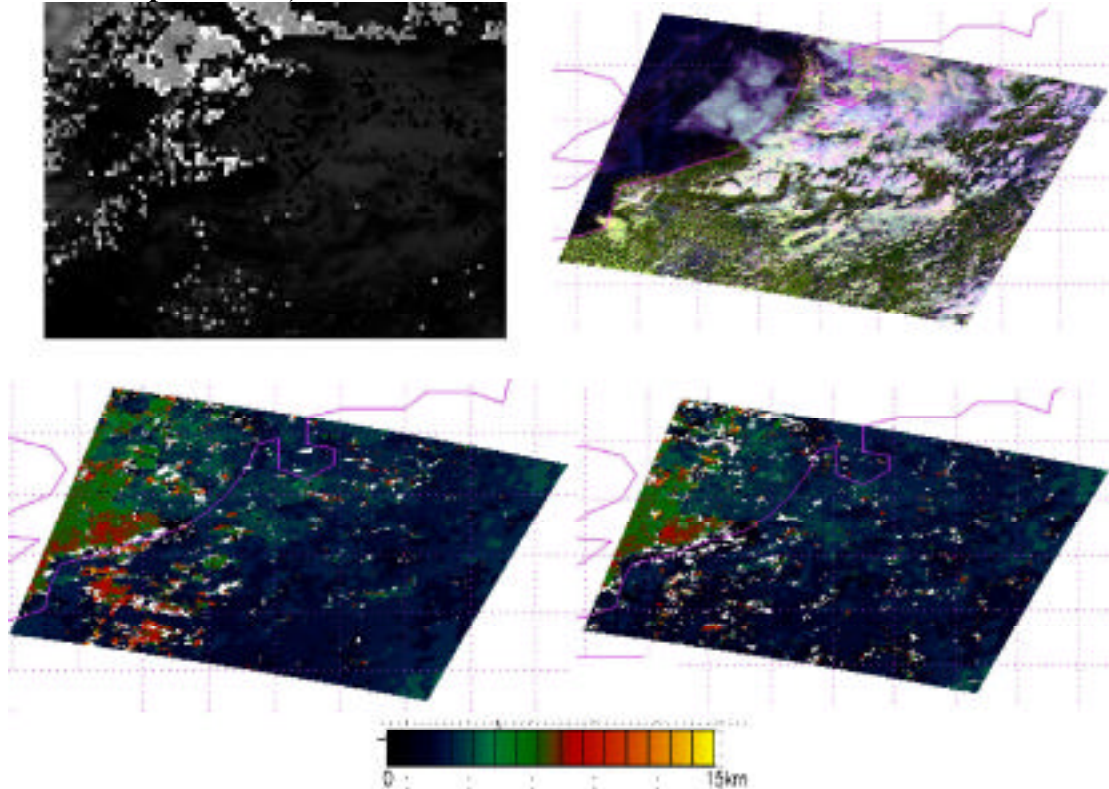


Figure 4. September 1, 1996 METEOSAT CTH (UL), false colour composite using 0.65, 1.6, 11 μm (RGB value).(UR), ATSR 11 μm (LL) and 1.6 μm (LR), A colour bar denotes the CTH scale. White spots indicate areas where the stereo matcher was not able to calculate a height.

All views contain roughly the same area. In the ATSR RGB image the high clouds appear as blue (Cirrus) and purple, low clouds as yellow/green (ATSR results supplied by UCL).

Discussion. The comparison of ATSR CTH with the Lidar, Radar and radiosonde information shows a slight overestimation by the ATSR results (see table 1 and 2). Compared to 1.6 μm , the 11 μm channel overestimates the CTH even more as can be seen in the map. Another striking difference between 1.6 μm and 11 μm results can be seen in Belgium and northern France. The 11 μm maps high (probably Cirrus) clouds that are also vaguely visible in the RGB image (the blue/grey spots). In both ATSR CTH maps high clouds before the Belgium coast are mapped. The RGB image seems to show a cloudfree area at that location. By stretching the original ATSR 11 μm channel image (see below) it becomes clear that the sky is definitely not clear above this part of the North Sea and that the stereo matcher correctly detects these high Cirrus clouds and contrails. The reason why the 1.6 μm CTH map also shows these high clouds is that the thin Cirrus clouds contrast enough with the dark sea surface background

	<p>This example demonstrates the potential of this stereo technique.</p>
--	--

Case 3: November 20, 1996

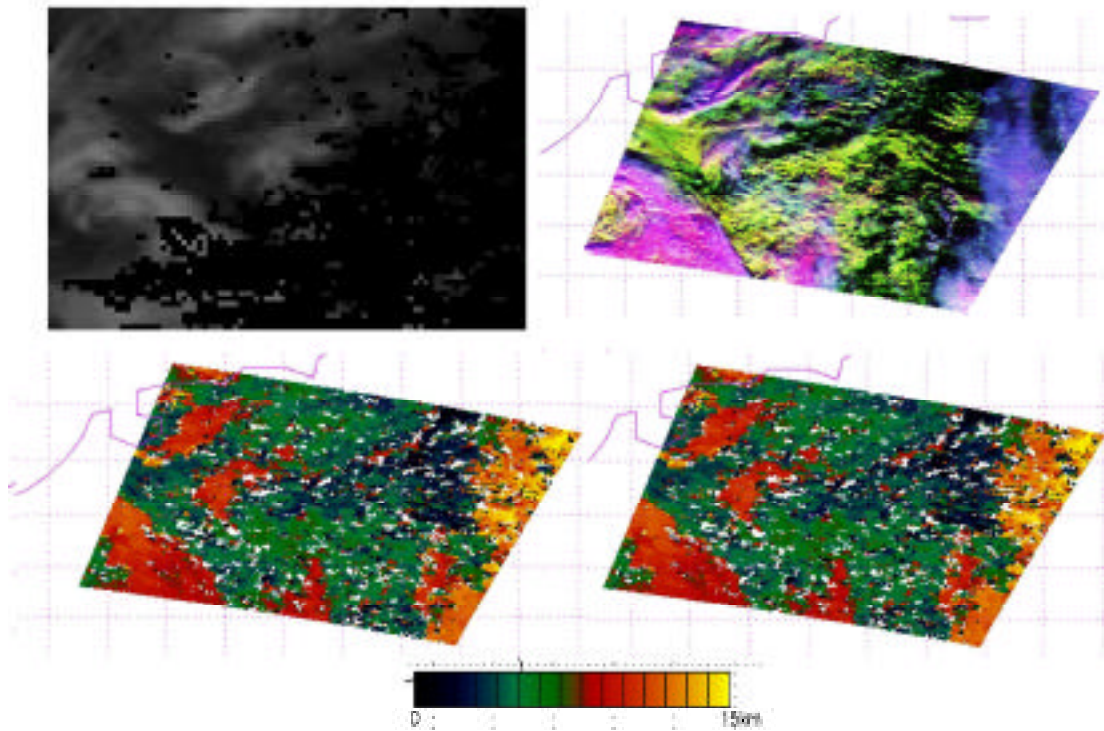


Figure 5. November 20, 1996 METEOSAT CTH (UL), false colour composite using 0.65, 1.6, 11 μm (RGB value). (UR), ATSR 11 μ (LL) and 1.6 μm (LR), A colour bar denotes the CTH scale. White spots indicate areas where the stereo matcher was not able to calculate a height.

All views contain roughly the same area. In the ATSR RGB image the high clouds appear as blue (Cirrus) and purple, low clouds as yellow/green (ATSR results supplied by UCL).

Discussion

As mentioned already in the discussion of table 2 the 1.6 μm channel obviously misses the thin Cirrus layer above the central part of The Netherlands and slightly overestimates the CTH of the lower cloud layer. The 11 μm channel indeed detects the Cirrus layer although a little higher as can be interpreted from the radiosonde profile.

The Cirrus layer in the eastern part of the image, as visible in the RGB image (blue/purple colour), is stereo matched in both channels at a height of up to 15 km. This is bit unrealistic when looking at the radiosonde profile of De Bilt indicating the tropopause at around 10 km (Cirrus does not exist above the tropopause).

Case 4: November 29, 1996

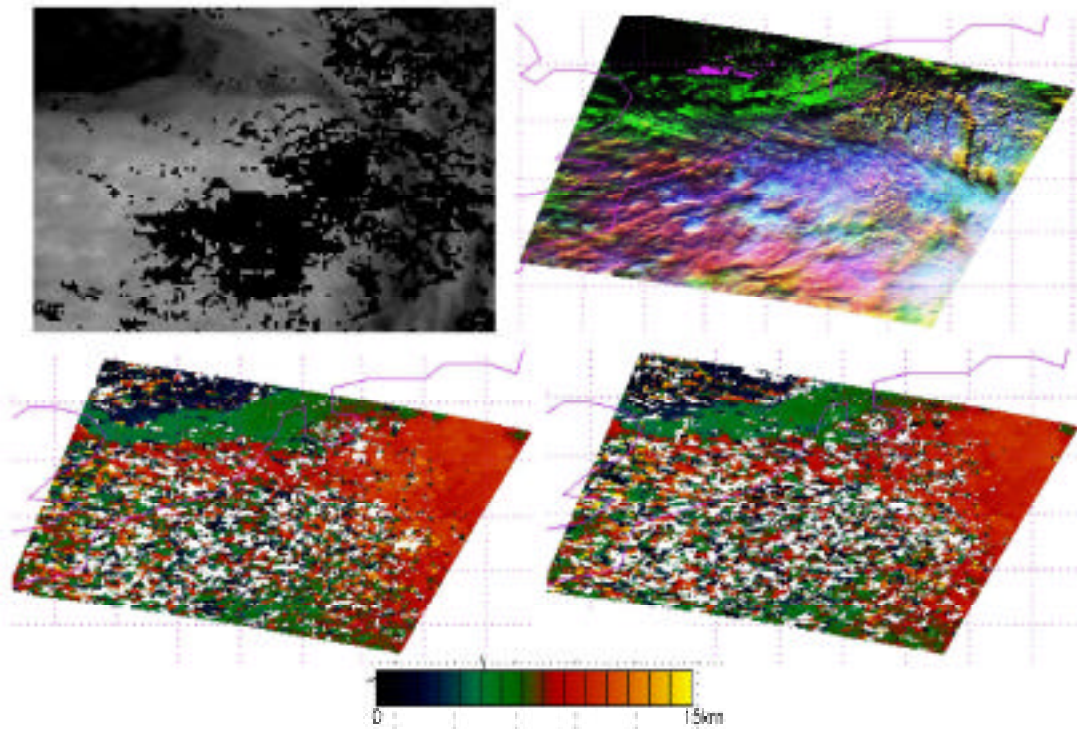


Figure 6: November 29, 1996 METEOSAT CTH (UL), false colour composite using 0.65, 1.6, 11 μm (RGB value).(UR), ATSR 11 μ (LL) and 1.6 μm (LR), A colour bar denotes the CTH scale. White spots indicate areas where the stereo matcher was not able to calculate a height.

All views contain roughly the same area. In the ATSR RGB image the high clouds appear as blue (Cirrus) and purple, low clouds as yellow/green (ATSR results supplied by UCL).

Discussion

The ATSR stereo matcher maps the high cloud layer above the central part of The Netherlands correctly according to the radiosonde profile interpretation. The Lidar and Radar signals do not reach this layer. So, no confirmation can be obtained from these data sources.

The surface of the top cloud layer above the continent shows rather rough. At lower solar zenith angles in this period of the year the reflectance of this rough kind of surface is strongly influenced by shadow effects. The stereo matcher has a lot of problems with this shadow effect resulting in a speckled pattern with a lot of missed matches (white spots) that make it hard to interpret.

In general the 1.6 and 11 μm CTH maps are in good agreement with each other and also with the RGB image. The lower cloud layer crossing the southern North Sea is well represented in the CTH maps.

Next to the ATSR stereo matching CTH results there were two cases in which observations obtained with the MOS sensor collocated with the CLARA 96 campaign. Cloud top pressure MOS images of these two cases were processed and delivered by FUB. Unfortunately, both cases are not very useful for evaluation purposes. The first case of August 19, 1996 was a completely cloud free day for The Netherlands and surroundings. For the second case, September 12, 1996 no ground observations are available, only METEOSAT data. The clouds occurring at that moment did not show a wide variety. The METEOSAT RGB composite shows low stratus layer with some high clouds above. In Figure 7 the MOS cloud top pressure map, the collocated METEOSAT RGB image and the obtained MetClock CTH results are shown. There are similar cloud features distinguishable. The higher clouds (blue in the MOS image and orange/red in the METEOSAT CTH image) and the lower clouds (green in both images) coincide fairly well. It is noticeable that the MetClock algorithm detects much more clouds above The Netherlands than can be seen in the MOS image. This might be an effect of the large difference in spatial resolution of both sensors: MOS about 500 m and METEOSAT about 5 x 10 km (at 50 North). The presentation of the MOS result image is very helpful for end use purposes: the colour coding is very natural and easy to interpret and the use of cloud mask helps the user to distinguish clouds from cloud free areas. N.B. It was agreed that for the final year, this representation would be used.

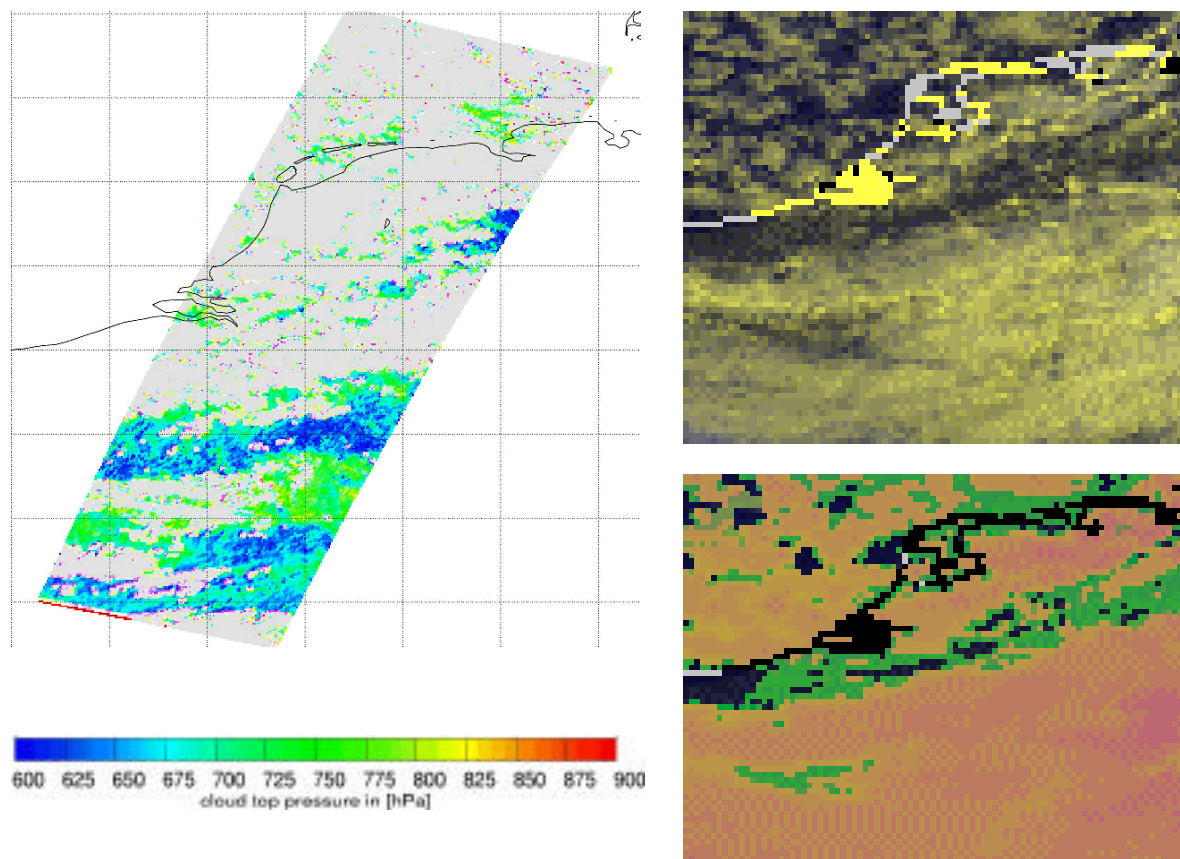


Figure 7: September 12, 1996, 10.00 UTC.

Left: The MOS cloud top pressure map; the light grey pixels are cloud free. *Upper right:* the collocated false colour RGB METEOSAT image; the dark spots are cloud free; the grey/yellow colours indicate lower clouds and

the yellow/white colours indicate higher clouds. *Bottom right*: METEOSAT qualitative CTH map (MetClock result); Black is cloud free; green indicates low clouds and yellow/orange/red indicate higher clouds

End user evaluation conclusions

- The radiosonde appears to be a more reliable and complete CTH data source than Lidar and the 3.3 GHz Radar. However, the problem of collocation should be kept in mind.
- The first comparison of obtained ATSR CTH values to other data sources is encouraging. The results are in reasonable agreement. Still further and more extensive comparisons are required. Preliminary conclusions:
 - The ATSR stereo matching seems to overestimate the CTH in many cases. This is more obvious in the case of the 11 μm channel.
 - Cirrus clouds are mostly mapped correctly by the 11 μm channel but sometimes missed by the 1.6 μm channel.
 - The ability of the ATSR stereo matching technique to map the CTH of Cirrus correctly forms a strong recommendation to use this technique operationally since other data sources (both ground and space based) do not provide this information.
- The presentation of the ATSR CTH maps should be improved in order to encourage end use. Some recommendations:
 - The difference between the 1.6 μm and the 11 μm results needs to be solved or both results should be merged into one CTH map. One unambiguous CTH would be beneficial for end user purposes.
 - A cloud mask at full ATSR resolution, derived from the original ATSR channels, should be applied to the CTH maps. This will help the end user to identify the clouds (or cloud free areas) and to see fine structures of the clouds (small holes, edges). Another advantage of applying a cloud mask is that erroneous CTH values are removed by the cloud mask in cases where the pixels are cloud free. The MOS image in figure 7 shows what is recommended here.
 - The colour coding of the CTH values should use a more natural colour order (blue for high clouds and red for low clouds; again see the MOS image).

Project Plan of KNMI activities for the final period

The project plan of KNMI for the performance of activities within the CLOUDMAP project has changed slightly from the description in the Technical Annexe of the contract. Therefore, the small changes and a summary of these activities are provided in this report. The details can be found in the Technical Annexe.

- To study the impact of CLOUDMAP products on NWP-models it was originally planned to perform an experiment in which CLOUDMAP CTH data would be assimilated in the experimental model RACMO (Regional Atmospheric Climate Model) of KNMI. Discussions with NWP modellers revealed that it is very doubtful if such an experiment would be useful and worth the rather large effort. The doubt of the experts is based on the limited temporal resolution and area coverage of the CLOUDMAP products probably resulting in very low impacts. Another important problem in this matter is that most NWP models (including RACMO) are currently not able to absorb the information included in the CLOUDMAP products. Major adjustments to the models will be necessary in order to enable an effective absorption of the CLOUDMAP information. Since

this exercise might be out of range of the CLOUDMAP project KNMI will first do some more research on the feasibility of the original idea of an impact study.

- For the introduction of (real-time) products to operational forecasters the use of Internet/Intranet pages appears to be the best option. Forecasters will be invited to evaluate the products at quiet hours during their shifts. To achieve an effective evaluation KNMI is very much dependent on the delivery of products by the other CLOUDMAP partners. In the first instance the selection of products of interesting meteorological situations seems to be the most realistic option to enable retrospective case studies by the forecasters. Real-time (within 3 to 4 hours) availability of products is not yet realistic although ESA/ESRIN has recently established a (near) real-time service for the distribution of ATSR data. An experiment to use this service and to experience the timeliness of product availability for the forecaster is optional.
- To evaluate the usefulness of CLOUDMAP products for climate research it is planned to use CLOUDMAP products as an extra data source in some past and future international experiments (like in the CLARA96 campaign). Besides the ATSR products also the MOS and MOMS products (if available) will be evaluated.
- In the final year of the CLOUDMAP project some major European institutes (including both weather services and climate research groups) will be visited with the aim to demonstrate to end users the CLOUDMAP products and their potential application in order to obtain feedback on the usefulness of the products.

At the end of this final year of the project KNMI will contribute its part to the final report.

Data collection

UCL

ATSR2 data collection

ATSR2 data over the UK and over Delft (see results and discussion in section 3.3.3.1) were ordered via the ESA data grant ESA A03-422 (See First Interim Report). They were obtained on CD-ROM from the UK-PAF at NRSCL. FUB were asked to find MOS data which would coincide with ATSR2 within a very short time interval.

Table 3 lists the ATSR2 scenes obtained over the UK covering the Chilbolton radar site and Table 4 lists the ATSR2 scenes obtained covering the CLARA96 campaign over the Netherlands.

Table 3 List of ATSR2 scenes obtained over the UK covering the Chilbolton radar site.

	DATE	TIME	ORBIT	TRACK	FRAME
1	14-Aug-98	11:15:26	17340	452	2565
2	20-Aug-98	11:26:55	17426	37	2565
3	2-Sep-98	11:18:20	17612	223	2565
4	5-Sep-98	11:24:05	17655	266	2565
5	8-Sep-98	11:29:50	17698	309	2565
6	12-Sep-98	11:03:57	17755	366	2565
7	7-Oct-98	11:18:20	18113	223	2565
8	10-Oct-98	11:24:04	18156	266	2565

CLOUDMAP - Cirrus and Contrail cloud-top maps from satellites for Weather Forecasting and
Climate Change Analysis :Second Interim Report (1998-99)

	DATE	TIME	ORBIT	TRACK	FRAME
9	13-Oct-98	11:29:47	18199	309	2565
10	23-Oct-98	11:15:23	18342	452	2565
11	26-Oct-98	11:21:08	18385	495	2565
12	29-Oct-98	11:26:53	18428	37	2565
13	1-Nov-98	11:32:39	18471	80	2565
14	5-Nov-98	11:06:46	18528	137	2565
15	8-Nov-98	11:12:30	18571	180	2565
16	11-Nov-98	11:18:14	18614	223	2565
17	14-Nov-98	11:23:58	18657	266	2565
18	17-Nov-98	11:29:42	18700	309	2565
19	24-Nov-98	11:09:34	18800	409	2565
20	27-Nov-98	11:15:21	18843	452	2565
21	30-Nov-98	11:21:06	18886	495	2565
22	3-Dec-98	11:27:21	18929	37	2565
23	6-Dec-98	11:32:36	18972	80	2565
24	10-Dec-98	11:06:42	19029	137	2565
25	22-Dec-98	11:29:45	19201	309	2565
26	25-Dec-98	11:35:31	19244	352	2565
27	26-Dec-98	11:03:54	19258	366	2565
28	13-Dec-98	11:12:28	19072	180	2565
29	16-Dec-98	11:18:14	19115	223	2565
30	19-Dec-98	11:24:00	19158	266	2565
31	29-Dec-98	11:09:38	19301	409	2565
32	2-Oct-98	21:58:03	18048	158	1035
33	5-Oct-98	22:03:48	18091	201	1035
34	12-Oct-98	21:43:38	18191	301	1035
35	15-Oct-98	21:49:21	18234	344	1035
36	28-Oct-98	21:40:43	18420	29	1035
37	31-Oct-98	21:46:29	18463	72	1035
38	6-Nov-98	21:57:58	18549	158	1035
39	9-Nov-98	22:03:42	18592	201	1035
40	16-Nov-98	21:43:32	18692	301	1035
41	19-Nov-98	21:49:16	18735	344	1035
42	2-Dec-98	21:40:42	18921	29	1035
43	5-Dec-98	21:46:25	18964	72	1035
44	8-Dec-98	21:52:10	19007	115	1035
45	11-Dec-98	21:57:55	19050	158	1035
46	21-Dec-98	21:43:36	19193	301	1035
47	24-Dec-98	21:49:21	19236	344	1035
48	14-Dec-98	22:03:41	19093	201	1035
49	27-Dec-98	21:55:05	19279	387	1035
50	1-Jan-99	11:15:21	19344	452	2565
51	2-Jan-99	22:06:32	19365	473	1035
52	6-Jan-99	21:40:38	19422	29	1035
53	7-Jan-99	11:26:50	19430	37	2565
54	9-Jan-99	21:46:25	19465	72	1035
55	10-Jan-99	11:32:37	19473	80	2565
56	12-Jan-99	21:52:11	19508	115	1035
57	14-Jan-99	11:06:45	19530	137	2565
58	15-Jan-99	21:57:58	19551	158	1035
59	17-Jan-99	11:12:31	19573	180	2565
60	18-Jan-99	22:03:44	19594	201	1035
61	20-Jan-99	11:18:17	19616	223	2565
62	22-Jan-99	21:37:52	19651	258	1035
63	23-Jan-99	11:24:02	19659	266	2565
64	26-Jan-99	11:29:47	19702	309	2565
65	30-Jan-99	11:03:54	19759	366	2565
66	31-Jan-99	21:55:05	19780	387	1035
67	2-Feb-99	11:09:38	19802	409	2565

	DATE	TIME	ORBIT	TRACK	FRAME
68	3-Feb-99	22:00:50	19823	430	1035
69	5-Feb-99	11:15:21	19845	452	2565
70	6-Feb-99	22:06:35	19866	473	1035
71	8-Feb-99	11:21:07	19888	495	2565
72	10-Feb-99	21:40:43	19923	29	1035
73	11-Feb-99	11:26:53	19931	37	2565
74	27-Feb-99	11:23:59	20160	266	2565
75	2-Mar-99	11:29:42	20203	309	2565
76	9-Mar-99	11:09:38	20303	409	2565
77	12-Mar-99	11:15:23	20346	452	2565
78	18-Mar-99	11:26:54	20432	37	2565
79	25-Mar-99	11:06:46	20532	137	2565
80	31-Mar-99	11:18:16	20618	223	2565

Table 4 List of ATSR2 scenes obtained over the CLARA96 experiment in the Netherlands.

	DATE	TIME	ORBIT	FRAME	TRACK
1	19-Aug-96	11:01:06	6962	02565	00094
2	22-Aug-96	11:06:51	7005	02565	00137
3	26-Aug-96	10:41:00	7062	02565	00194
4	29-Aug-96	10:46:45	7105	02565	00237
5	01-Sep-96	10:52:31	7148	02565	00280
7	19-Nov-96	11:09:44	8279	02565	00409
9	23-Nov-96	10:43:52	8336	02565	00466
10	26-Nov-96	10:49:35	8379	02565	00008
11	29-Nov-96	10:55:20	8422	02565	00051
12	02-Dec-96	11:01:03	8465	02565	00094
13	05-Dec-96	11:06:47	8505	02565	00137

Chilbolton Radar data collection

Chilbolton quick-looks were obtained from the RAL under the NERC data grant for each date that ATSR2 was available from 1/8/98-31/3/99 shown in Table 3 above. Two unsuccessful NERC grants were written to try to obtain a more extended time series. The 94GHz radar was operated near continuously from the end of October 1998 through to the end of March 1999. The CLARE98 campaign took place between 3-23 October 1998 centred around the Chilbolton site. This ESA-sponsored campaign included 15 groups from around Europe making intensive in situ measurements from 3 aircraft of cloud properties as well as the Chilbolton 3 and 35GHz radar operating and a 94GHz radar from GKSS.

Wide-angle sky digital imagery data collection

A pair of Kodak Megaplug digital cameras with both 16mm and 8mm lenses and associated PC-NT computers were loaned by a colleague at UCL and installed at the Chilbolton Radar Facility on the roof of two Portakabins known as the receive and transmit towers for the period 20-23 October 1998 during the ESA sponsored CLARE98 campaign. These locations were exactly 500m apart and the precise camera locations were determined using differential GPS.

Each camera had a separate NT PC and framegrabber board. The cameras were used to obtain a total of around 4 hours of continuous stereo digital imagery. These images

were acquired at time sampling up to every 10 seconds due to the rapid transit of clouds across the sky. Neither cameras had access to a sun occulter.

Almost 3 Gbytes of data were obtained which was beyond the capacity of the NT PC hard disks to store. Hence, each night these data were downloaded onto a removable disk and these data were eventually transferred onto the Unix systems employed for the project. These data were then catalogued and then JPEG quick-look versions were created from which a CD-ROM was created. This CD-ROM included a real-time web-based display to use the JPEG quick looks to access the original TIFF formatted imagery. This was the only way that the stereo sequence could be viewed in (side-by-side) stereo and the quality of the imagery assessed.

Several problems were found using this quick-look facility, including (1) the NT PC clock would drift causing the stereo data to go out of synchronisation; (2) the contrast would vary enormously from image pair to image pair due to the effects of the sun and the rapid motion of the clouds; (3) when the sun emerged from behind a cloud, the images would very quickly saturate. An example is given below in Figure 8.

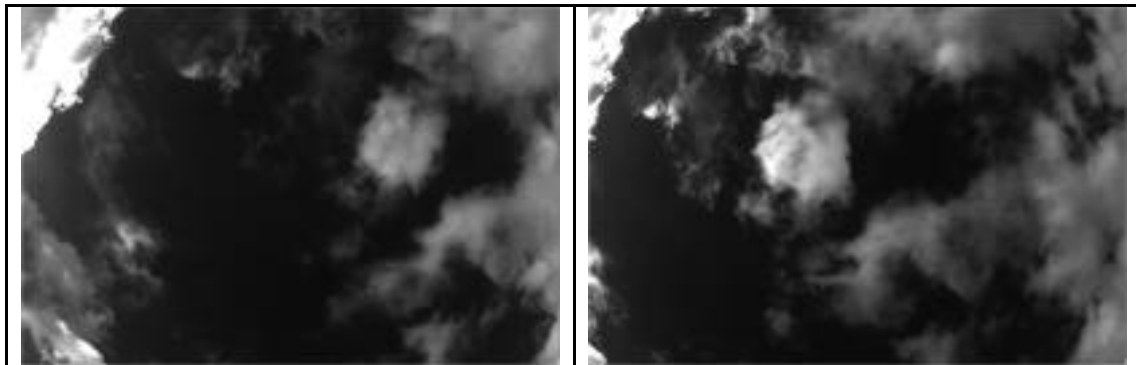


Figure 8. Left and right views 500m apart taken by the Kodak Megaplug digital cameras of clouds during CLARE98 (23.10.98) showing the effects of differences in contrast, synchronisation and the lack of a sun occulter.

Each camera was carefully geometrically calibrated using the UCL camera calibration facility. This permitted the calculation of 3D co-ordinates from a stereo-pair.

Status of the NASA EOS Terra mission

The June 1998 launch-date for the NASA EOS Terra spacecraft (renamed from the EOS AM-1) which was slipped last year to June 1999 has slipped further to December 1999. Work has therefore focused on an analysis of AirMISR data acquired during the NASA-NOAA FIRE-ACE campaign centred around the Barrow ARM site.

AirMISR data acquired during the FIREIII campaign in Alaska

NASA and the ARM (Atmospheric Radiation Measurement) project from the US Department of Energy held a joint aircraft and field campaign close to the Barrow (ARM) site. In May and June of 1998, the Airborne Multiangle Imaging Spectro-Radiometer (AirMISR) participated in the FIRE Arctic Cloud Experiment (ACE). During the FIRE ACE experiment, 13 flights (each with 4 to 8 data acquisitions or

runs) were attempted over Point Barrow Alaska or the Surface HEat Balance of the Arctic Ocean (SHEBA) ice station. AirMISR flies on the NASA ER-2 aircraft and has a single pushbroom (line imagining) camera of the same design as the nine cameras on the MISR satellite-based instrument. High resolution images are obtained by this camera in four narrow spectral bands centered at 446, 558, 672, and 866 nm. During the FIRE ACE experiment, the camera was adjusted to reproduce the nine view angles which will be obtained by the satellite (that is a nadir view plus 26.1, 45.6, 60.0, and 70.5 degrees forward and aft referred to hereafter as An, Bf or Ba, Cf or Ca, Df or Ca depending on whether the look was forward or aft). Image resolution is approximately 7 meters at nadir (with a cross track image width of approximately 10 km) and 21 meters at 70.5° AirMISR Red channel data was processed by JPL into 9 registered looks on the ellipsoid at 27.5m resolution and radiometrically calibrated into radiance units using pre-flight calibration. This is the so-called level 1B2 format. A set of example images is shown in Figure 9. The 14-bit digital signal means that AirMISR is able to see subtle contrast variations which are not visible to the human flight at the time of overflight.

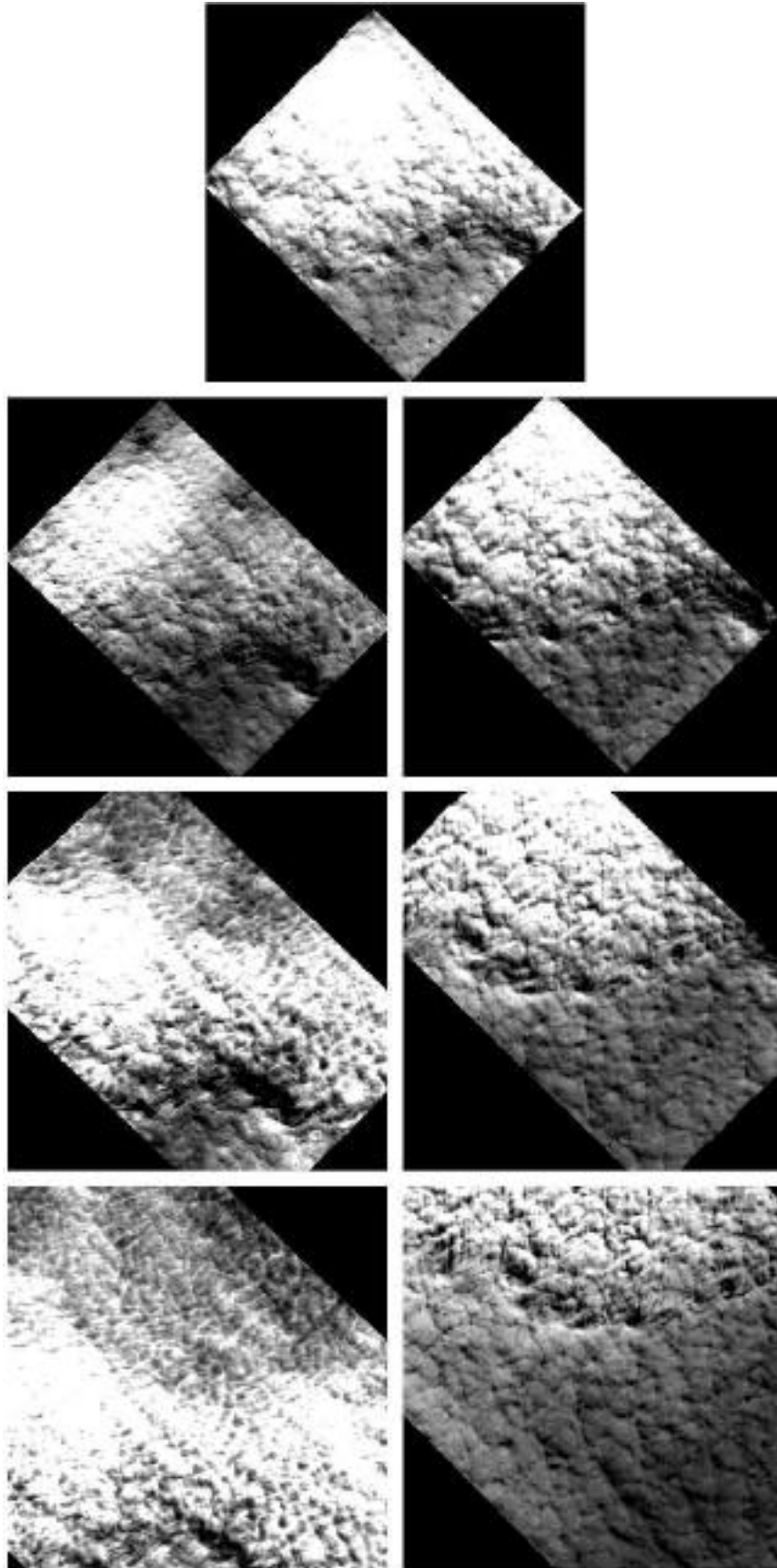


Figure 9. AirMISR Red channel data from An, Af, Aa, Bf, Ba, Cf and Ca reading from left to right and top to bottom.

DLR-IPE

Status of the MOSM-PIRODA data collection

Since its start in September 1996 MOMS on MIR has produced more than 250 image strips of about 20 to 30 images length covering about 50 million km₂ of the Earth land surface. The length of one scene is about 80 to 90 km. The MOMS data collection ended in late August 1999, when MIR started to be prepared for an unmanned sleeping status planned to last until February 2000 as (a preliminary) date for the final decision about its future.

MOMS on MIR is facing a time delay of many months between image acquisition and tape delivery to the ground. Up to now 165 image strips have become available as quick looks lasting from the beginning of the MOMS/MIR mission to 10 Feb. 99.

Over 60% of the data were taken in mode D suitable for CLOUDMAP, that is with the blue and near infrared nadir looking channels and the fore- and aft-looking panchromatic stereo channels, all at an identical ground pixel size of 15 to 18 m (depending on the actual height of MIR). With the exception of the desert areas most of the MOMS image strips do contain clouds (with about 25 % cloud cover in the total mean). All quicklooks up to April 1998 were checked for cloud content including cirrus clouds and contrails on a image by image basis.

The radiometric quality of the MOMS images suffers from an electronic temporal instability in the on-board signal processing chain, causing a time variable striping of the images. In the meantime more than 50 image strips have undergone radiometric correction (destriping with an empirical algorithm): The draw back for CLOUDMAP is, that image processing is concentrated on cloud free images (low priority for CLOUDMAP) and sufficiently cloudy images for CLOUDMAP have become available only quite recently. An overview of the radiometrically corrected image strips of the year 1998 is given in **Table 5**.

Up to now thirteen cloud dominated MOMS images have been selected for CLOUDMAP with regard to cloud type, cloud layering, Cirrus and especially contrail content and further for appearance of cloud and contrail shadows and shadow drift. These images have been subjected to radiometric correction (destriping) and partly also geometric correction. Certain parts of these images have been selected as a set of reference scenes for testing the performance of stereo evaluation algorithms at specific situations of cloudiness. The most important are:

- 1 single layer cloud fields with shadow,
- 2 multi-layer cloud fields (without shadow),
- 3 persisting contrails and
- 4 contrails with contrail shadow.

Data take NR, centre co-ordinates, unit time and local time of the MOMS cloud images are given in **Table 6** together with some information on cloud content and surface type.

Table 5. Decalibrated MOMS/MIR Data Takes, Available at DLR-OE
Oberpfaffenhofen. Status: as of August 1999

DT	M	Location	Date	Day	start Long	end Long	start UT	end UT	start LT	end LT	image Nr	Sunel
T083C	A	Bristol Ankara	14.03.97	73	-4	34	9,0	9,2	8,8	11,5	4-74	25-50°
T085F	A	Chile/Argentine	21.01.98	21	-72	-54	14,5	14,6	9,7	11,0	5-52	55-65°
T0865	D	Calais/BlackSea	06.03.98	65	-1	28	9,7	9,8	9,7	11,7	1-22	25-39°
T086F	D	Iran/SriLanka	13.03.98	72	62	81	6,2	6,3	10,3	11,7	1-26	47-77°
T0873	D	Chile/Argentine	17.03.98	76	-69	0	0,0	0,0	-4,6	0,0	1-23	66-52°
T0875	D	Argentine	18.03.98	77	-69	-57	17,0	17,0	12,4	13,2	1-14	54-47°
T0879	D	Venez.nBrazil	20.03.98	79	-69	-61	13,2	13,3	8,6	9,2	1-18	36-45°
T087B	D	Chile/Argentine	21.03.98	80	-69	-59	15,6	15,6	11,0	11,7	1-14	47-48°
T0881	D	Chile/Argentine	24.03.98	83	-72	-60	14,1	14,2	9,3	10,2	1-18	39-41°
T0887	D	Chile/Brazil	30.03.98	89	-75	-47	19,8	19,5	14,8	16,4	1-43	37-32°
T0891	D	Guinea/Lybia	07.04.98	97	-10	15	14,8	14,9	14,1	15,9	1-45	60-20°
T0893	D	Togo/Turk.BISea	08.04.98	98	-2	37	13,8	14,0	13,6	16,5	2-58	66-20°
T0899	D	nwMex/Missouri	09.04.98	99	-111	-94	22,1	22,2	14,7	15,9	1-24	-?
T089B	D	Sudan/Kasachst.	10.04.98	100	24	58	11,8	11,1	13,4	14,9	1-60	71-20°
T089F	D	Sudan-Aral-Altai	13.04.98	103	33	88	10,5	10,7	12,7	16,6	1-48	75-20
T08A1	D	nwIndia-eMong.	14.04.98	104	68	126	7,9	8,2	12,5	16,6	1-61	75-20
T08A3	D	Jemen-eMongol.	15.04.98	105	48	117	8,4	8,7	11,6	16,5	1-74	80-20
T08A9	D	sPortug.-ePoland	19.04.98	109	-11	23	12,3	12,4	11,5	13,9	2-34	62-43
T08AB	D	Aethiop./Kuweit	20.04.98	110	37	52	6,5	6,6	8,9	10,1	6-32	45-61
T08AD	D	Bordeaux-ePol.	21.04.98	111	-2	22	11,9	12,0	11,7	13,4	3-24	56-43
T08B1	D	Alma-Ata	25.04.98	115	73	82	4,8	4,8	9,7	10,3	1-12	49-51
T08B5	D	Alg.-Vienna-Pol.	27.04.98	117	-9	24	8,9	9,0	8,3	10,6	1-34	36-50
T08B7	D	France-Poland	28.04.98	118	-2	25	9,5	9,6	9,4	11,3	1-25	44-51
T08B9	D	Gibr/Nice/Slovak	30.04.98	120	-6	22	7,5	7,6	7,1	9,0	1-32	21-41
T08BB	D	England-Turkey	01.05.98	121	-6	28	11,3	11,4	10,9	13,2	1-32	52-58
T08BD	D	Wales-BlackSea	02.05.98	122	-6	30	10,2	10,3	9,8	12,3	1-31	46-60
T08BF	D	Pyrenees	03.05.98	123	-5	5	12,4	12,6	12,1	13,0	1-12	62-64
T08C3	D	Wales-Krim	05.05.98	125	-6	36	8,8	8,9	8,4	11,3	1-35	50-70
T08C5	D	wIreTurk.Oman	08.05.98	128	-15	55	9,0	9,2	8,0	12,8	1-33	37-64°
T08CE	D	Aral-BanglDesh	13.05.98	133	60	89	4,0	4,1	8,0	10,0	1-37	28-36°
T08DC	D	Kauk Caspian	10.06.98	161	41	48	12,4	12,4	15,1	15,6	1-11	40-47°
T08DE	D	swAegypt-Baku	11.06.98	162	25	50	11,2	11,4	12,9	14,7	1-35	77-52°
T08E2	D	Sicily-eVolga	13.06.98	164	15	38	12,4	12,5	13,4	15,0	2-28	69-47°
T08E6	D	PortLkConstUkr	15.06.98	166	-10	27	13,4	13,5	12,8	15,3	1-34	70-44°
T08E8	D	swAeg.-neBaku	16.06.98	167	28	55	9,2	9,4	11,1	13,0	1-35	81-70°
T08E9	D	Kasachstan	16.06.98	167	75	84	9,5	9,5	14,5	15,1	2-09	?
T08F3	D	Nice-SWUkraine	21.06.98	172	9	23	10,5	10,5	11,1	12,0	1-16	66-64°
T08F4	D	Kasachstan	21.06.98	172	65	91	10,6	10,7	15,0	16,8	2-22	45-30°
T08F6	D	Netherl-swCaspi	21.06.98	172	2	49	13,6	13,8	13,8	17,1	3-43	55-25°
T08FC	D	Aeg.AralChina	24.06.98	175	30	135	5,7	6,1	7,7	15,1	3-85	60-31°
T08FE	D	Portugal-Poland	25.06.98	176	-11	23	9,4	9,5	8,7	11,1	1-35	45-61°
T0902	D	wIre-Oman	27.06.98	178	-12	59	12,2	12,4	11,4	16,4	1-75	62-30°
T0904	D	BretTurk.Somal	28.06.98	179	-4	51	12,7	13,0	12,5	16,4	1-73	64-26°
T0906	D	Bisk-Aral-Tibet	29.06.98	180	-2	74	8,5	8,7	8,4	13,7	1-66	40-65°
T0908	D	Baku-Aral-Kasac	01.07.98	182	49	77	3,3	3,4	6,5	8,6	1-49	27-60°
T091B	D	Bret.-Calabria	10.07.98	191	-4	20	8,2	8,3	7,9	9,6	1-25	35-53°
T091D	D	Kasachstan	10.07.98	191	55	78	4,1	4,3	7,8	9,5	1-25	31-49°
T0940	D	Ethiopia-Afgan.	18.08.98	230	36	74	6,0	6,2	8,4	11,1	18-52	35-61°
T0957	D	England/Chilbolt	16.10.98	289	-6	2	14,5	14,5	14,1	14,7		22-19
T095D	C	eastZaire	11.11.98	315	25	29	8,1	8,1	9,8	10,1	5-16	54-61°

					start	end	start	end	start	end	image	
DT	M	Location	Date	Day	Long	Long	UT	UT	LT	LT	Nr	Sunel
T0964	D	Chile-Argentina	14.11.98	318	-74	-65	15,7	15,8	10,8	11,4	2-13	69-67°

N.B. Colour highlights refer to the MOMS strip for **Figures 10-11**, **Figures 12-15**, **Figure 16** and **Figures 17-18**

Table 5 has the following key:

- Column 1: data take NR of the image strip,
 - Column 2: NR of operational mode (modes not suitable for CLOUDMAP are printed bold),
 - Column 3: location of the Data take NR,
 - Column 4: date of the data take,
 - Column 5: day of the year of the data take,
 - Column 6: longitude of the start of the image strip,
 - Column 7: longitude of the end of the image strip,
 - Column 6: Unit Time of the start of the image strip,
 - Column 8: Unit Time of the end of the image strip,
 - Column 9: Local Time of the start of the image strip,
 - Column 10: Local Time of the end of the image strip,
 - Column 11: processed images of the data take,
 - Column 12: range of solar elevation in the image strip.
- (bold printed LT values for start or end in column 9/10 indicate, that the covered LT-range is crossing either ATSR/ERS-2, MOS/IRS-P3 or AVHRR/NOAA-14).**

Table 6. List of radiometrically calibrated MOMS cloud scenes selected for testing the stereo matching algorithms at DLR-IPE.

DT	M	NR	location	Date	Long	Lat	UT	LT	clouds	shadow	surface
T07F5	B	02	Cape Town	13.10.96	17,4	-37,2			Cirrus	no	sea
T0838	C	30	North-Adria	13.03.97	13,9	44,8	10,0	9,1	Cirrus	no	sea
T0846	D	04	Patagon./Argentina	01.04.97	-71,4	-37,2			Cumulus	yeso	land
T083C	A	32	West-Austria	14.03.97	14,3	47,7			contrail	no	land
T08B3	D	19	Bavaria	26.04.98	12,0	48,6	13,2	12,4			
T08C5	D	03	South-England	08.05.98	-4,9	50,7	8,9	9,2	contrails	no	sea/land
T08C5	D	04	South-England	08.05.98	-3,5	50,4	8,9	9,2	contrails	no	sea/land
T08C5	D	05	South-England	08.05.98	-2,2	50,2	8,9	9,1	Cirrus	no	sea
T08E2	D	16	Romania	13.06.98	27,9	44,5			contrail	drift	land
T08FE	D	17	France/Switzerl.	25.06.98	5,8	46,6			contrail	drift	sea
T08FE	D	18	France/Switzerl.	25.06.98	7,0	47,0			contrail	drift	land
T0908	D	23	West of Baku	01.07.98	47,6	39,6	3,3	6,5	Cumulus	no	land
T0908	D	24	West of Baku	01.07.98	48,5	40,2	3,3	6,5	Cumulus	no	land

N.B. Colour highlights refer to the MOMS strip for Colour highlights refer to the MOMS strip for **Figures 10-11**, **Figures 12-15**, **Figure 16** and **Figures 17-18**

Table 6 has the following key:

- Column 1: Data take NR of the image strip,
- Column 2: NR of operational mode,
- Column 3: Image NR within the data take,
- Column 4: Location of the image,

Column 5: Date of the data take,
Column 6: Longitude of the image centre,
Column 7: Latitude of the image centre,
Column 8: Unit Time of the image centre,
Column 9: Local Time of the image centre,
Column 10: Dominating cloud type within the image,
Column 11: Shadow visibility and (remarkable) shadow drift,
Column 12: Surface type (land or sea).

The **Figures** in this report show some of the selected reference cloud scenes. These scenes are presented as two different views (Nadir and one stereo channel or two stereo channels) either side by side to demonstrate shadow drift or as red/green anaglyph images to provide a vivid impression of the 3D structure and distribution of different cloud fields including aircraft contrails of all ages. The anaglyph images need to be viewed using red/green glasses with the red glass at the right eye. The virtual depth of the clouds, contrails or the Earth surface of these images is (in most cases) much deeper than the paper position! Many images are subsampled by a factor of four, that is with a ground pixel size of 60 m instead of the original 15 m to give an overview of the image at a tolerable image size.

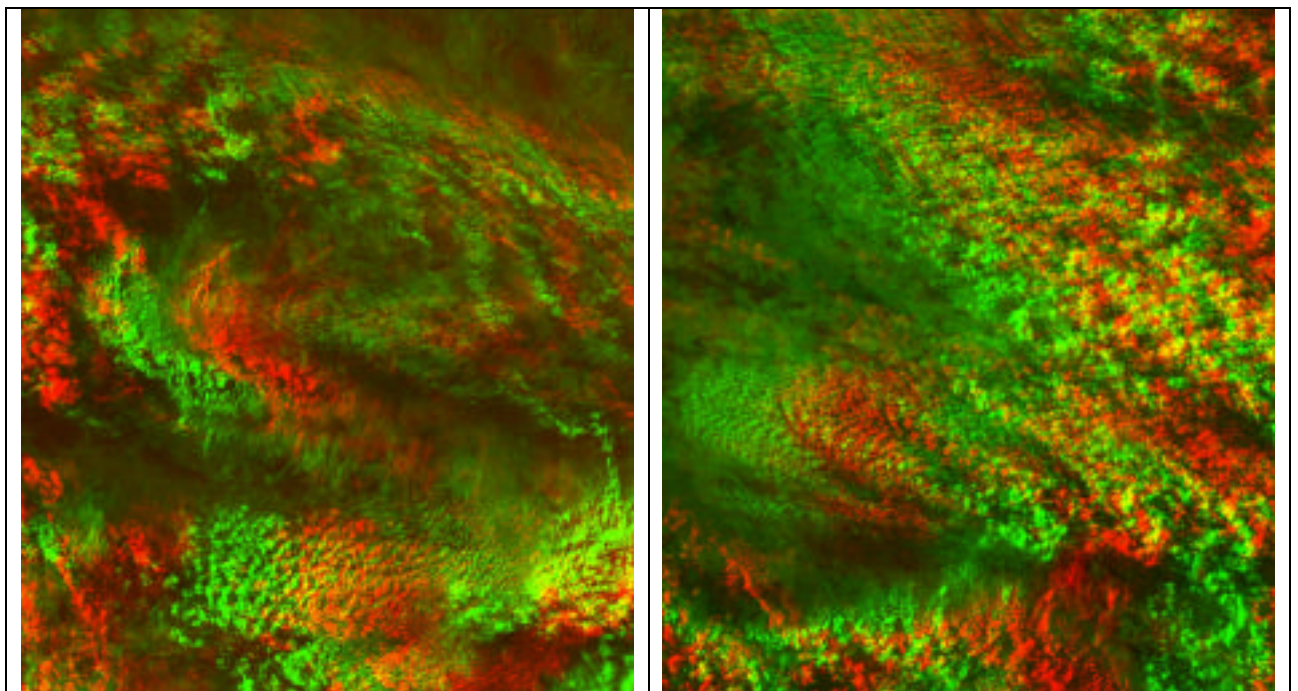


Figure 10 shows an anaglyph view of a nearly complete anaglyph views (4000 by 4000 pixel out of 5800 by 5920 original image size) of two adjacent MOMS images (23 and 24) of data take T0908 west of Baku with multi-layer cloud fields over land. Figure 10 (left) is combined from channels 1 and 6 and Figure 10 (right) from channels 4 and 7.

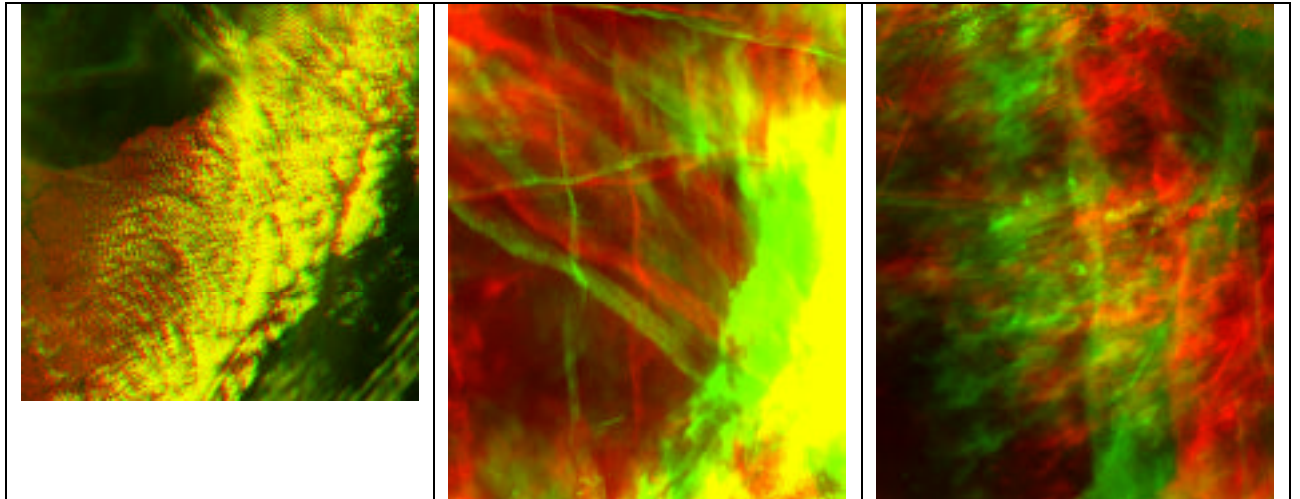


Figure 11 present similar red/green anaglyph views of three adjacent MOMS images (03 to 05) of data take T08C5 west of the Chilbolton test site in South England. The image 03 shows a single layer field of small Cumuli over land as the dominating feature. The image 05 is dominated by Cirrus type clouds over sea. All images contain aircraft contrails, but the image 04 shows all types of contrails from status nascendi to worn out old ones, mainly in a Cirrus environment over sea. Optically thick clouds are saturated, since the images were stretched to enhance the contrail and Cirrus clouds.

The Figures 10 and 11 are about 70 by 70 km_ and resampled at a factor of four (60 m pixel).

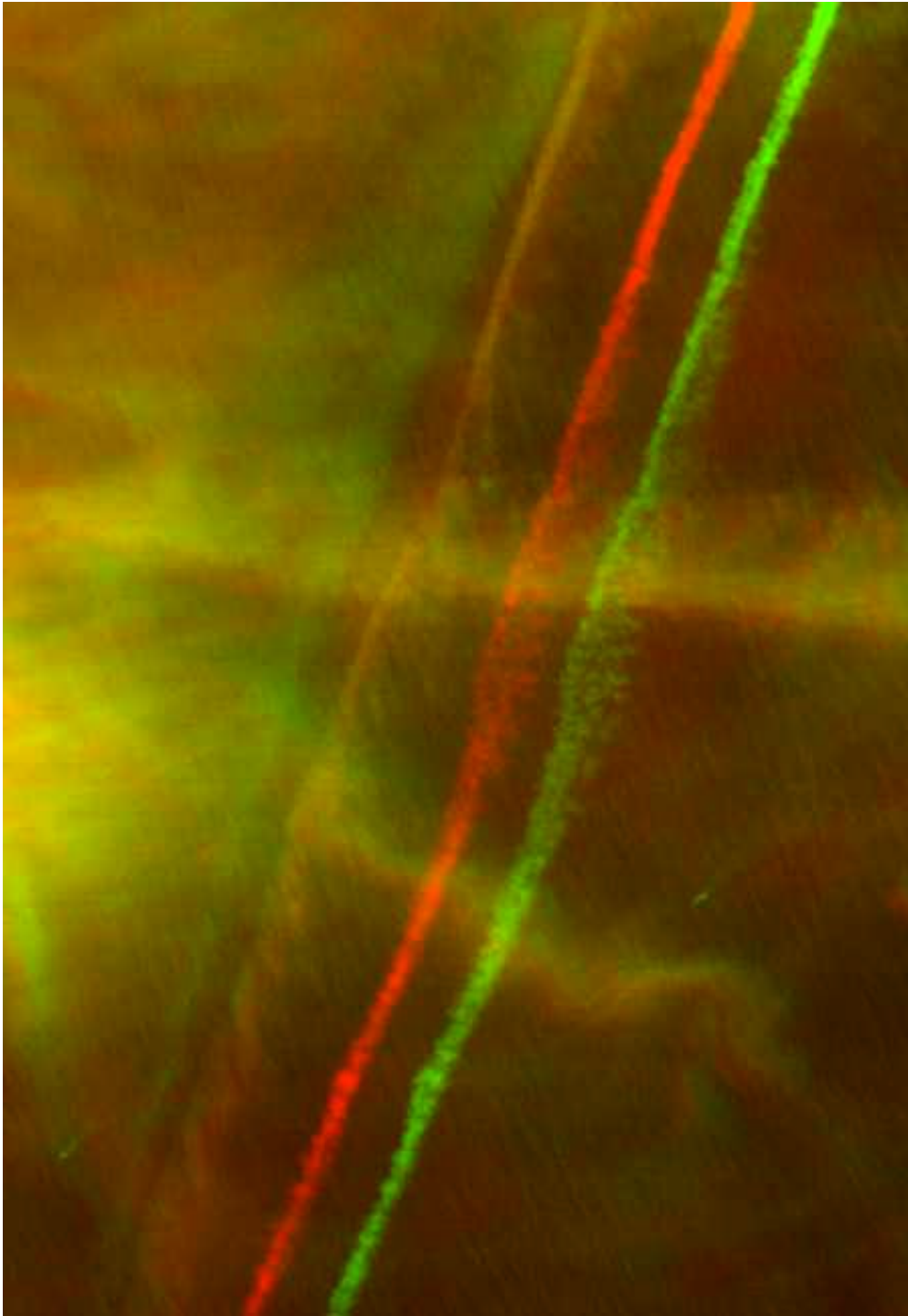


Figure 12 shows an anaglyph view of a Cirrus cloud and a persisting contrail over sea. The waves of the sea surface are visible in this image. The example is from image 04 of the data take T08C5.



Figure 13 is a side by side presentation of the stereo channels 6 and 7 of a persistent contrail over land casting a clearly visible shadow. The clearly visible displacement of the shadow position within the 40 seconds time interval between the two images by strong winds leads to a 16% difference between the true and the apparent stereo height of this contrail! The example is taken from the MOMS image 16 of the data take T08E2

The contrails of Figures 13 and 14 demonstrate that the spatial structure of persisting contrails is stable enough to allow for a visual stereo impression and machined stereo matching

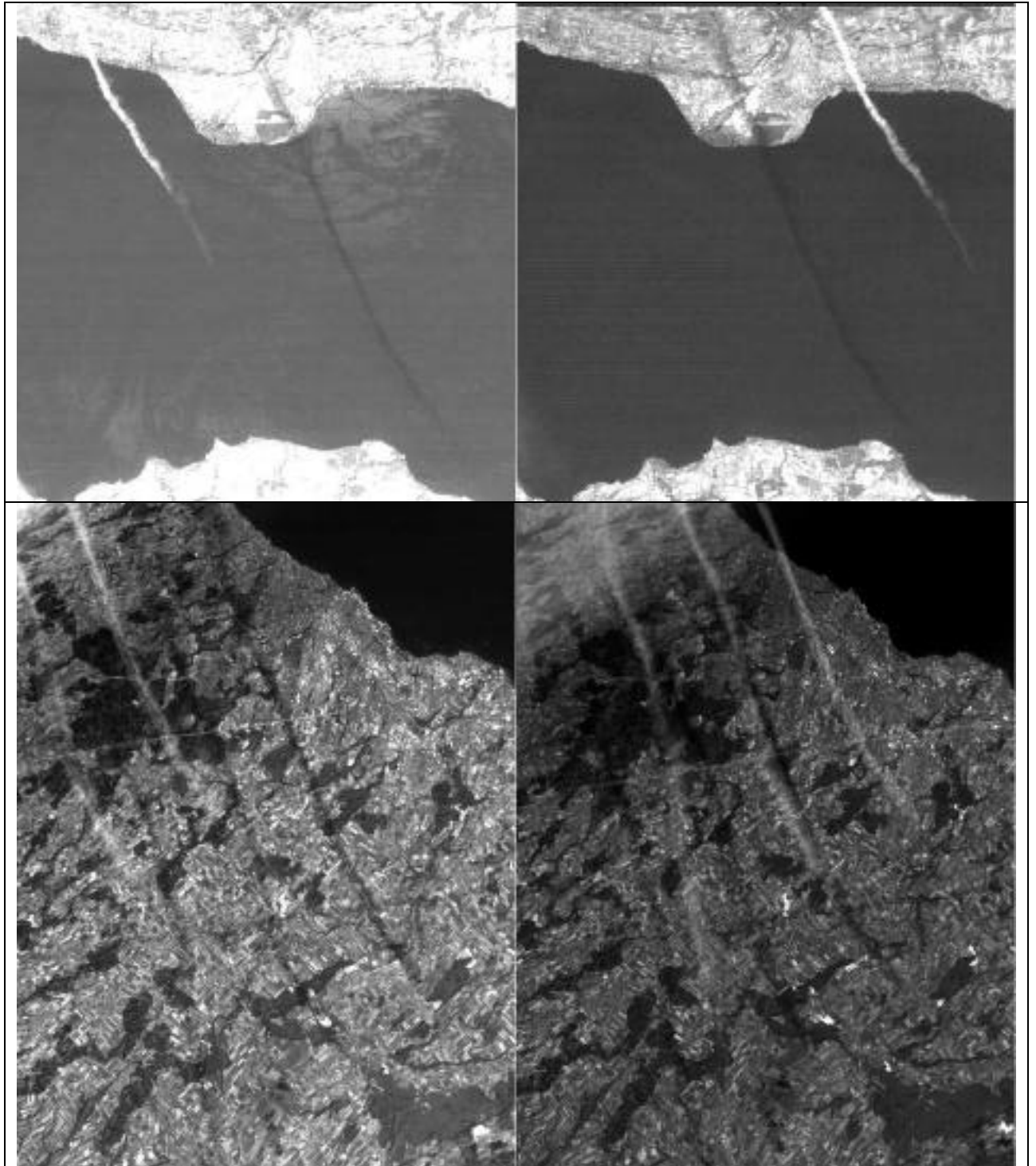


Figure 14 are side by side presentations of the stereo channels 6 and 7 of persisting contrails over land and sea casting a clearly visible shadow associated with shadow drift. The example is taken from the MOMS image 16 (upper) and 17 (lower) of the data take T08FE

The contrails of Figure 14 show that the shadow analysis can be used to derive true height and drift not only for clouds but (sometimes) also for (persistent) contrails!

DLR-IPE identified the crossing points between the orbital plane of MIR and the orbital planes of ATSR-2/ERS-2, AVHRR/NOAA-14 and MOS/IRS-P3 for all existing MOMS/MIR data takes and additionally for all MOMS-D2 crossings with AVHRR/NOAA-14.

A quantity of more than 90 out of 250 MOMS data takes was identified as containing at least one suitable crossing point. A detailed analysis of the actual time gaps at the crossing points is delayed because of incomplete (non-unique) data archiving of the MOMS ground strips metadata (according to requirements from surface science only longitude, latitude and solar elevation were stored as ancillary information, but not the times of data taking!).

ETH

Stereo MOMS data collection

The University of Stuttgart provided two stereo pairs taken on March 14th, 1997, during the PRIRODA mission from the Russian MIR station. The data take number is 083C, scenes 25-26 (see **Figure 15**) and 27-30. The sensor used was MOMS-2P (shown in **Figure 16**), consisting of stereo and multispectral modes, for a total of 5 optical systems that record with CCD linear sensors. As shown in **Figure 17**, in the stereo module the nadir-looking sensor (HR 5) has a ground resolution of 6 meters and the 2 sensors forward and backward oriented (STEREO 6 and 7) have a ground resolution of 18 meters. The time delay between the acquisition of the forward and backward images is about 40 sec. The multi-spectral sensors (MS 1/2 and MS 3/4) have a ground resolution of 18 meters. The flight height is about 400 km.

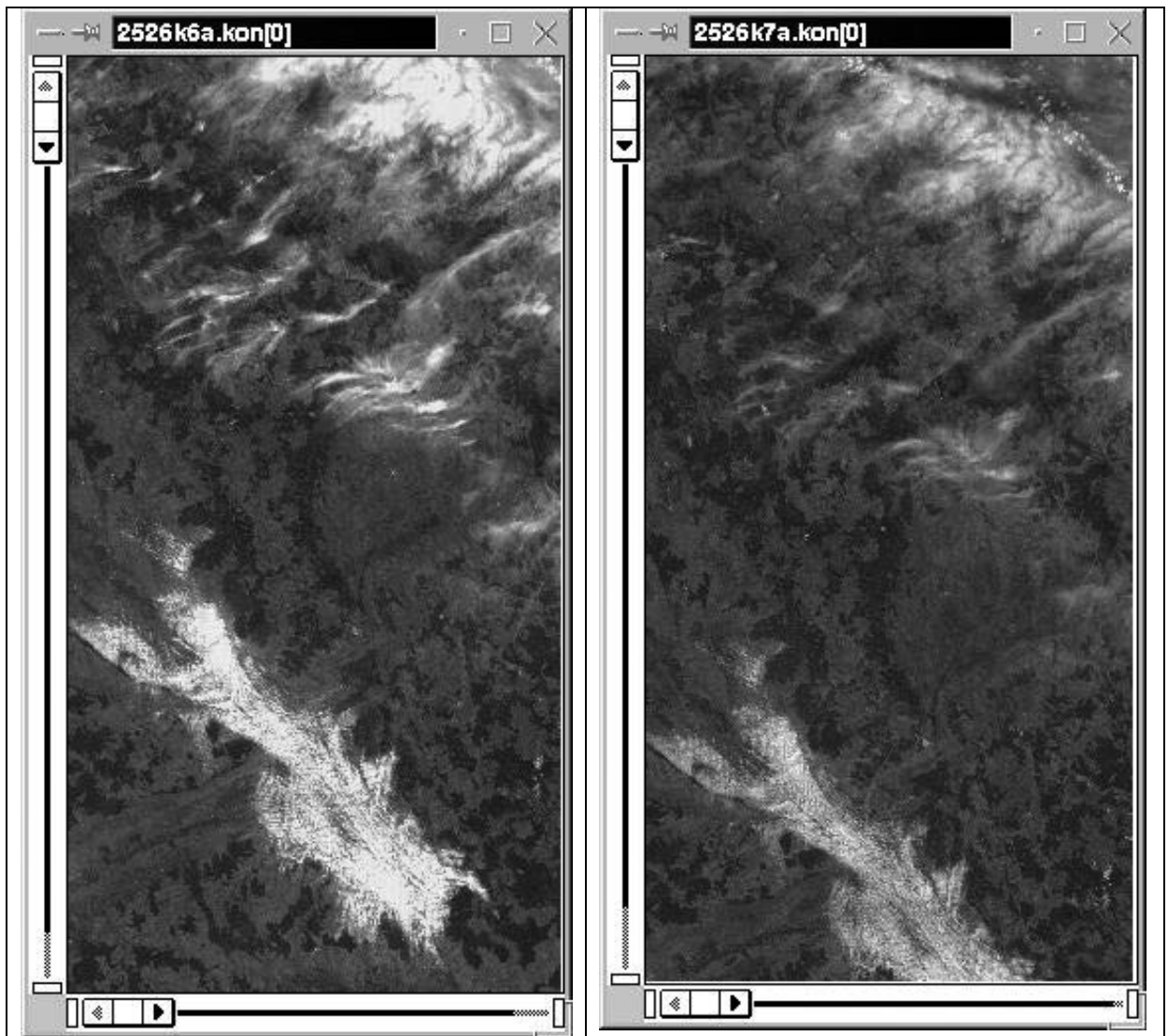


Figure 15: MOMS Stereo pair, scenes 25-26. On the left is the aft view, on the right the forward view. The flight direction is from left to right.

(<http://192.111.33.173/ATSRNRT/>). All ERS-2 orbits received at Tromso satellite station (normally 10 of 14 per day) are available in this service.

With this new interface, we have downloaded a couple of scenes over Switzerland in July and August 1999 where the resulting cloud-top heights can be compared with radiosonde and surface station data from the Swiss Meteorological Institute. During the MAP-SOP (9th September to 15th November 1999), it is planned to download all the available scenes for the target area "Rhine Valley" as part of the MAP field campaign (see section 3.3.2.3.4).

Ground-based whole-sky stereo digital images

Ground-based photogrammetric cameras have been used at various sites in the past to measure cloud parameters and are potentially very valuable for this project for validation purposes (First Interim Report, section 3.2.1.8). Unfortunately, there were some problems (illumination differences, synchronization) with the cameras employed at Chilbolton during CLARE98 which do not allow the derivation of many products from these images (see section 3.3.2.1.3). Therefore, new image pair series were taken for use as validation data of satellite-derived CTH's of preferably thin clouds.

A few series of stereo cloud images were already taken with two KODAK DCS460 colour digital CCD cameras at Zurich, Switzerland during one week in August 1999. **Figure 18** shows a stereo pair taken with a 18mm lens and a horizontal distance of about 800m.

During three weeks in October 1999, more series will be captured, both with a 18mm wide-angle and a 8mm fish-eye lens. The measurements will take place in the MAP-Target Area "Rhine Valley", Switzerland (see also 3.2.5.4).

The experimental setup consists of the same two Kodak DCS460 colour digital CCD cameras used in August 1999, with a horizontal distance of 850 meters, both connected to a laptop for camera control and image storage and to a GPS receiver for high-precision time synchronization.

Both a 18mm lens and a 8mm fish-eye lens are used for the measurements to compare the advantages and disadvantages of a relatively small field of view (18mm) against whole sky images which are however strongly deformed at the borders (fish-eye) (**Figure 19**). The time interval between subsequent images for each sensor is adapted to the current meteorological situation and is between 10 seconds and about 2 minutes.

A special moving device (sun occultator) was used to avoid imaging the sun and problems like blooming and smearing of the CCD sensor (**figure 20**).

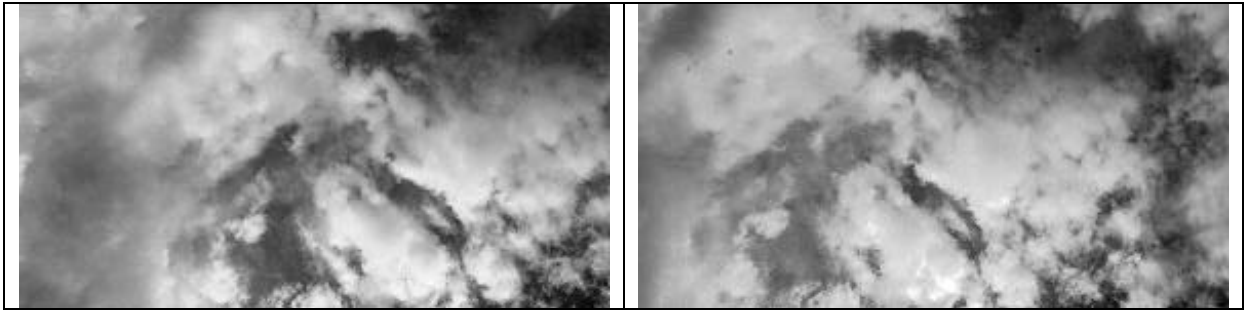


Figure 18: Stereo pair with 18mm lens, 08/08/1999 17:00 GMT; horizontal distance: 800m. Because of the late time of the day, no sun occulter had to be used.

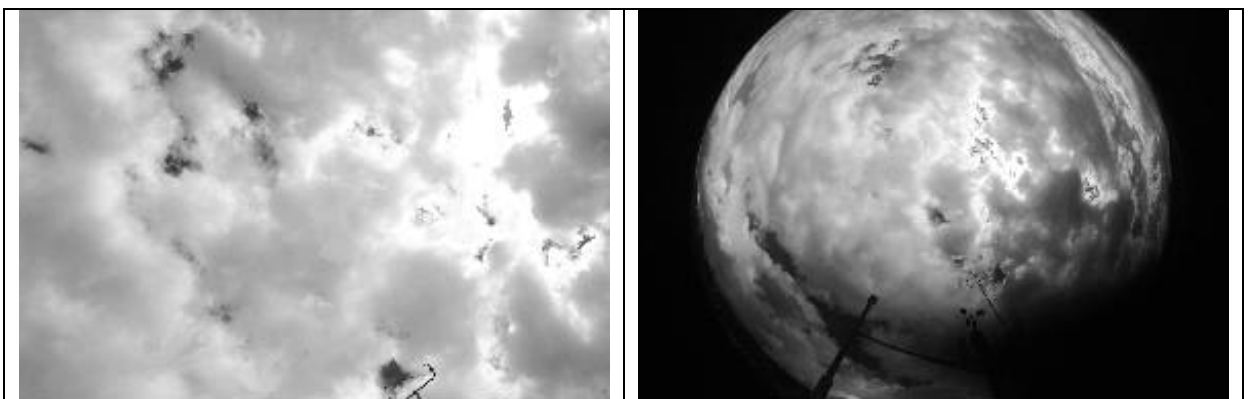


Figure 19: Left: image taken with 18mm lense; right: image taken with 8mm fish-eye lens. Time difference between these two images is 60 seconds.



Figure 20: Sun effects in images without (left) or with (right) a sun occulter.

MAP Campaign

The Mesoscale Alpine Programme (MAP) is an international research initiative devoted to the study of atmospheric and hydrological processes over mountainous terrain. It aims at expanding our knowledge of weather and climate over complex topography. (<http://www.map.ethz.ch>)

The operation period is 7 years from 1995 to 2001. Within this programme duration, there are three levels of observing periods:

- General Observing Period (GOP): 1st October 1998 to 30th November 1999
- Special Observing Period (SOP): 9th September to 15th November 1999
- Intensive Observing Periods (IOP's): short periods of several days within the SOP with even more enhanced observations.

The SOP is the largest observational field program of meteorology over the Alps since ALPEX in 1982.

There are three target area, "Rhine Valley" (Switzerland), "Lago Maggiore" (Italy, Switzerland) and "Brennerpass" (Austria) (**Figure 21**). The studies in the target area "Lago Maggiore" are mainly about heavy precipitation events (= wetMAP), the ones in the other two target areas "Brennerpass" and "Rhine Valley" mainly about Foehn related phenomena (=dryMAP).

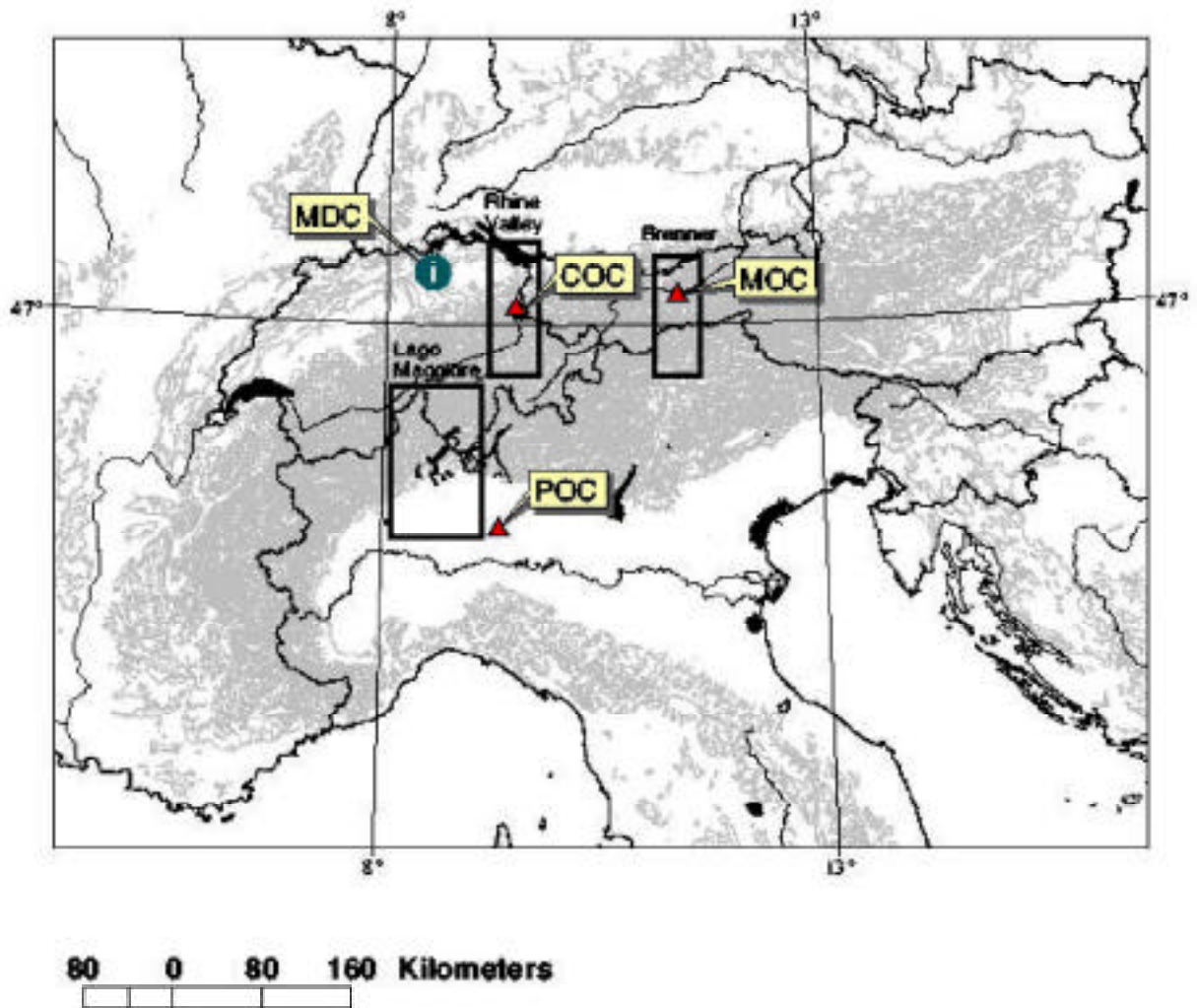


Figure 21: Target Areas of the Mesoscale Alpine Programme (source: <http://www.map.ethz.ch>)

DLR-IPA

AVHRR data collection over Europe for contrail studies

AVHRR-HRPT data is received and archived routinely at the DFD (Deutsches Fernerkundungs- Datenzentrum) at DLR Oberpfaffenhofen. (See **Figure 22**). IPA has direct access to this huge data set. A high speed data connection to DFD's robot archive enables mass production of AVHRR products online and retrospectively through the archive.

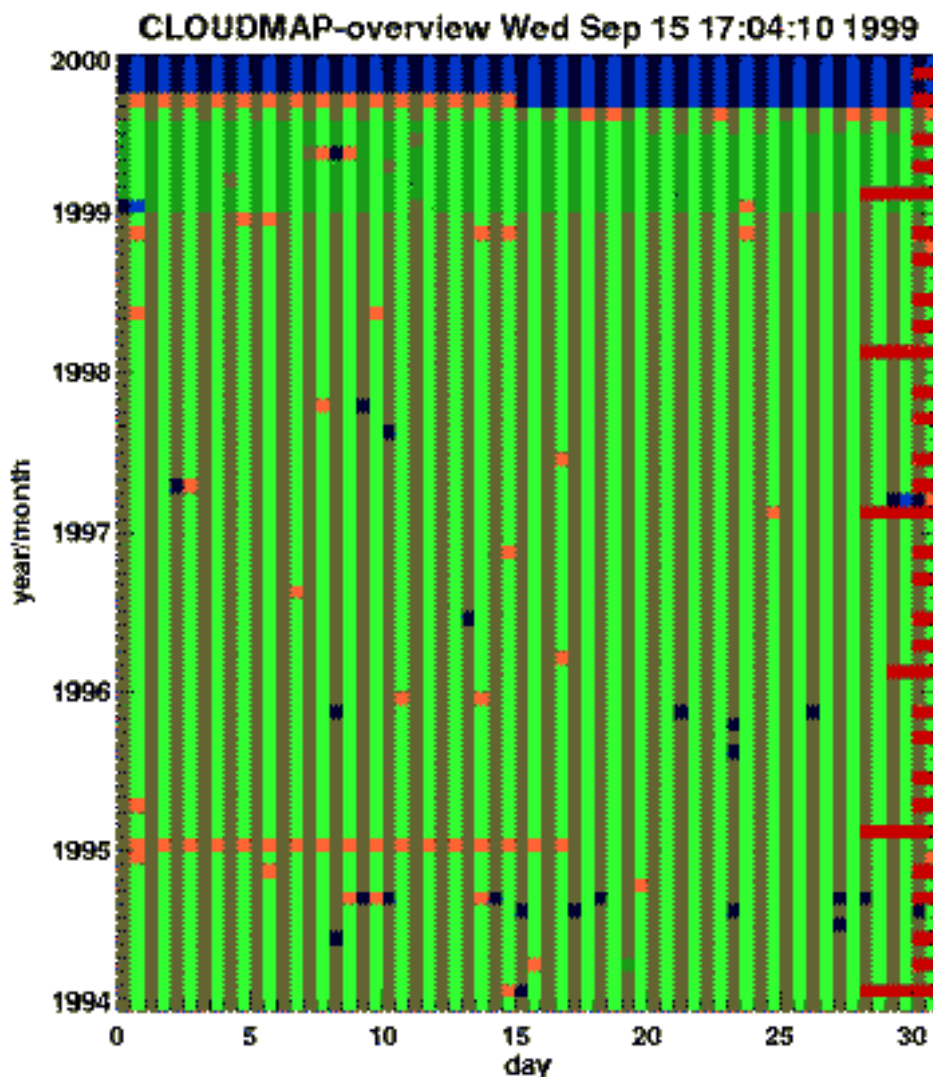


Figure 22. Calendar overview of available and processed AVHRR-HRPT data for 1994 - 1999(valid on Sept. 18 1999). green: already processed, red: not (yet) available, yellow: raw data available in automated archive, dark colours: night passages.

ATSR2 data collection over Europe for contrail studies

For algorithm implementation some ATSR scenes were received. The near realtime data (NRT) connection to Tromsø works, but a fully automated scheme for operational processing needs to be developed. The envisaged ATSR processing needs a filter for selection of certain regions of interest.

Ground-based data collection for contrail validation

A validation of the contrail detection scheme with high resolution images is strongly recommended. Needed are a few coincident scenes to NOAA-14 overpasses as this satellite carries the sensor where the majority of the analyzed data comes from. Due to the fast growth of contrails the time difference must be below 5 minutes. Unfortunately, none of the known MOMS-scenes fulfilled this need.

The CLARE96 data set of skycamera observations from the Netherlands in 1996 was scanned for images showing contrails. Unfortunately no coincidences with NOAA-14 were found.

We hope to achieve such a validation set by the CLOUDMAP co-operation with ETH or UCL. Also other contrail images even outside of Europe are welcome, if a corresponding NOAA-14 pass can be supplied.

DLR-IST

MOS data was supplied by DLR-IPE and AVHRR and ATSR2 images by DLR-IPA

FUB

MOS data collection

The Modular Optoelectronic Scanner (MOS) onboard the Indian Research Satellite (IRS) is the core sensor for the FUB activities within this project. Due to three spectral bands within the Oxygen-A band, which has been firstly realized on a high resolution imaging sensor, cloud top pressure can be derived with multispectral algorithms. A large number of channels in the visible and near infrared spectral range can be used to detect cloud optical, geometrical and microphysical properties.

In the second CLOUDMAP year, the FUB collected MOS tracks from the German Remote Sensing Data Centre (DFD) Neustrelitz for several time periods and locations within the area of the two available receiving stations in Neustrelitz, Germany itself and Mas Palomas, Canary Islands, Spain. (Figure 23 and Figure 24 respectively). The selection of data was led by three major criteria:

- MOS scenes coinciding with measurements during the CLARA 1996 and CLARE 1998 campaigns
- MOS scenes for the cloud microphysical retrieval of stratocumulus clouds in the North Atlantic region
- MOS scenes with a close temporal and spatial correlation with radiosoundings.

CLoudMAP - Cirrus and Contrail cloud-top maps from satellites for Weather Forecasting and Climate Change Analysis :Second Interim Report (1998-99)

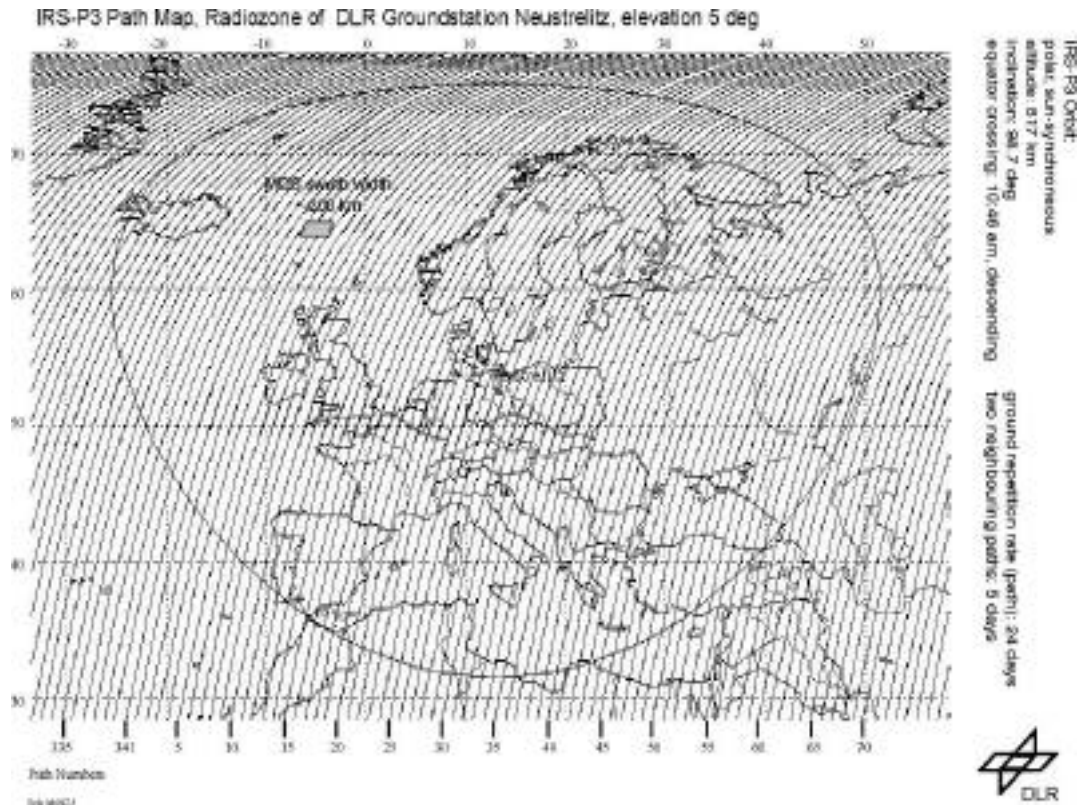


Figure 23: IRS-P3 path map with the radiozone of Neustrelitz, Germany.

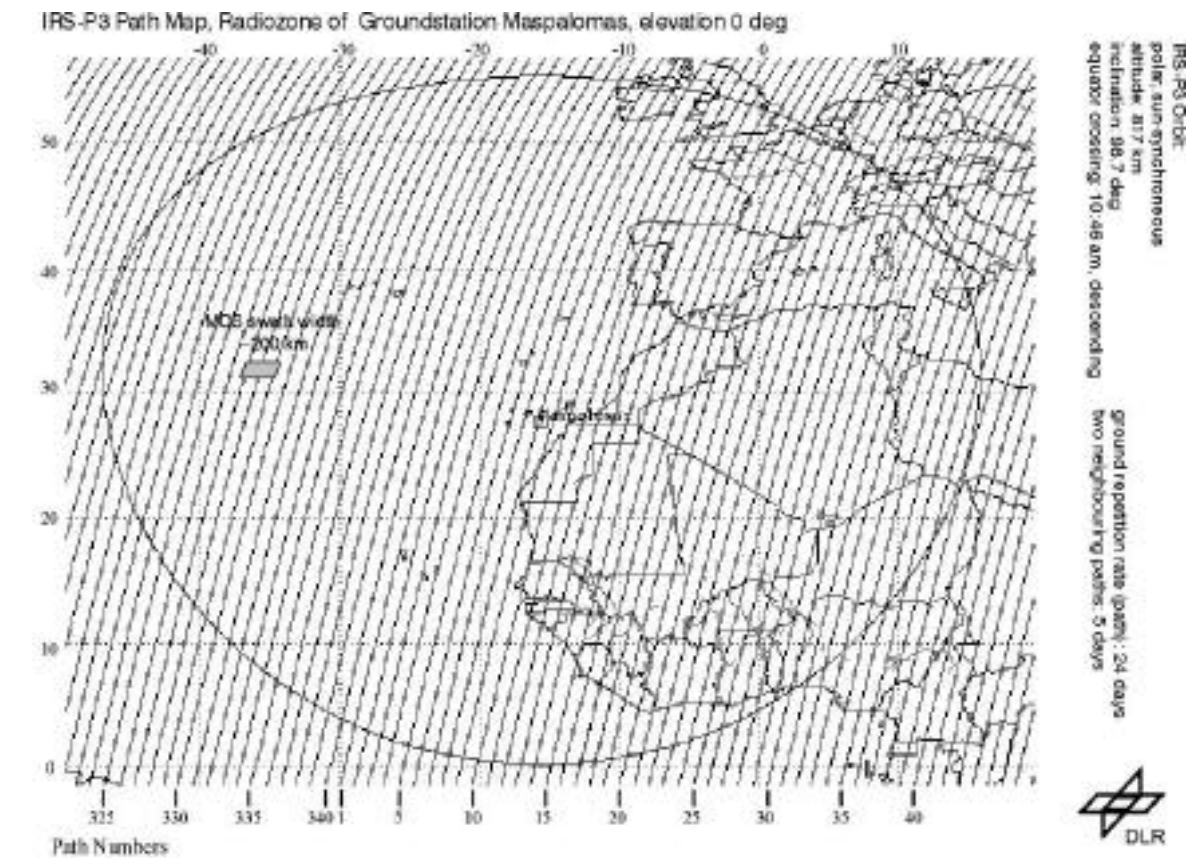


Figure 24: IRS-P3 path map with the radiozone of Mas Palomas, Canary Island, Spain

Radiosondes

The radiosounding data were collected from the Global Telecommunication System (GTS) covering the European area. The main objective is to use the vertical profile of (dew point) temperature especially the altitude of its inversions. The pressure at the inversion altitude can be compared with the MOS cloud top pressure product for a consistency check. A number of 30 radiosoundings could be used for the consistency check given the general requirements (cloudy atmosphere and a close MOS overpass) were fulfilled.

Data processing algorithm development and implementation

UCL

ATSR2 Radiance-to-CTH Processing chain

In the second year of the project, UCL developed a level 1b to level 2 processing chain in IDL for ATSR2 stereo data. This software was supplied to DLR-IPA and ETH Zurich for onward evaluation. The input Level 1b data was in radiance units, forward and nadir registered to an ellipsoid, in equally spaced 1km pixels with georeferencing information. This is the standard default so-called GBT product (Global Brightness Temperature). It consists of an array of 512 x 512 elements. The level 2 product was CTH (Cloud-Top Height) above the ellipsoid (WGS84) with an associated latitude and longitude array.

The IDL macro enables automated processing to be accomplished with user inputs for which spectral channel stereo-pairs to match as well as what parameters to use for specifying the stereo matching, particularly the search radius in row and column which is critically related to execution time and the patch size to use for matching. Owing to the slow execution time of an IDL implementation of the stereo matcher, M2, a significant effort was invested in improving this performance through recoding of the algorithm in C and porting it onto a Sun and linux platform. The IDL macro was written in such a way that other stereo matchers could be incorporated into the processing chain. This routine reads in SADIST ATSR2 data, version 2v100 or 2v300. This is NOT exactly the same as the Near Real-time ATSR format from ESRIN but would not require too much effort to add this functionality.

A search range of -2 to 2 in the x direction is used with -2 to 15 in the y direction. N.B. Along-track stereo means that the significant height changes occur in the y-direction. A typical patch radius is 11 pixels for ATSR2. Matches are performed every pixel.

The stereo matching algorithm

M2 (multi-point matcher) is an area-based stereo matcher [Muller *et al.*, 1999]. It works by designating the imagery from one camera as the reference image and the other as the comparison image. A region, the patch size (x_patch, y_patch), is chosen in the reference image and a set of comparison patches within a pre-defined search window (x_range_min, y_range_min, x_range_max, y_range_max), is established in the comparison image. The matching metric is then computed by taking all the values in each patch and subtracting the mean values within the patch from each

pixel to yield a normalised brightness. Then the absolute difference in the reference normalised patch minus the normalised values in the comparison patch averaged over the number of points being matched is tested against a threshold. The M2 metric used here is

$$SM2 = \frac{1}{N_{pts}} \left| \frac{[R(x_i, y_j) - \langle R \rangle] - [C(x_i, y_j) - \langle C \rangle]}{[R_{max} - R_{min}] [C_{max} - C_{min}]} \right| \quad \text{(equation 1)}$$

SIGMAm2

where $R(x_i, y_j)$ is the reference pixel values at (i,j)
 $C(x_i, y_j)$ is the corresponding value in the comparison image
 R_{max}, R_{min} are the maximum and minimum values within the reference image respectively
 C_{max}, C_{min} are the maximum and minimum values within comparison patch respectively
 N_{pts} is the number of points being matched
 $\langle R \rangle$ is the average value within the reference patch
 $\langle C \rangle$ is the average value within the comparison patch
 i, j are the relative indices within the patches for summation

$$SIGMAm2 = \frac{1}{N_{pts}} \left| \frac{[R(x_i, y_j) - \langle R \rangle]}{[R_{max} - R_{min}]} \right| \quad \text{(equation 2)}$$

The quantity SIGMAm2 (sigma) is an estimate of the average uncertainty in the numerator of equation. For a reference patch the x and y values of disparity (xdis, ydis) are those for which SM2 is smaller than or equal to threshold TM2. If $SM2 > TM2$ the disparity is discarded. If multiple matches from M2 satisfy the threshold criterion, the best match for a patch is defined as the one that minimises SM2. This is done by setting a secondary threshold AM2 where $AM2 = f \cdot SM2_{min}$ where f (f) is greater than 1. If the best match is the only one for which $SM2 < AM2$ it is classed as a successful match.

M3 is similar to M2 except medians rather than then means are used.
 $SM3 < TM3$ are regarded as a successful match. TM3 and TM2 maybe different.

The stereo matching schemes will fail if the areas to be matched are featureless or devoid of spatial contrasts. For ATSR2, the coarser resolution in the forward scan (out to 1.7km at the edges of scan in the forward direction) will reduce the accuracy of this pixel-level acuity matcher.

The ATSR2 camera model

For ideal stereoscopic pairs, the two images should be taken at exactly the same time. The time difference between the acquisition of the forward swath and the nadir swath is 120 seconds. Equation 3 [Prata and Turner, 1997] is used to calculate the heights, where height, H is given by

$$H = YDIS / (\tan(ANGLE_f) - \tan(ANGLE_n)) \quad \text{(equation 3)}$$

where $YDIS$ is the disparity
 $ANGLE_f$ is the forward zenith angle
 $ANGLE_n$ is the nadir zenith angle

It has been assumed that all the movement in the y direction is due to height. Also the increase in the size of the field of view from the forward view is not taken into consideration.

AirMISR Radiance-to-CTH Processing chain

ATSR and MISR data are very similar in terms of obtaining cloud heights. They both have 'cameras' at different angles which can be used to derive disparities and hence heights. There are some major differences apart from the number of cameras though.

ATSR data are co-located in the direction of travel, hence you are directly measuring the disparity difference. MISR data however and hence AirMISR data have to be remapped onto an ellipsoid projection and hence use a different co-ordinate system, so when the disparities from a matching routine are calculated they are at an angle to the direction of travel. This clearly indicates why ATSR just uses the y disparity and MISR needs both the x and y to calculate heights.

An automated IDL processing chain was written to produce CTHs from MISR level 1B2 data (all cameras registered to each other on a surface ellipsoid in Space Oblique Mercator projection). This used the M2 stereo matcher (see previous section). The JPL supplied interactive software, hdfscan, was used to extract the key metadata concerning the angles required to transform stereo matched disparity into height. In the next section, the formulae developed for this purpose are described in more detail.

Deriving heights from AirMISR data (assuming winds=0)

The following explains how the height equation was derived for MISR (AIRMISR) data.

For each camera there is a:

zenith angle - θ (wrt vertical)
azimuth angle - ϕ (wrt down-track direction)

If $\phi=0$ (i.e. the camera is looking straight down the swath as is sort of the case for ATSR) the disparity for a single camera is:

$$(h \cdot \tan(\theta) / xres)$$

where

h - height
 $xres$ - pixel resolution ($xres=1$ for ATSR)

However, if the camera is not pointing in the straight down-track direction then the measured disparity will have both a cross-track and down-track component to it where:

dx = cross-track disparity = $h \cdot \tan(\theta) \cdot \sin(\phi) / xres$
 dl = along-track disparity = $h \cdot \tan(\theta) \cdot \cos(\phi) / xres$

So if the two cameras measuring the disparity are labeled "1" and "2" and have angles (θ_1, ϕ_1) and (θ_2, ϕ_2) , the disparities of both cameras for the along and

across-track can be calculated from the "straight-down" point using the formulas above:

$dx_1 = \text{cross-track disparity for cam 1} = h \cdot \tan(\theta_1) \cdot \sin(\phi_1) / x_{res}$
 ... and so on for dx_2 , dl_1 , and dl_2 ...

The disparity that is actually measured is of (dx_2-dx_1) and (dl_2-dl_1) so:

$dx = \text{measured cross-track disparity}$
 $= dx_2 - dx_1$
 $= h \cdot [\tan(\theta_2) \cdot \sin(\phi_2) - \tan(\theta_1) \cdot \sin(\phi_1)] / x_{res}$

$dl = \text{measured along-track disparity}$
 $= dl_2 - dl_1$
 $= h \cdot [\tan(\theta_2) \cdot \cos(\phi_2) - \tan(\theta_1) \cdot \cos(\phi_1)] / x_{res}$

Hence

$\sqrt{dx \cdot dx + dl \cdot dl} = h \cdot \sqrt{[(dx_2 - dx_1) \cdot (dx_2 - dx_1) - (dl_2 - dl_1) \cdot (dl_2 - dl_1)]} / x_{res}$

Substituting the formulae for dx_1 , dx_2 , dl_1 and dl_2 into the above equation and reduce it down leads to the final formula (after employing the trigonometric identity for $\cos(\phi_2 - \phi_1)$) is:

$$h = \frac{\sqrt{dx \cdot dx + dl \cdot dl} \cdot x_{res}}{\sqrt{[\tan(\theta_2) \cdot \tan(\theta_2) + \tan(\theta_1) \cdot \tan(\theta_1) - 2 \cdot \tan(\theta_2) \cdot \tan(\theta_1) \cdot \cos(\phi_2 - \phi_1)]}}$$

DLR-IPE

DLR-IPE developed a special IDL-embedded version of its CLT-matcher for CLOUDMAP.

The matcher accepts large data formats and navigation parameters to be read from data files (instead of setting them manually). Matching can be confined to a pre-defined displacement vector with a selectable range of deviations. This ability allows for a systematic "slicing" through all height levels of cloud fields.

The confinement of the displacement vector is important for stereo-matching of semi-transparent clouds and for matching of clouds with cloud shadows.

No results were available at the time of writing.

ETH

Cloud-Top height from MOMS scenes

Two stereo images of Bavaria (data take number: 083C, scene number: 27-30) were used as test set. The images were acquired on March 14, 1997 from the MOMS sensor, with a ground resolution of 18 m and a time delay of 40 sec between the forward and backward channels. They were supported by 58 Ground Control Points (GCPs) marked on a digitized topographic map at scale 1:25,000. The GCPs were measured with a precision of about 5 metres in planimetry and 2 metres in height. The images were first preprocessed (noise reduction), then the Wallis filter was applied (contrast enhancement, radiometric equalization). The GCPs were identified

in the two images by least square matching and a bundle adjustment based on the

- 6, 10 and 18 GCPs, chosen along the borders in order to achieve an optimal distribution;
- linear and quadratic function to model the change of attitude in the flight direction;
- use of Intersection Points (IP).

model of V. Kratky (1989) was used with different input parameters:

The best results were obtained using 10 GCPs and a quadratic attitude model. In this case there was no convenience in using IP, but they can be very useful when GCPs are not in a sufficient number or not optimally distributed.

The same operations were applied to another stereo pair from the same set (data take number: 083C, scene numbers: 25-26), showing clouds. 29 GCPs were measured in 1:50,000 digital topographic maps and in the two images, whereby point transfer from one image to the other was by least squares matching (Figure 25). The bundle adjustment based on the model of V. Kratky was applied with 10 GCPs and a quadratic attitude model. The RMS error of 19 Check Points (CPs) were 5.2 m in X, 4.4 m in Y and 11.1 m in Z. Figure 26 and Figure 27 show the errors in planimetry and in height for each CP. The strict sensor model was then approximated by polynomial mapping functions, which are almost as accurate but much faster. Before matching, a further preprocessing to detect and reduce vertical stripes due to the saturation of the even image columns in cloud regions was necessary (Figure 28).

The next step is to develop an algorithm for matching in order to take into account the low texture of the clouds, the discontinuous and sometimes transparent or semi-transparent cloud form and the cloud deformation during the time interval between the acquisition of the images (see also 3.3.5.2). These problems can be reduced by using least squares matching with geometric constraints, i.e. searching the corresponding points along the quasi-epipolar lines defined by the mapping polynomials above mentioned. The results of matching will be controlled by manual stereo observations at digital photogrammetric stations.

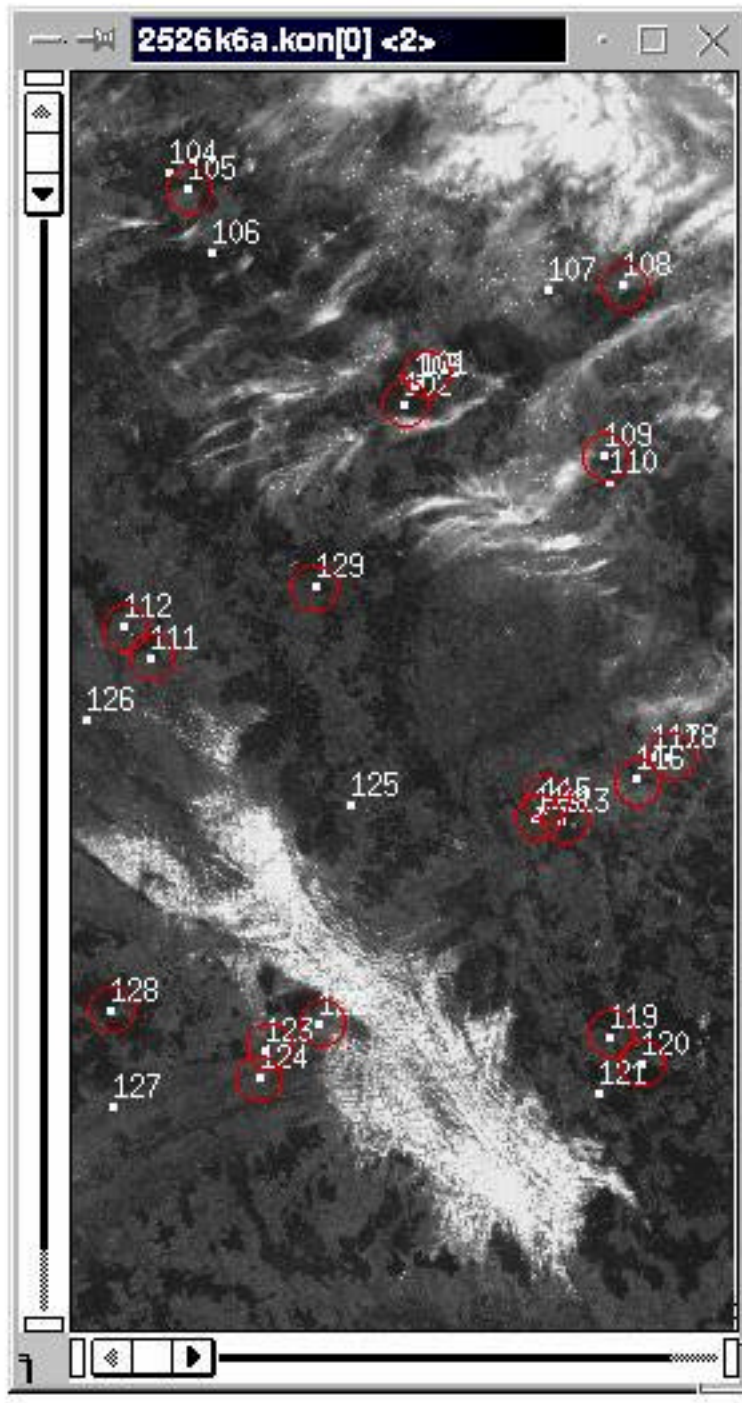


Figure 25: Distribution of GCPs and CPs (in red)..

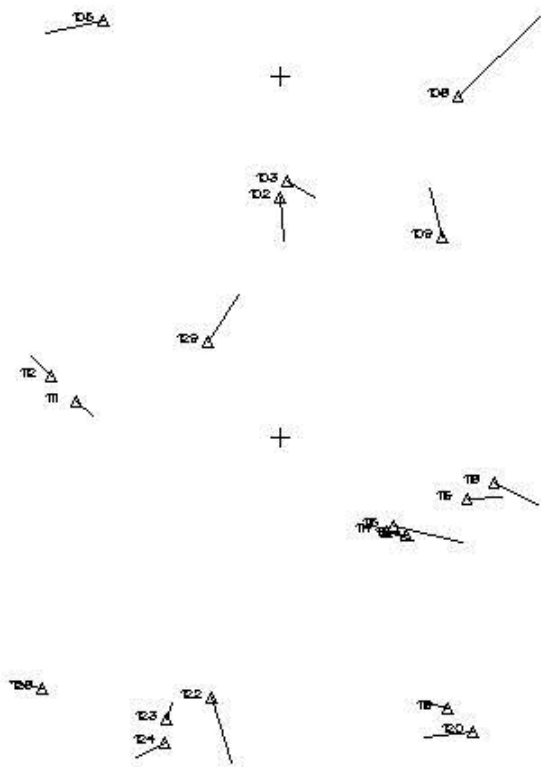


Figure 26: Plot of errors in planimetry for 19 check points.

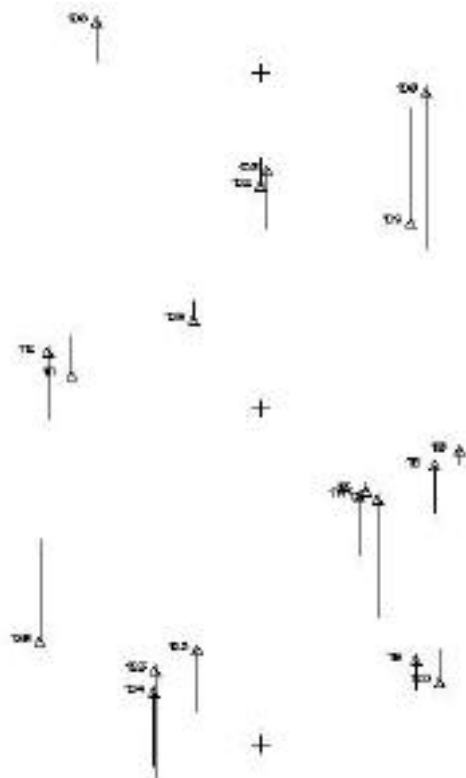


Figure 27: Plot of errors in height for 19 check points.

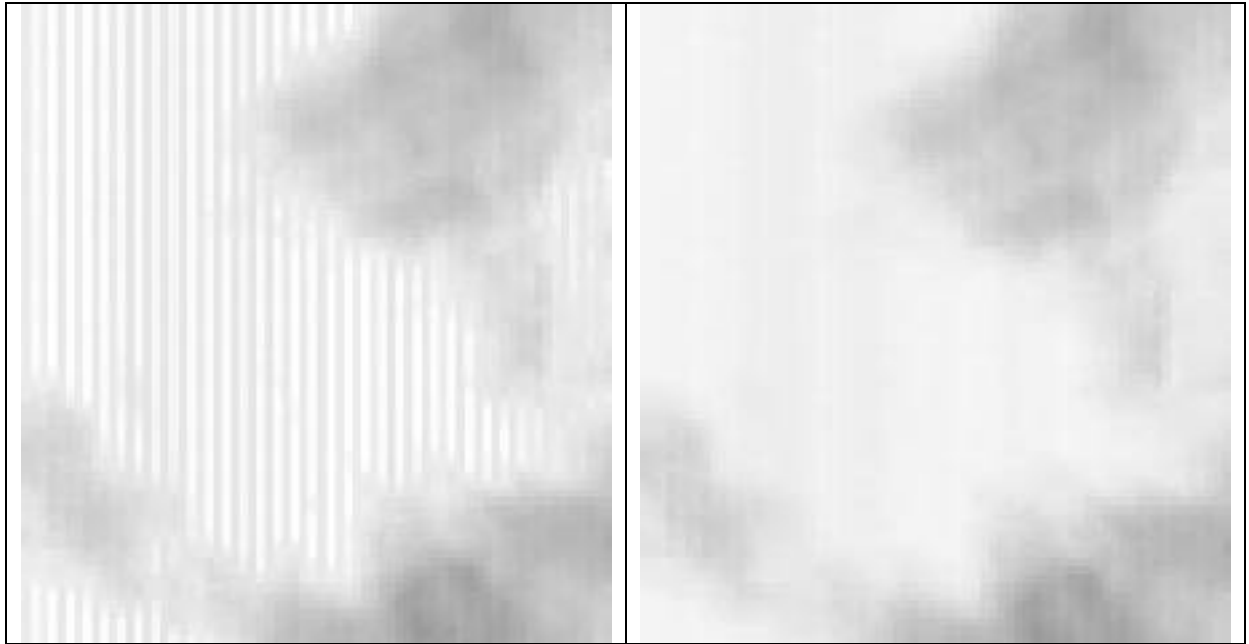


Figure 28: Zooms of saturated areas before (left image) and after (right image) applying the filter.

Stereo matching algorithm

Matching of clouds presents various problems: low texture or saturation at clouds, small SNR, poor definition of cloud edges, discontinuous, transparent or semi-transparent surfaces, large illumination differences, perspective differences and occlusions, multiple solutions etc. Such problems were reduced in previous research by using a Least Squares Matching procedure which made use of geometric constraints (epipolar line) to reduce the search space for corresponding points from 2D to 1D. This matching procedure is however sensitive to local shape and texture variations, which often occur with clouds.

Thus, first a matching of larger mostly stable regions will serve to guide and restrict the more accurate but also more susceptible to noise, fine matching. In addition, a dynamic analysis of the cloud-base reconstruction from subsequent stereo-pairs will be used for verification of the matching results as well as restriction of the search space.

Camera modelling for ground-based images

The inner orientation parameters are measured before and after the field measurements with a dense 1.5mx2mx2m testfield at our institute (Figure 29). These calibration procedure has already been used for 18mm lenses of different cameras (eg KODAK DCS460, KODAK DCS200) (Beyer, 1992), but will have to be adapted for the calibration of the fish-eye lens.

There are two independent methods used to determine the exterior orientation: first, an airplane with DGPS flying a flight path at different altitudes and imaged by the ground cameras will serve as a dynamic control point field. These known sky points can thus be used for calculating the exterior orientation elements.

The second approach works with clear sky night images where the stars can be taken as sky control points instead of the airplane. In addition, GPS measurements of the camera locations, electronic levelling and azimuth sensors will provide at least approximations for the exterior sensor orientation, or even an additional control of the orientation as determined by the two above mentioned methods.

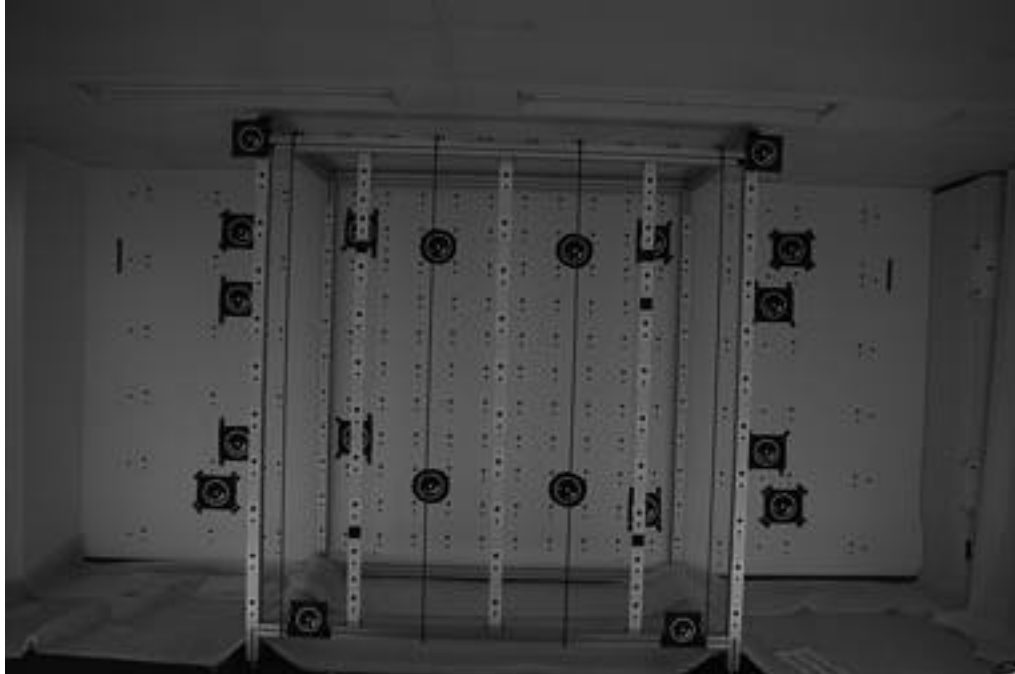


Figure 29: Testfield at ETH for determination of the inner orientation parameters of the cameras.

DLR-IPA

AVHRR Contrail detection algorithm implementation

For the standard processing of AVHRR-HRPT data of NOAA14 the contrail algorithm is frozen to the current version described by Mannstein et al. (1999). The scheme was successfully added to an operational processing chain including a quality control.

AVHRR Contrail processing over Europe

The contrail detection algorithm meanwhile was applied to 2208 daytime NOAA-AVHRR scenes covering Europe from the years 1994-1999 (see **Figure 22**).

Due to higher throughput - the network within DLR-IPA was rebuilt in the summer of 1999 - we may now process even more data. Therefore we expanded the envisaged processing to include the night time overpasses (2191 possible nights covering the years 1994 - 1999), which doubles the amount of AVHRR data to be processed within CLOUDMAP. This decision is based on scientific reasoning: contrails have their dominant climatological impact at night. Processing of night time data started in August 1999. All archived night-time data will be processed until next summer. Online processing continues on night + daytime data.

AVHRR Contrail processing over Asia

A data conversion routine to the DLR HRPT format was developed. Thus those scenes may be handled identically like the ones received in Oberpfaffenhofen. We already applied the contrail detection algorithm to 95 of the approximately 400 overpasses of this set. First results are shown in Figure 30.

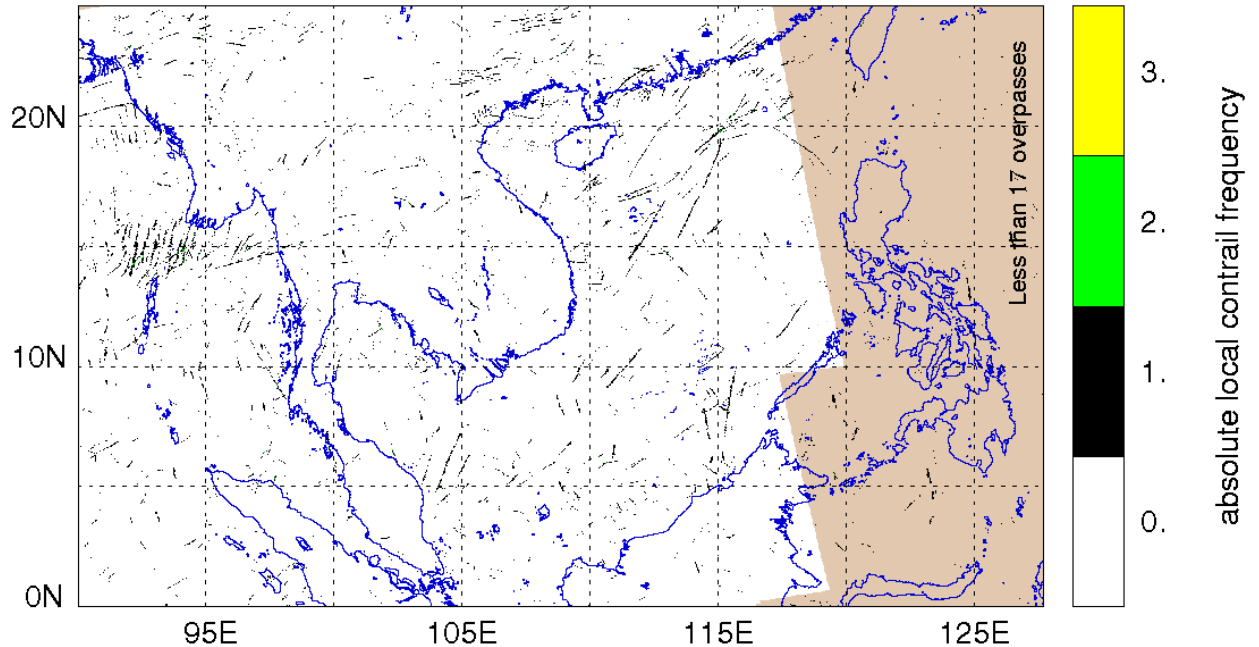


Figure 30. Stacked Contrails over SE-Asia from 60 scenes in January 1998

Implementation of ATSR2 Contrail detection

The parameter set of the current version of the algorithm was also applied successfully to ATSR2 test data. The algorithm gives reasonable results both for nadir and forward scan. **Figure 31** shows a ATSR2 12 μm channel image and **Figure 32** the corresponding derived contrail mask.

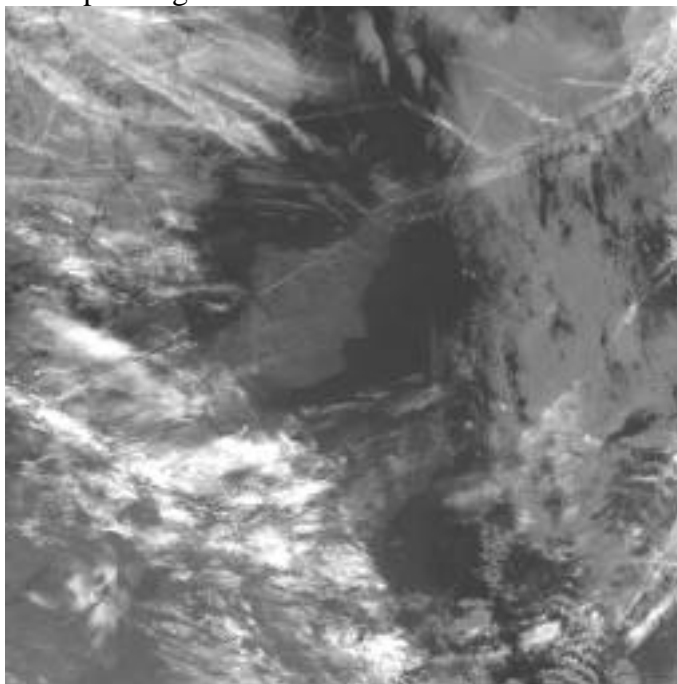


Figure 31. ATSR2 test dataset with contrails (12 μm channel)



Figure 32. Detected contrails from the nadir view of the test dataset.

For the characterisation of the performance of the algorithm it is necessary to produce longer series of data. We expect from the processing of ATSR NRT data to be able to give a good estimate for the false alarm rate. The detection efficiency has to be determined by comparison with other datasets. The combination of the contrail detection algorithm with the stereo height determination from UCL was not successful. The tested area-based stereo matchers did recognise and resolve only a small fraction of the contrails. This is shown in Figure 33. A suitable feature based matcher is not yet available for testing.

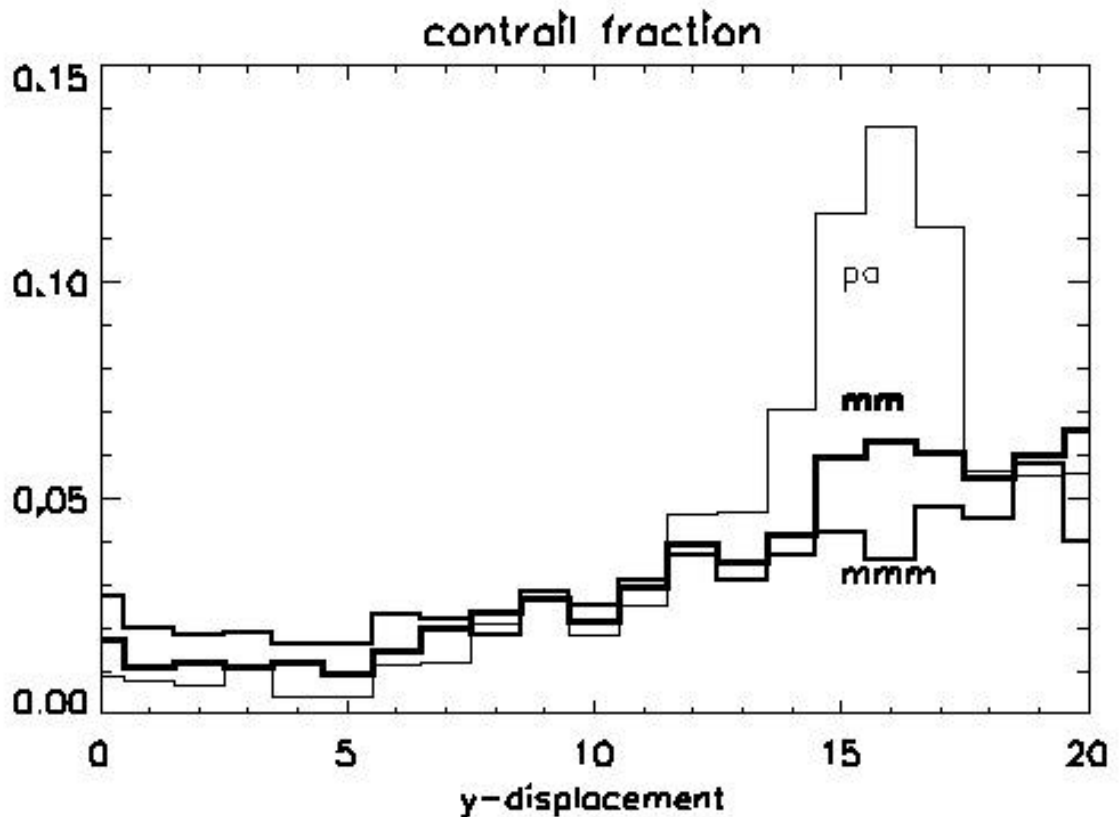


Figure 33. Fraction of contrail pixels within the y-displacement classes of different area based matchers: mm and mmm are the UCL matchers, pa is a matcher programmed at DLR-IPA and tuned to handle contrails. All matcher either ignore contrails or overestimate their width.

DLR-IST: Decision Directed Estimation of Cirrus and Contrails Based on Property representation by Fuzzy Measures and their Fusion by a Fuzzy Integral

Introduction

The goal of this workpackage was a theoretical investigation of the detection of cirrus clouds and contrails based on their stochastic properties coupled with other properties. Such properties include the change in brightness of surrounding structures and known properties such as the linearity for contrails. The methods are of more general relevance and based on grey scale images of different kinds. If multispectral images exist, relevant information is obtained by pre-processing. With this an enhancement of the searched structures as contrails is achieved. If the structures of interest are superposed by similar stochastic structures, the separation is nearly impossible. If the information in many related images (multispectral images) is mapped in their grey features, images of different origin can be used, such as MOS, AVHRR and ATSR2.

Contrail Detection

The separation of contrails and cirrus clouds is based on their structure (“texture”). The mathematical basis and algorithms are similar but the properties are of different kind and they will be considered separately. If multi-spectral images exist the images will be combined for an enhancement of contrails.

Difficulties with contrail separation

Contrails are superimposed on structures such as clouds and the Earth's surface. They can be interrupted, thinned or broadened. The contrails can be brighter or darker than the surrounding clouds, so that the separation cannot be achieved solely through their grey scale value. Other edge structures are also present such as coastlines, clouds and rivers and are difficult to distinguish when thin clouds are superposed. If the contrails are optically thin they are difficult to detect. The structures of the boundary of clouds, coastlines, and rivers are difficult to distinguish from contrails especially if they are approximately linear. The contrails are visible in different grey value ranges and normally cannot be detected only in one range.

Estimation of relevant textural properties

For the detection of contrails a lot of images were studied to isolate relevant statistical properties for the contrails. Some obvious properties could be observed in the images such as contrails have mostly a linear structure, contrails are mostly brighter than surrounding regions and lines of contrails are often interrupted. Some relevant textural properties can also be isolated. It is found that contrails have a special texture of grey values, which are conditioned by their physical structure. The boundaries of the contrails are fuzzy. The structures along and across the contrails are different. The brightness of the contrails is reduced with the distance from their centre. Diffusion processes can describe the ageing of contrails. The centre of gravity of contrails can describe the line of the contrails. The contrails can be shifted and distorted by wind. The structures of contrails can change with distance from their centre.

Pre-processing for contrail detection

In the case of AVHRR, MOS or ATSR2 images there exist two or more images for contrail detection. They are taken in different frequency ranges. For the enhancement of contrails two images are related together to the range of the grey values and by multiplication of one image. This is based on the results obtained by analysis of the histograms within selected ranges. The properties of the histogram will be analysed successively until the best parameters are estimated.

Development of mathematical basis for description of textures

The main mathematical basis is the separation by stochastic properties. This is based on the representation of the stochastic in form of the dynamic of the stochastic. The mathematical fundamental is developed in general. These theoretical results are used in their fundamental meaning for an algorithm, which uses only important points and not all details to be fast. The mathematical fundamentals are based on three steps:

- Mathematical description of textural properties by a system of stochastic differential equations, rank or sign-functions and calculation of estimated values and their stochastic part
- Generalised description of different kinds of properties by mapping on the closed interval $[0,1]$ represented by the Fuzzy measure
- Fusion of different parts of the properties by a combination of different kinds of properties by the fuzzy integral

The fuzzy integral has the properties of a fuzzy measure and is used as a new fuzzy measure. Based on this property a hierarchical algorithm is developed to extract all interesting stochastic information.

If the interactions between the neighbouring pixel values are already known, a description by a system of stochastic differential equation is applied. The stochastic components y_1, y_2, \dots, y_n describe the stochastic effects acting on the neighbouring pixels at the selected pixel point x . Dependent on the local situation the distance of interaction is more or less large and give a defined contribution to the mean value of the grey values. The stochastic components are combined together by a coupled system of stochastic differential equations with a coloured noise n . All of this is related to different pixel-points x . In such a way we have a system of vector equations of the form

$$\begin{aligned} dy_1(x) &= \mathbf{F}_1(y_1, y_2, \dots, y_n) dx + G_1 n(x) \\ dy_2(x) &= \mathbf{F}_2(y_1, y_2, \dots, y_n) dx + G_2 n(x) \\ &\dots \\ dy_m(x) &= \mathbf{F}_m(y_1, y_2, \dots, y_n) dx + G_m n(x) \end{aligned}$$

Only simple categories of functions, characterising the interaction between pixels or regions, are used for the non-linear functions. If the interaction can be assumed to act over a long distance then such functions as logarithm or square root are used. The short acting interaction will be described by functions such as exponential function or power functions with higher coefficients.

An approximate solution of this equation is the Martingale technique or a simpler hierarchical filter function is developed and gives estimation values y_{est} . The subtraction from the original value is used to obtain the stochastic value y_{stoch} .

If not known a priori relationships between the components in form of equations then non-parametric methods are applied. Examples have shown that the rank is an effective method to eliminate stochastic properties. The rank $R_{i,j}$ for images with the grey values $x_{i,j}$ of the pixel point (i,j) is described with the help of the step function $u(x)$ with summation over k and l by

$$R_{i,j} (N,M) = \sum_{k,l} u(x_{i,j} - x_{l,k}),$$

where $k = \{i-M, \dots, i-1, i+1, \dots, i+M\}$ and $l = \{j-N, \dots, j-1, j+1, \dots, j+N\}$.

The rank $R_{i,j}$ shows how many of the pixels in the region $2N*2M$ have a value less than the selected value $x_{i,j}$ in this region. This value characterises independent of any a priori knowledge the stochastic relationships and is used to describe the stochastic in different regions.

If the image seems to be only noisy the calculation of the distribution of signs is used. The number of the neighbouring values larger than $x_{i,j}$ with a threshold g is given by

$$S_{i,j} (g,M,N) = \sum_{k,l} u(|x_{i,j} - g| - |x_{l,k} - g|) u(x_{i,j} - x_{k,l})$$

Only those values which validate $x_{i,j} > g$ are collected. Because the relationship

$$2*u(x) = \text{sign}(x) + 1 \text{ and } u(x_{i,j} + x_{k,l} - 2*g) = 2$$

is fulfilled if and only if

$$|x_{i,j} - g| > |x_{k,l} - g| \text{ and } x_{i,j} > x_{k,l} \text{ or}$$

$$|x_{k,l} - g| > |x_{i,j} - g| \text{ and } x_{i,j} < x_{k,l}$$

so that the faster relationship

$$S_{i,j}(g, M, N) = u(x_{i,j} + x_{k,l} - 2 * g)$$

is used. With the help of these stochastic procedures different stochastic properties are obtained where only selected parts are relevant for the detection on contrails.

Based on the sign representation four types of stochastic can be separated

- $S(g)$ is calculated for different values of g
- The difference for different levels of g are calculated, i. e. $S(g_m) - S(g_n)$
- Repeated calculation of S by using $S_{i,j}(g, M, N)$ as new values of the grey value of the pixel (i, j)
- Usage of the variance of $S(g)$ as the stochastic value

Analogue combinations of differences and hierarchical structures can be constructed with the rank function $R_{i,j}$ such as the difference, different values of g for the threshold, $R_{i,j}$ as values for the pixel (i, j) and used equivalently to grey values and using the variance as a new value.

The mathematical method is only the first step, the second and more important field is the model construction and the understanding and representation of different effects and their superposition. The components are to decompose and this is normally an iterative process. It is developed a decision directed method. For this is organised a mapping of stochastic properties in a fuzzy measure and a related fuzzy function. This fuzzy functions and fuzzy measures are combined by fuzzy integrals. The a priori knowledge is obtained by the analysis of many different kinds of images.

Mapping of properties of textures on fuzzy measures and fuzzy function

The terminus texture, used for properties in the image, is translated to stochastic properties if mathematical description is applied. For selection and combination of relevant stochastic and also non-stochastic properties the representation by fuzzy measures and related fuzzy functions is used. By the fuzzy measure or the fuzzy function, respectively, it is possible to combine different kinds of properties to describe a selected texture more precisely (Hetzheim, 1993a,b). This is achieved by the mapping of different kinds of relationships on the closed interval $[0,1]$. On the other side, the fuzzy function gives the possibility to use the measure related to their importance. For such a mathematical property the loss of the additivity is a condition. The loss of additivity is compensated by a coupling parameter α . The Fuzzy measure e is used in the definition of Sugeno. For the two elementary properties z_1 and z_2 the combination is given by

$$e(z_1 \cup z_2) = e(z_1) + e(z_2) + \alpha e(z_1) e(z_2)$$

where $\alpha = (1 + e(z_1)) * (1 + e(z_2)) - 1$

The general fuzzy measure A is obtained by collection of many elementary Fuzzy function in the form:

$$e(A) = e(z_i) + \alpha e(z_i) e(z_j) + \dots + \alpha^{n-1} e(z_1) \dots e(z_n)$$

The coupling parameter is obtained by iterative solution of the equation

$$f_{\tau} \mathcal{N} (= \int_{\tau} \mu(\delta) \times \mathcal{P}_{\tau}$$

In the following step the next region of another property of the contrail is combined with this fuzzy function f_{τ} . In such a way we obtain a set of fuzzy function, f_1, f_2, \dots, f_{10} and fuzzy measures, $\mu_1, \mu_2, \dots, \mu_{10}$. Here the elements of the sets are obtained directly by a priori assumed properties or by derived properties obtained as the result of a fuzzy integral. In such a way we construct a hierarchical process for all possible combinations of parts of properties. The summation of all combinations of fuzzy measures with fuzzy function makes us sure, that all possible properties in all combination that should be considered are used. In such a way we get an image mapping the properties of a contrail, where the (grey) values represent a measure for the membership related to the existence of a contrail. This is a normal number, not a fuzzy number. With the help of a threshold it was decided, which pixel of the image belongs to a contrail. By this procedure different kinds of stochastic are separated automatically from images.

The structure and texture of the contrail is influenced by the wind. This fact complicated the detection of contrails because many different structures exist in dependence of the action of wind and the age of the contrail. On the other side changes in the contrails with the time is used to estimate the age of the contrail to find aged contrails. For such a separation is assumed that the effect of the diffusion can be described by the diffusion equation. This possibility is demonstrated on an MOS image with an aged contrail.

Algorithms for detection of contrails and their present realisation

For the detection of contrails the mathematical fundamentals are reduced to obtain fast working algorithms. Vector processes working on the entire image replace especially the serial working routines because IDL is the basis language and works much faster on vector image processing. These are functions for the entire image. In the first step the contrails are enhanced for finding the regions where the contrails are expected. If multispectral images exist the images are adapted together by a calibration. Such a calibration has to be done over some limited ranges and for this ranges combinations of both images are produced.

In this way is obtained a kind of membership functions for the contrails. For this the stochastic is estimated in different directions, because the contrails have a special property in the line direction. After this the hierarchical optimal detection of properties for the contrails begins. The hierarchically working algorithm is controlled by parameters. Finally a logical or arithmetical combination of binary images is produced. A threshold is then used to decide where the contrail is separated. The algorithms are written in IDL language. If it is possible inserted functions of IDL are used for less time consuming of algorithms. Most parameters are estimated automatically by analysing the image.

The algorithm is applied to single and multispectral images. For the detection of contrails the programmes were tested in different kinds of images e. g. different regions over the earth, different cloud coverage and different sun angles. Over 40 images were tested for contrails. Most contrails were detected but also some other boundaries were falsely interpreted as contrails. Often coastlines, rivers and cloud-edges are not distinguished from contrails.

The algorithm was applied to MOS-images, AVHRR-images and ATSR2-images, also for images taken behind the polar circle from an aircraft and for images from ground. The results were as follows:

The contrails are detected but it is not clear how many contrails in reality exist, because not all are clearly visible.

For multispectral images an automatic adaptation is developed for the conditions of the images taken at different frequencies, e. g., the images are calibrated in such a manner that the local shapes over every elected range is most likely. An important problem is also the realisation by a programme, especially that it is robust and fast enough. Many algorithms cannot be realised in their original mathematical form, because they were too time consuming and too big or the programme was only relevant to a special case.

Detection of Cirrus clouds

The separation of cirrus clouds is based on the same principles as the separation of contrails only other kinds of properties are important. The main properties of cirrus clouds are that the cirrus clouds are very thin, hardly visible over clouds, they have nearly not visible boundaries and they have different textural structures. Their generation and their physical properties are the reason for their special stochastic properties.

Very important is the physical understanding of the generation process of cirrus clouds to find out the important properties and their influence on the grey values of the image. For the frequency of multispectral images is important that they are high and very cold, mostly ice crystals. The extension of cirrus clouds is mostly like normal clouds without an extension in a special direction.

Because the methods are similar as such for the contrails, they are not explicit explained here.

The algorithms for the detection of cirrus clouds is based on the

- Enhancement of different textures by multiplication with different values
- Estimation of a threshold for characterisation of the boundary of a cirrus cloud
- Addition of different texture properties for separation of regions with distinguishable structures
- Detection of other clouds by their structure and masking of this region
- Estimation of structures by non-parametric description of structures

The properties of cirrus clouds are essentially based on their stochastic. It cannot be assumed an effect in different directions. The stochastic in all directions have an equilibrium distribution. The main task is to find the boundaries for changing the stochastic beginning from the core of the cirrus cloud. If such an onion structure of the stochastic is detected, then an important property for the existence of cirrus is given.

An iterative process produces different shells of the cirrus clouds. The isolation of cirrus clouds is achieved by using a threshold for finding the boundary. The fuzzy measures are used as given above. For the description by fuzzy measures and fuzzy function are the following properties selected:

- Difference of stochastic values limited by a threshold (related to an assumed boundary)
- Change of values is limited in regions
- Wavelet transforms with limitation of parameters

- Gradient of neighbouring values ordered by rank
- Combining of bitmaps obtained for different limits in the grey values
- Ordering of histogram values for small areas

Cirrus clouds covered by other clouds could not be detected. The texture properties are also used for masking of regions, where structured clouds occur such as a vortex of clouds.

Algorithms for detection of cirrus clouds and their present realisation

Only three images with cirrus were used for analysis because no more images with isolated cirrus clouds were available. The cirrus clouds were detected and also the boundary with a calculation of the numbers for the stochastic properties especially the boundary effects.

In one example a cirrus cloud is detected, which is alone. In another case a second cirrus cloud overlays a cirrus cloud. In this case both cirrus clouds could be distinguished by their different stochastic structure, especially an overlaid superimposition of directed effects in the stochastic.

Open issues and future work

Open issues are the optimisation of programmes related to more properties to distinguish contrails from other lines if it is possible. An open issue is also the isolation of cirrus clouds superposed over other clouds by multispectral images. The optimisation of programmes related to more properties to distinguish contrails from other lines, if it is possible, is a task for the future.

A better time efficiency for programmes (reducing time consuming) is the aim for the near future. In future programmes have to be tested on more examples. It is also important to look for a better time efficiency of programmes by reducing their time consuming. The automatic adaptation related to conditions of the image, which have to be estimated automatically, is also a task for the future. The parameter-controlled calibration of images may also be investigated for a precise but robust solution. For a better understanding more examples have to be investigated. The comparisons with the result of the algorithm of IPA have also to be performed.

Example results (no commentary supplied)

Examples of cirrus clouds in MOS images



Figure 34. Cirrus clouds (original MOMS image) where boundaries difficult to see

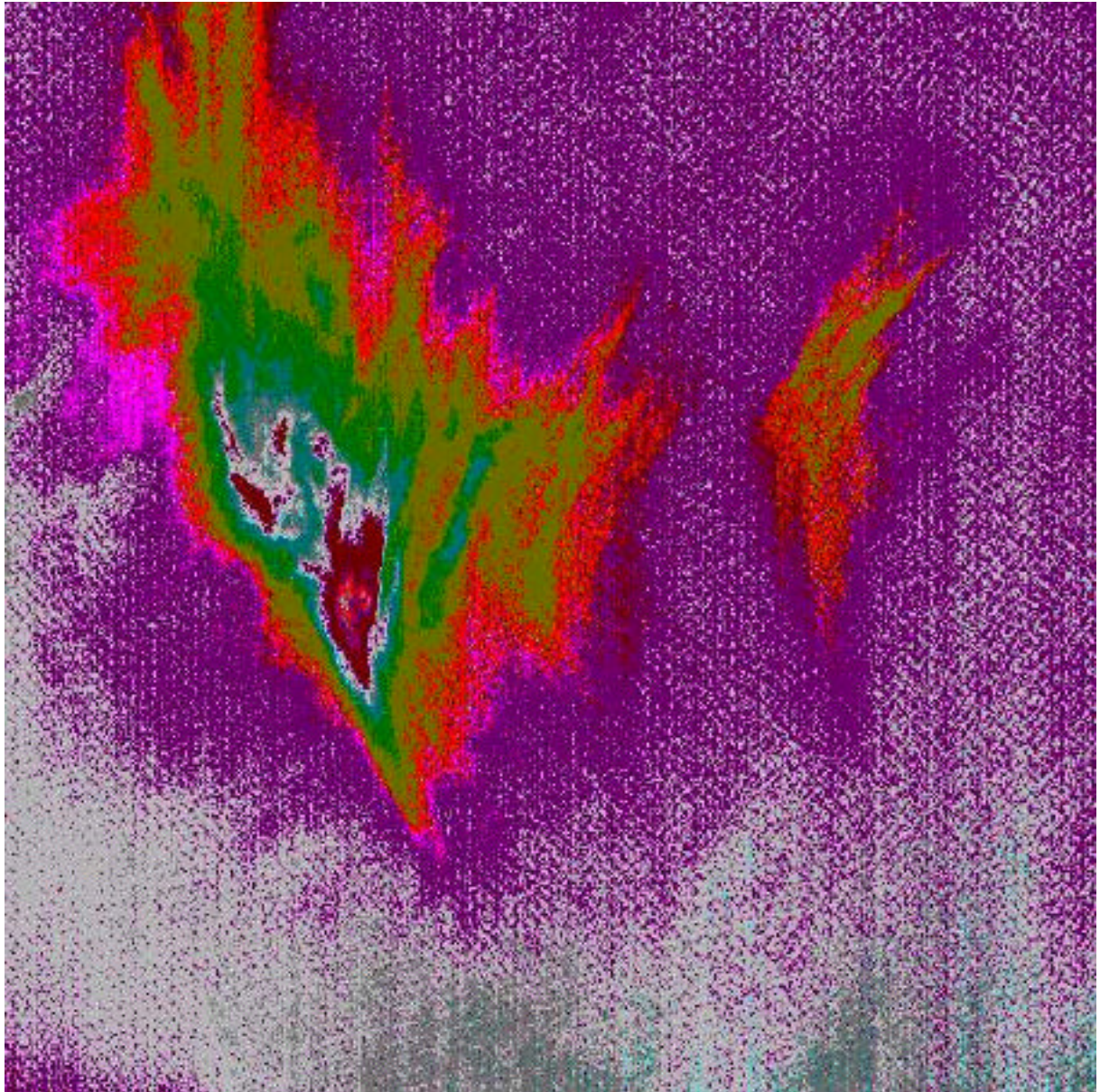


Figure 35. Detection of a cirrus cloud from MOMS with extracted boundary and core

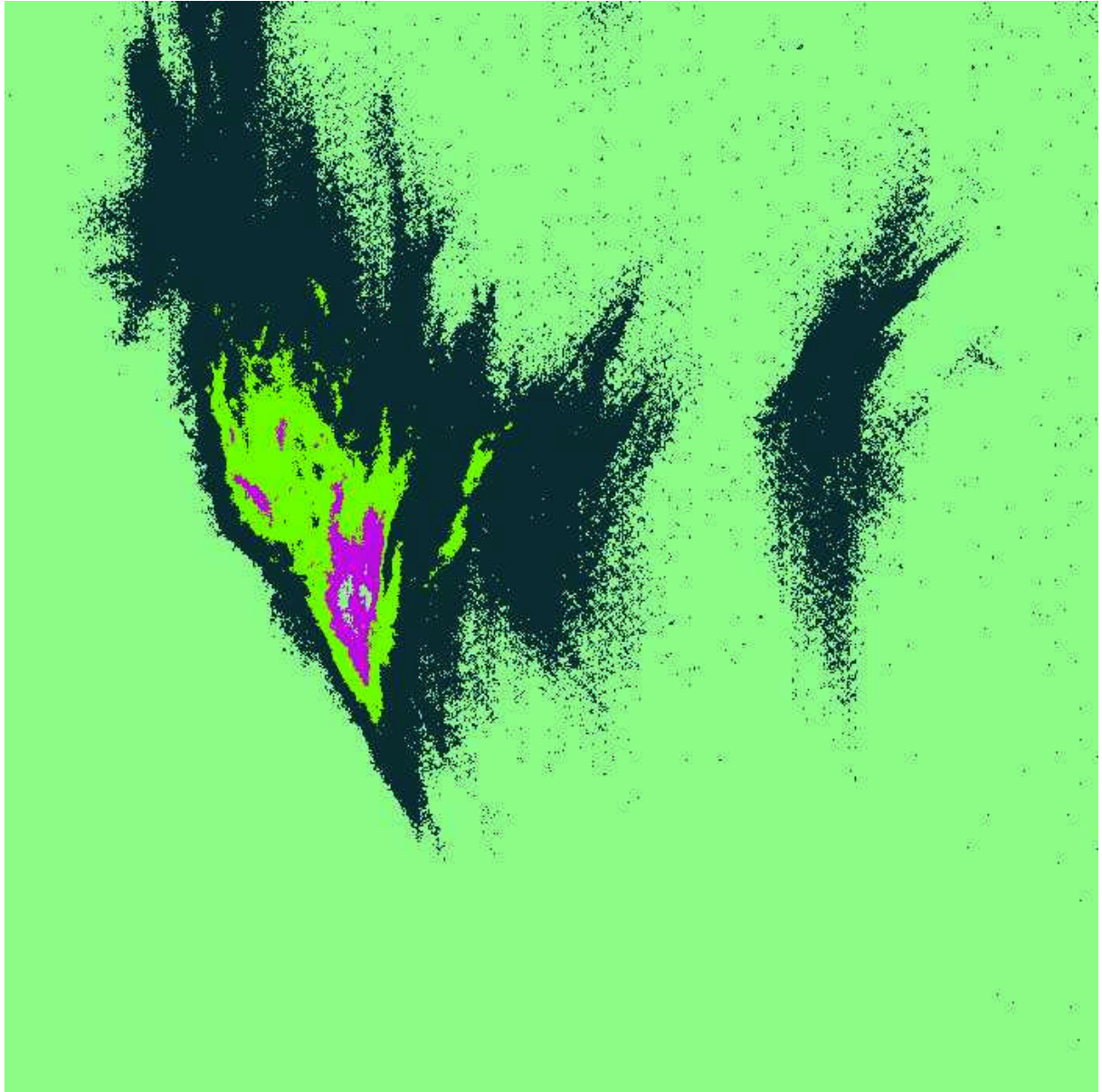


Figure 36. Representation of the boundary structure of the cirrus cloud from MOMS

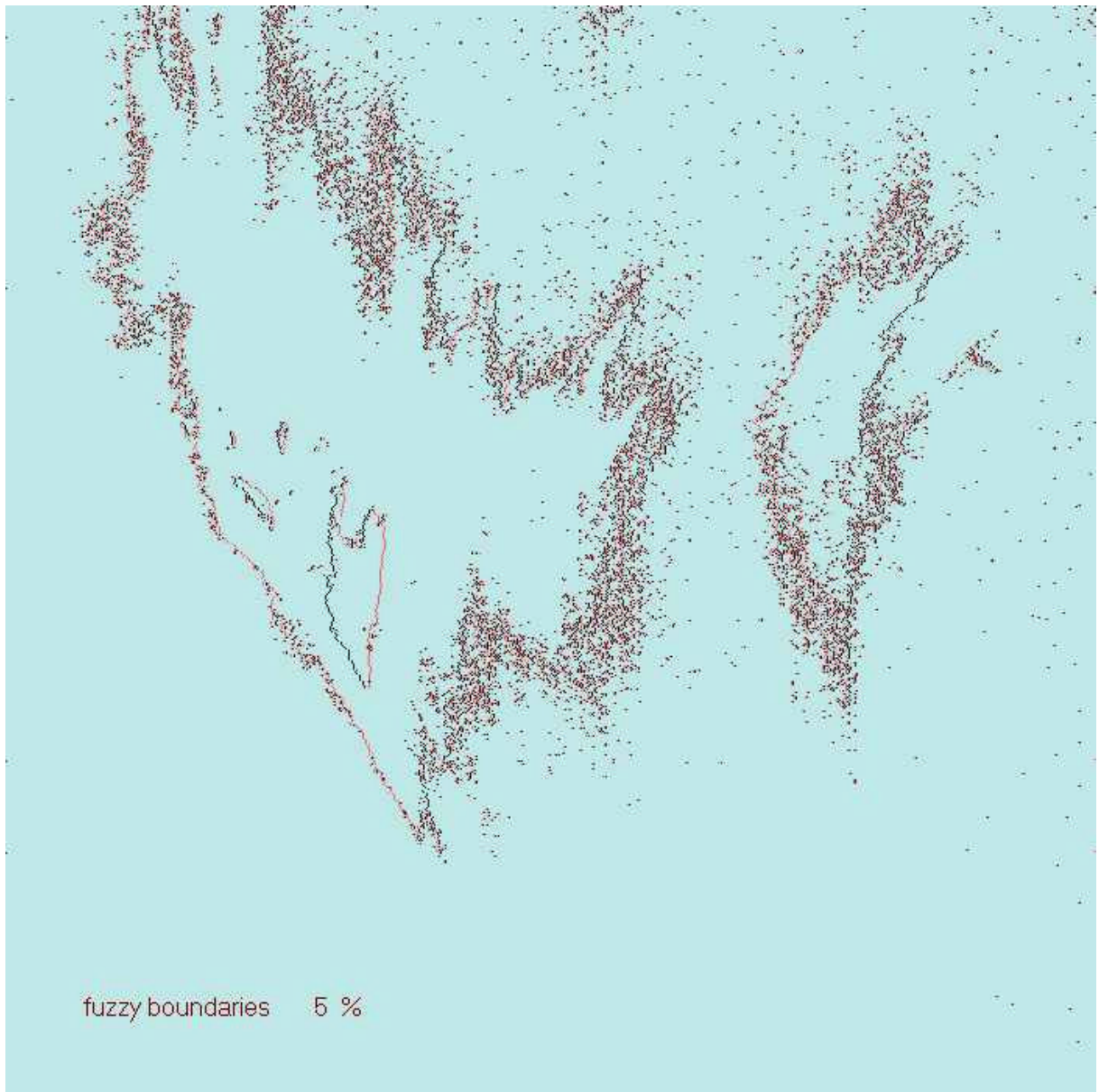


Figure 37. Representation and quantification of the boundary of the cirrus cloud from MOMS



Figure 38. Two different layers of cirrus clouds (original MOMS image)

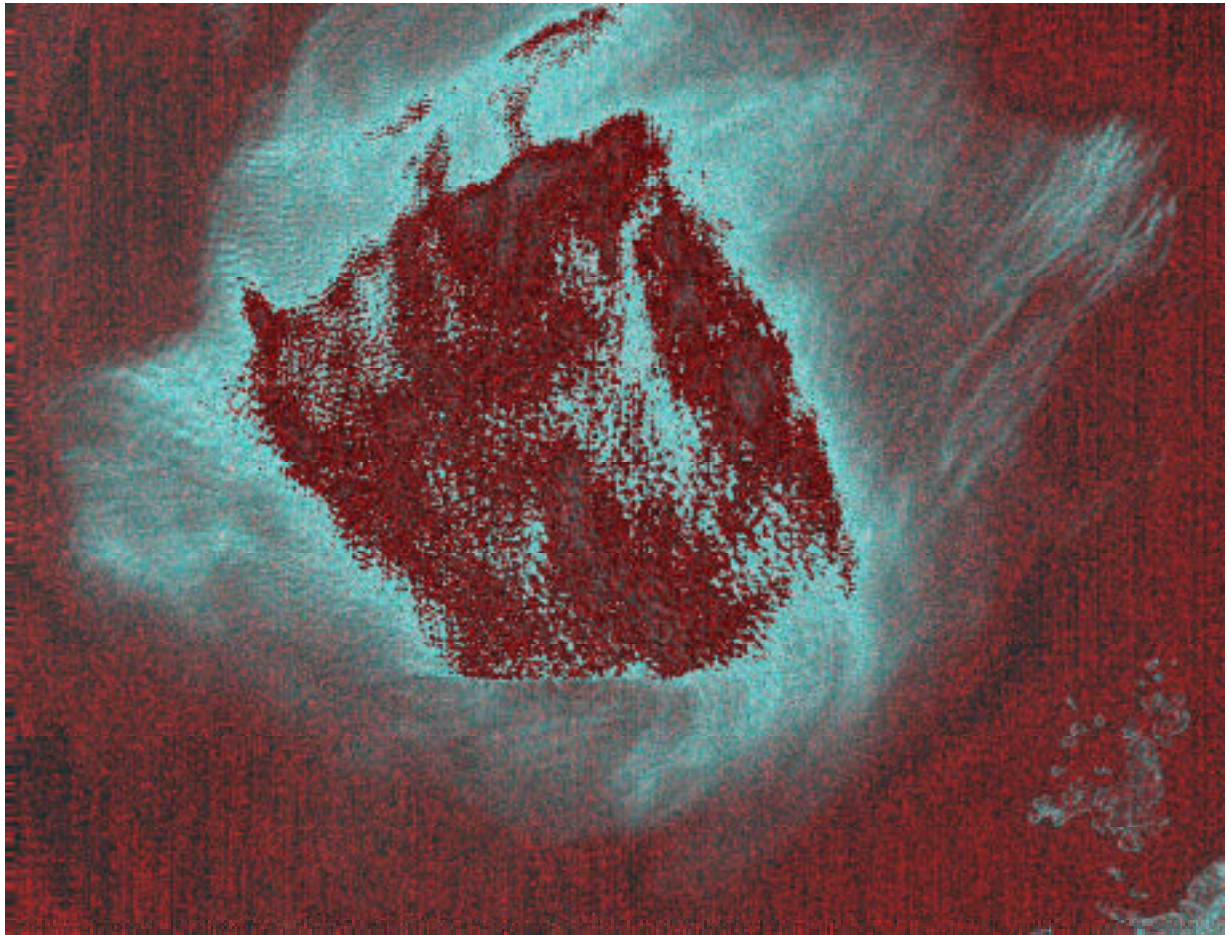


Figure 39. Representation of the lower cirrus cloud (blue) from MOMS

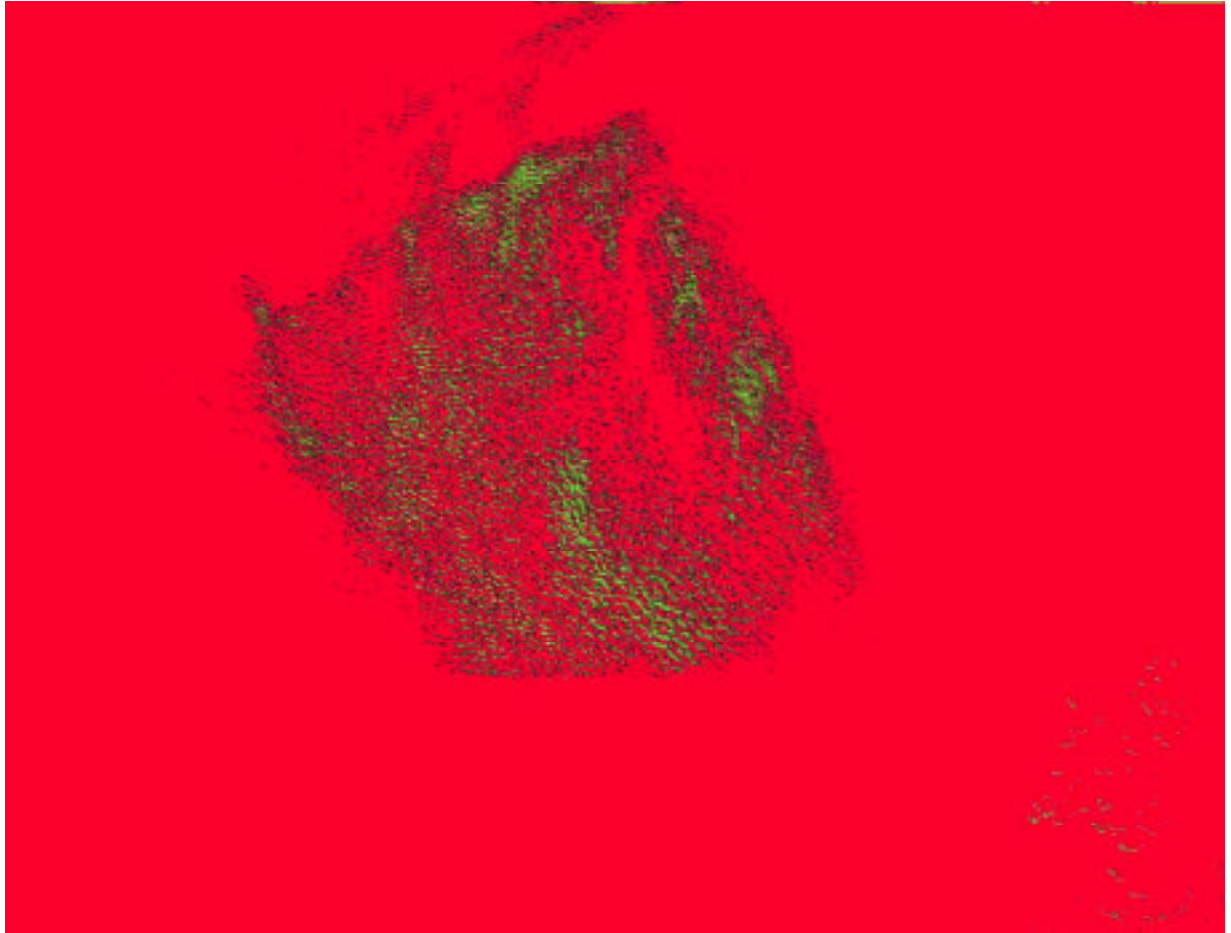


Figure 40. Separation of the upper cirrus cloud (yellow) from MOMS

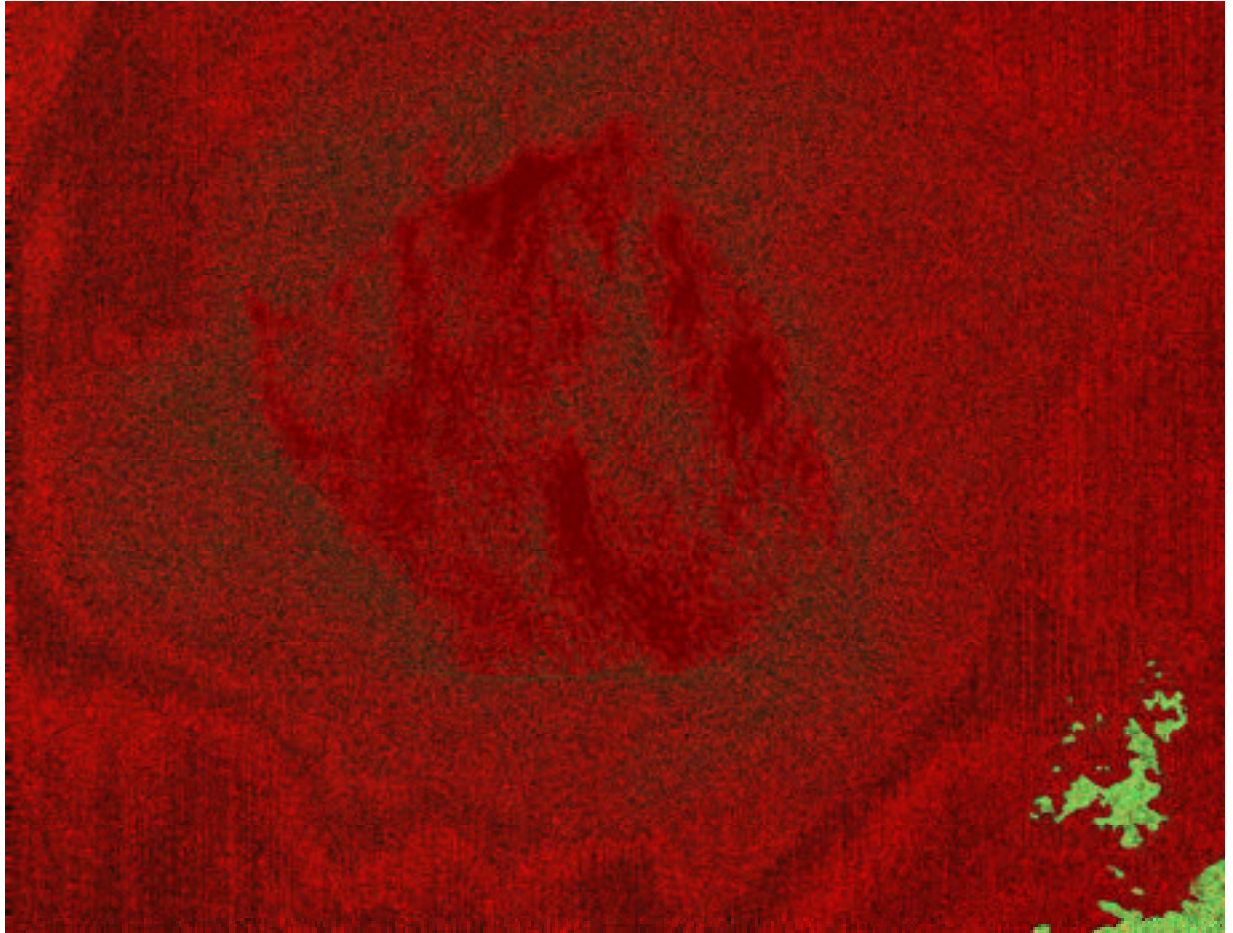


Figure 41. Isolation of no cirrus clouds (green) from MOMS

Examples of contrail isolation in AVHRR images

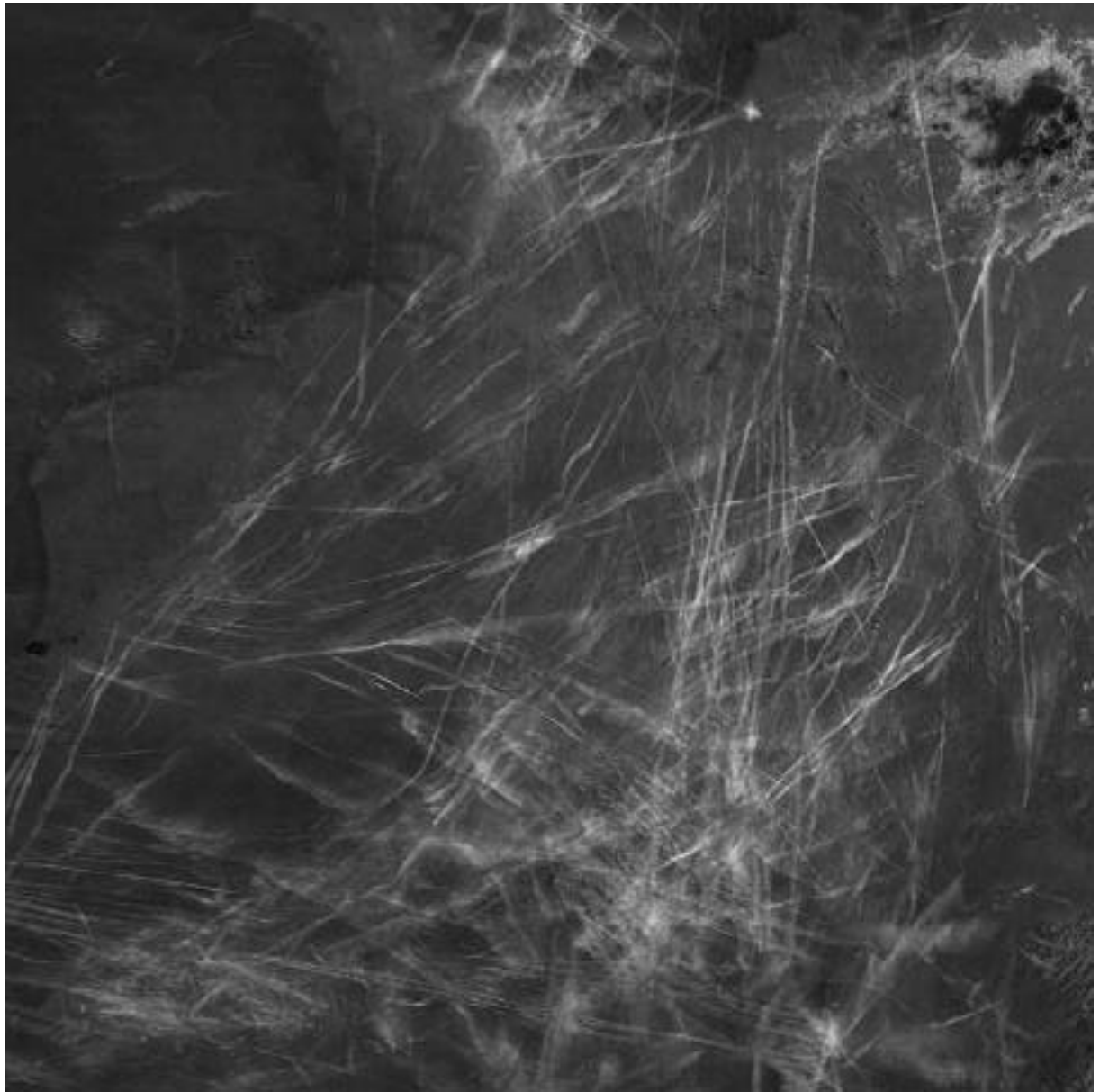


Figure 42. Germany with many contrails (original AVHRR image)



Figure 43. Isolation of contrails (more flights red) from AVHRR

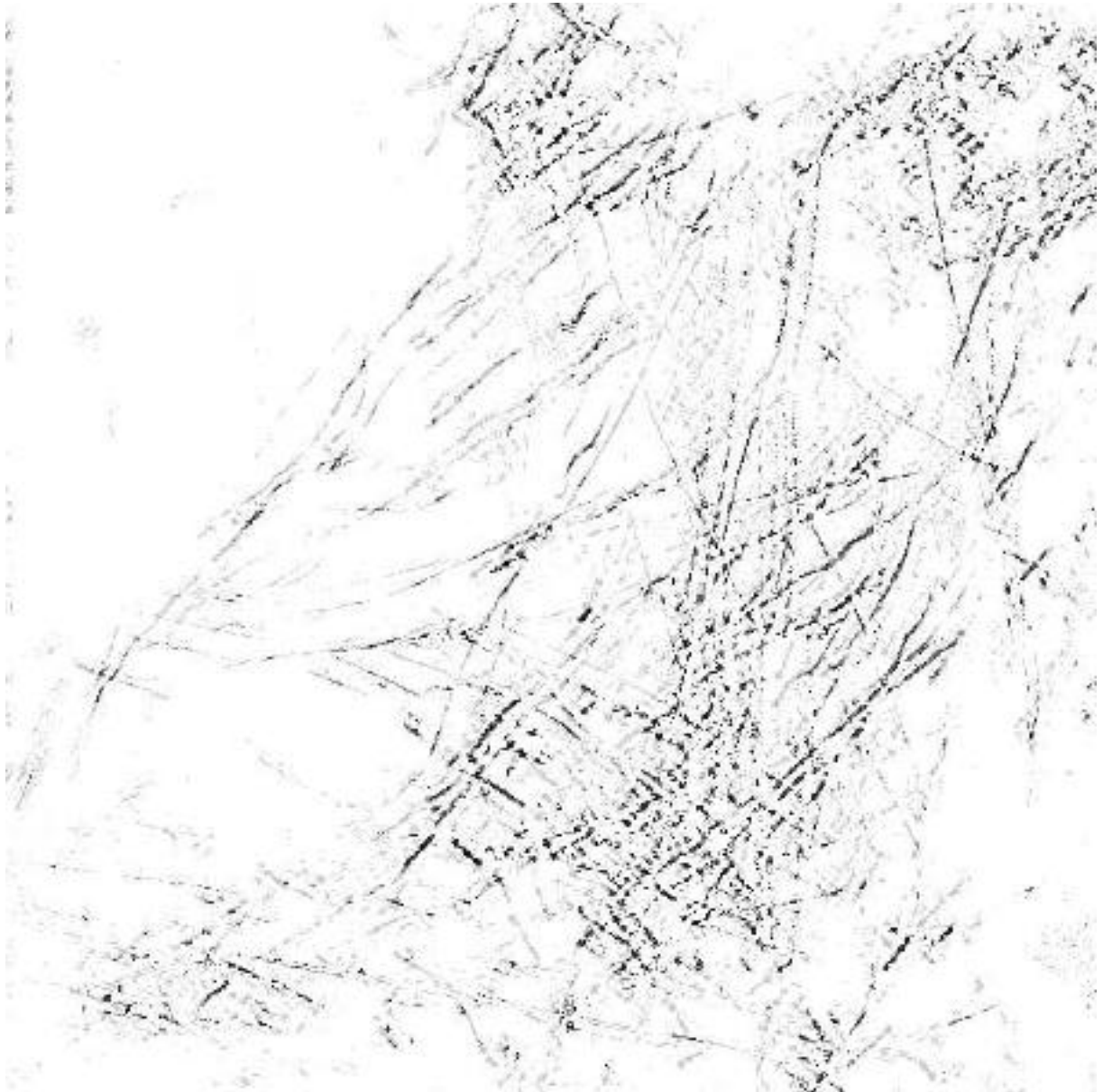


Figure 44. Contrails distinguished by non-linear filtering from AVHRR

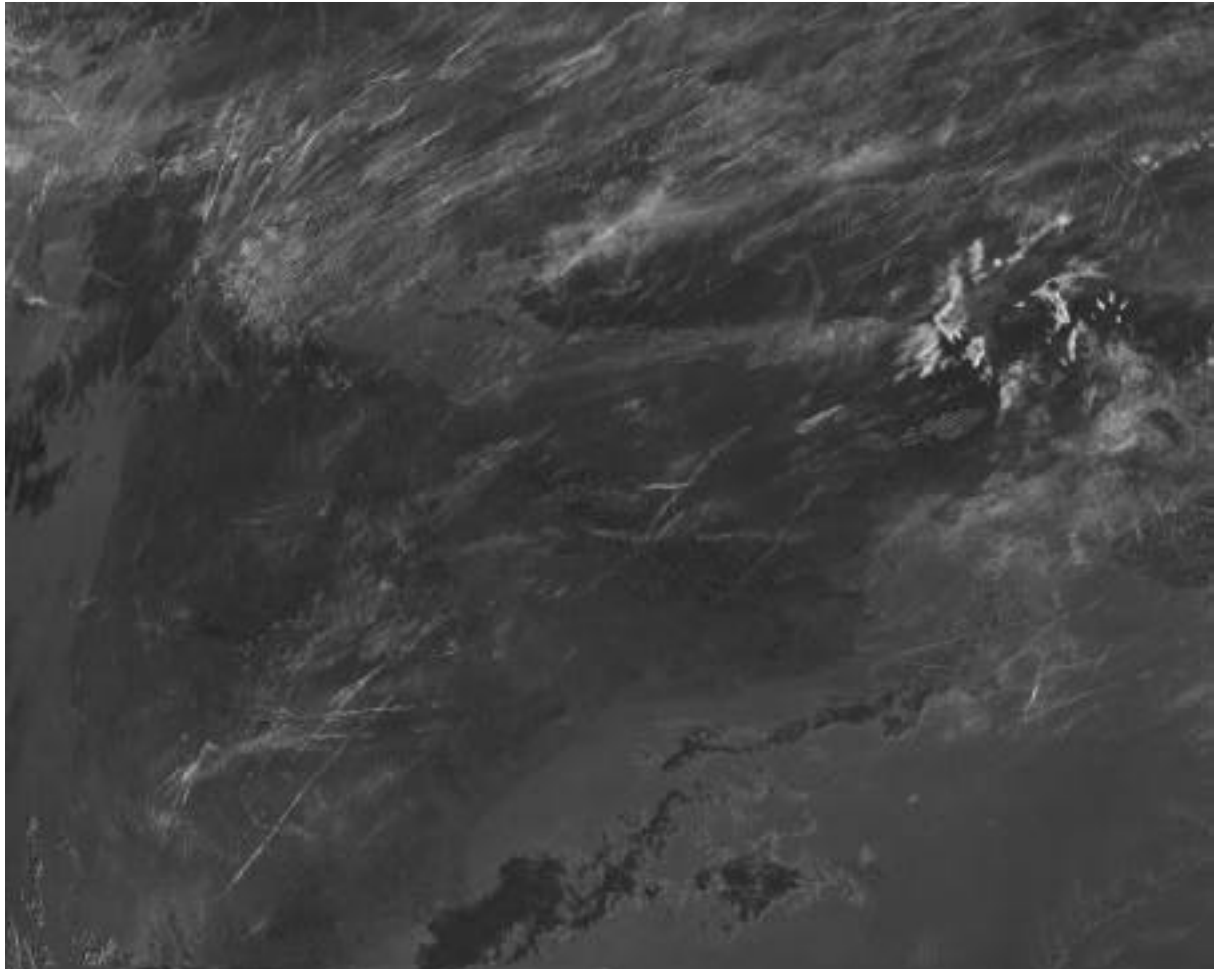


Figure 45. AVHRR image with contrails (original) from AVHRR



Figure 46. Enhancement of lines in the AVHRR image



Figure 47. Isolation of contrails from AVHRR

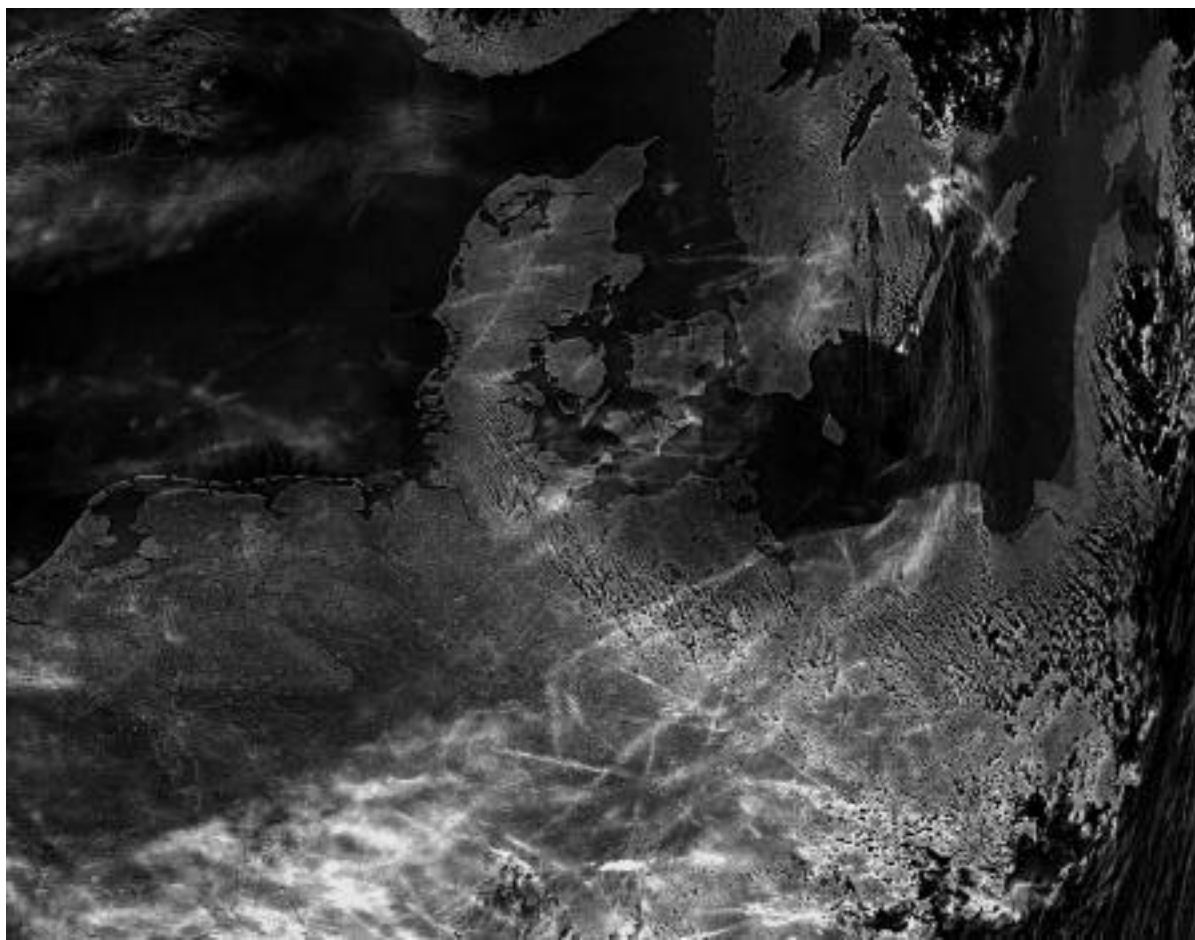


Figure 48. AVHRR image (original)

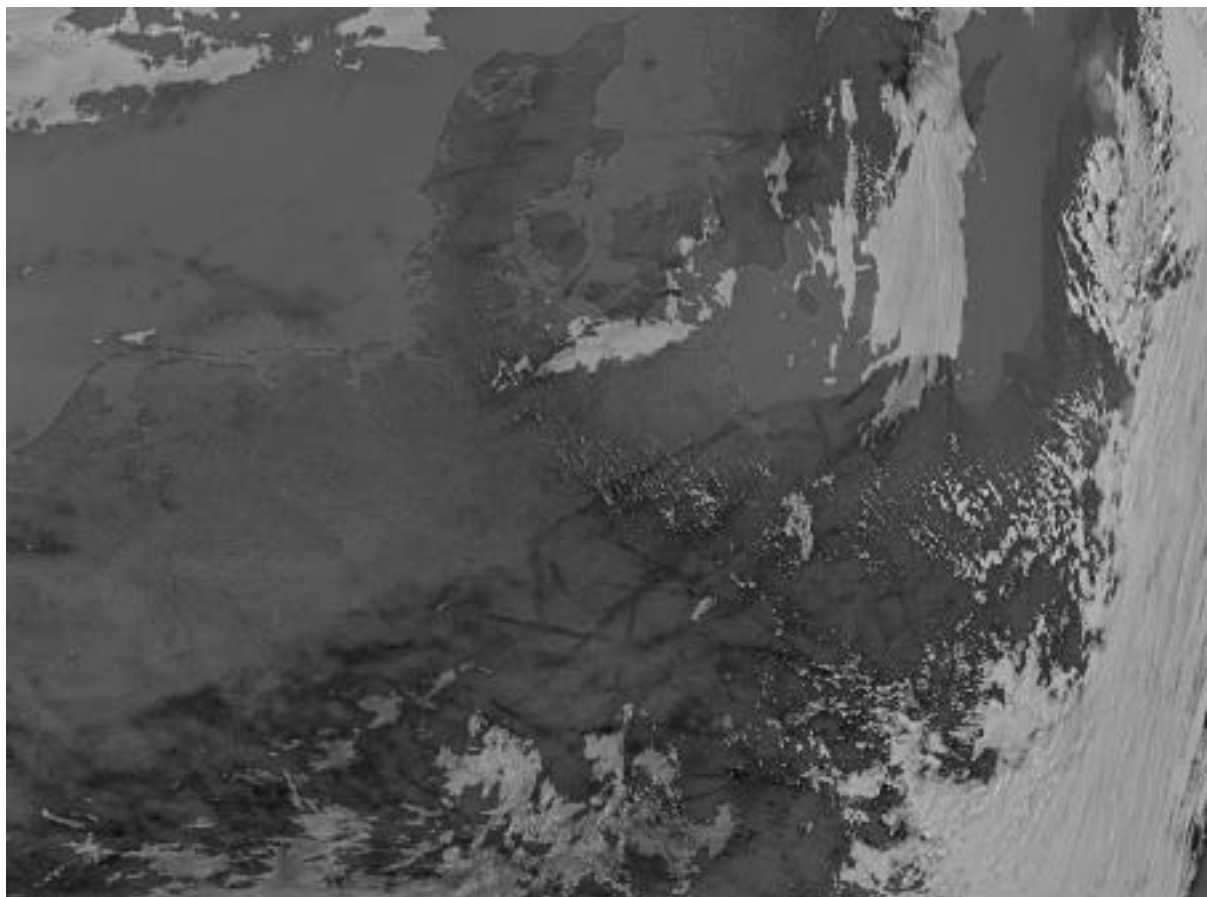


Figure 49. Separation of clouds by structures (characterised brighter) for masking from AVHRR

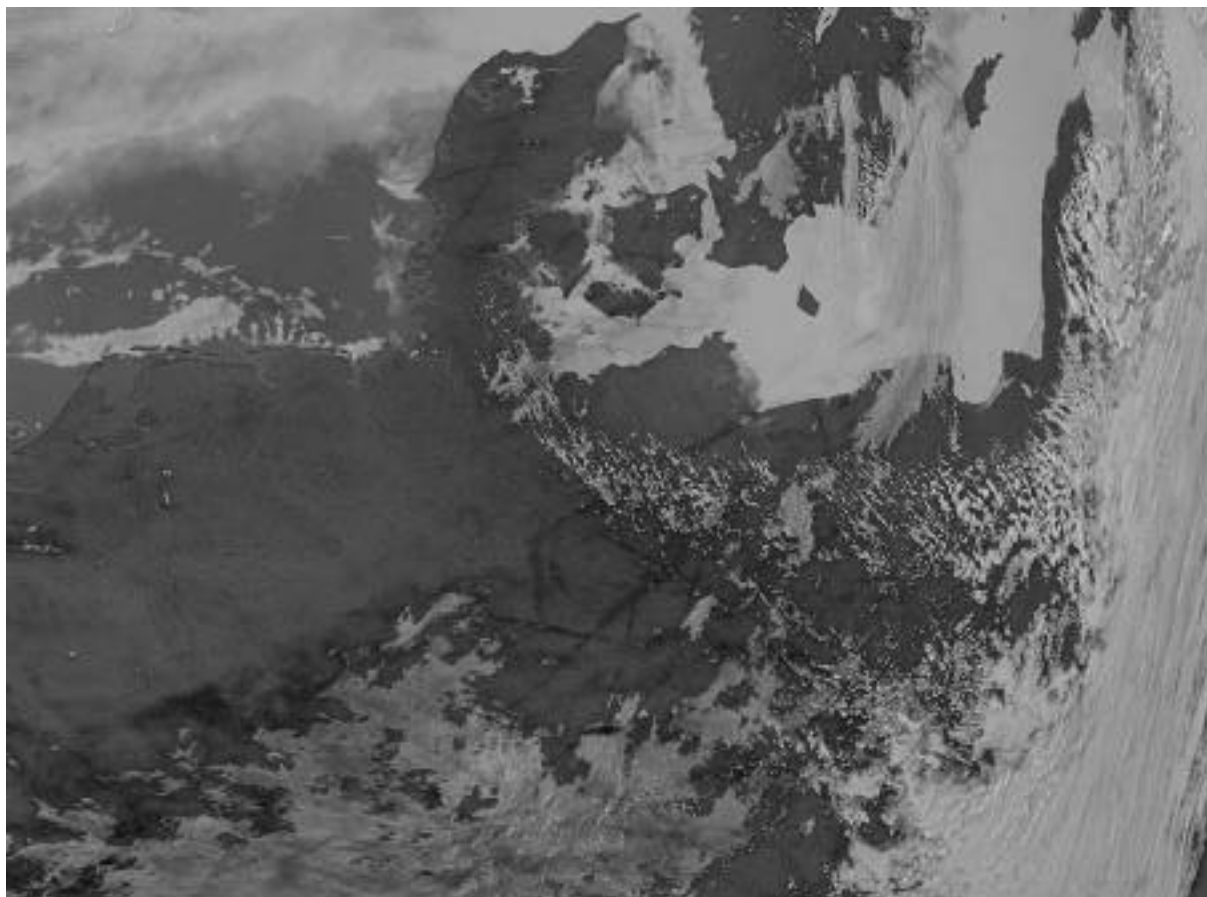


Figure 50. Characterisation of Baltic Sea by textures (represented brighter) from AVHRR

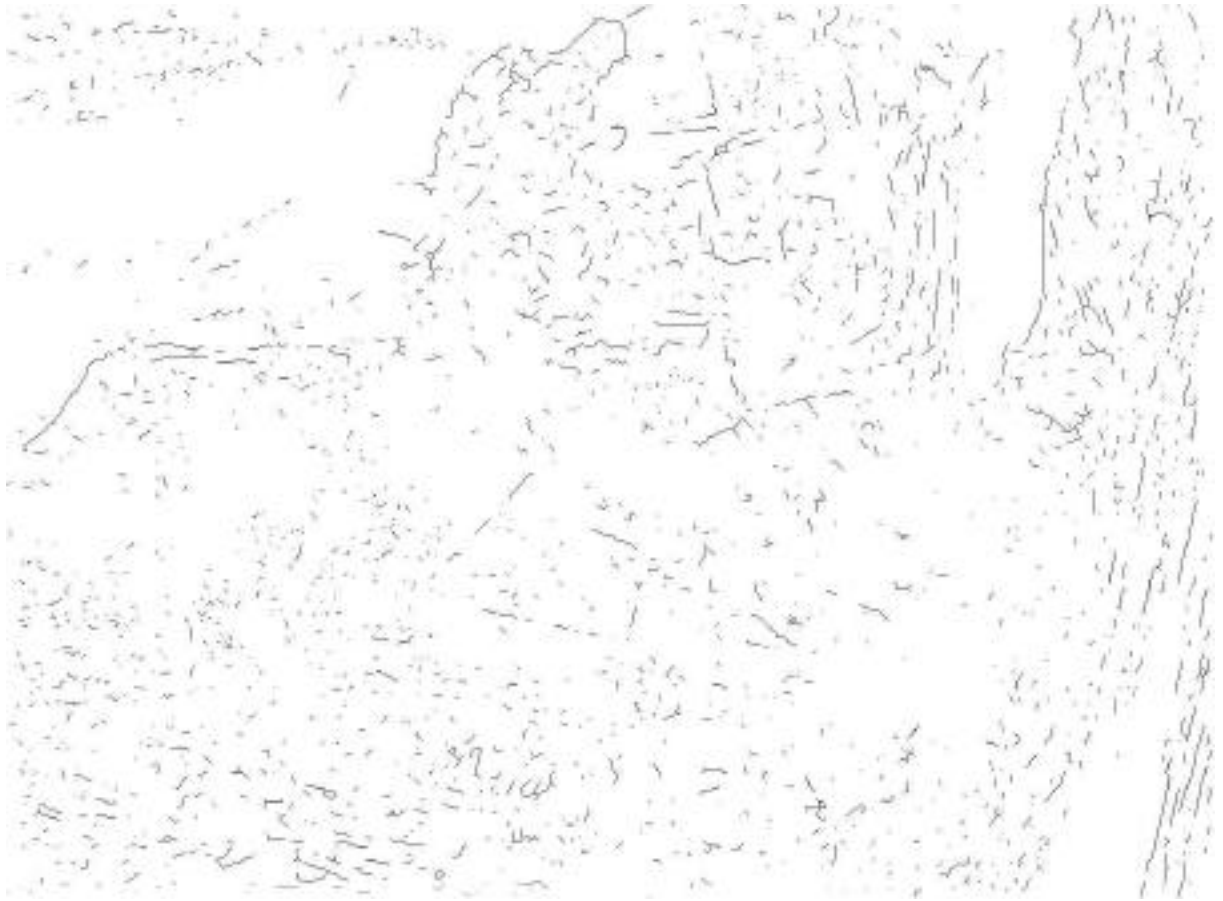


Figure 51. Isolated contrails from AVHRR



Figure 52. AVHRR of region surrounding Denmark without contrails but small clouds



Figure 53. Nearly no contrails are detected from AVHRR

Examples of contrail isolation in MOS images

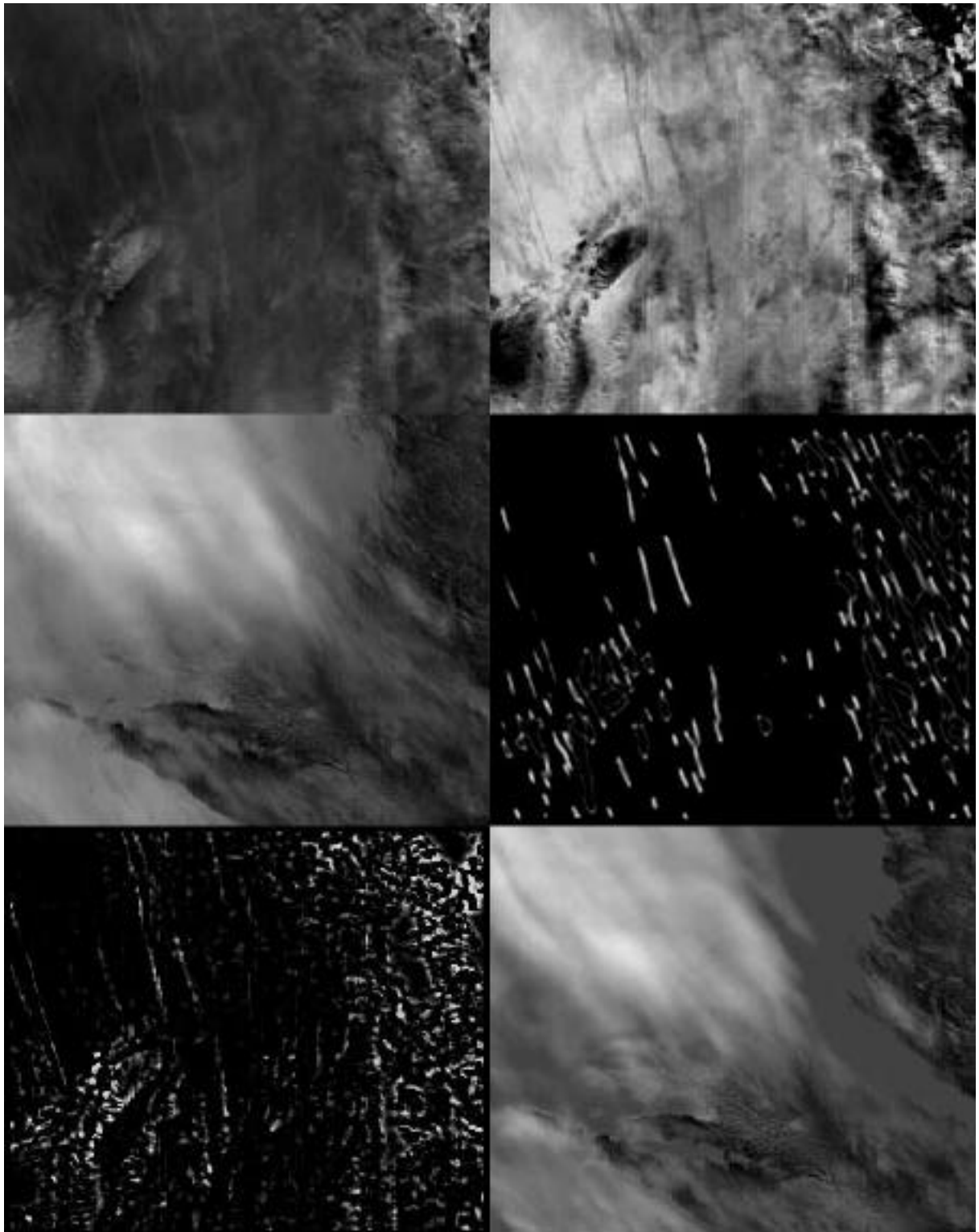


Figure 54. MOS image original left upper with cloud enhancement and contrail isolation



Figure 55. Aged contrails in the middle of the MOS image



Figure 56. Examples of enhancement of the structures of aged contrails from MOS

Examples of contrail isolation in ATSR 2 images

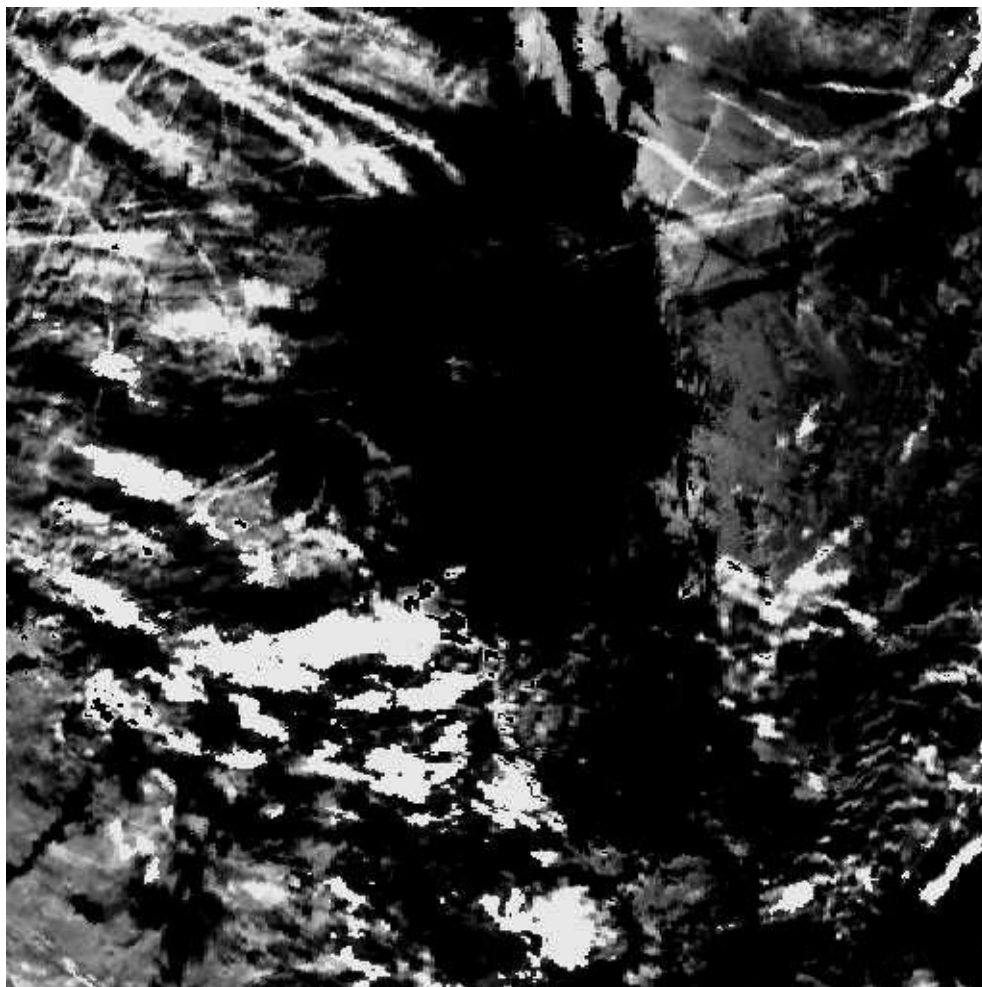


Figure 57. Original ATSR2 image (difference image) with contrails

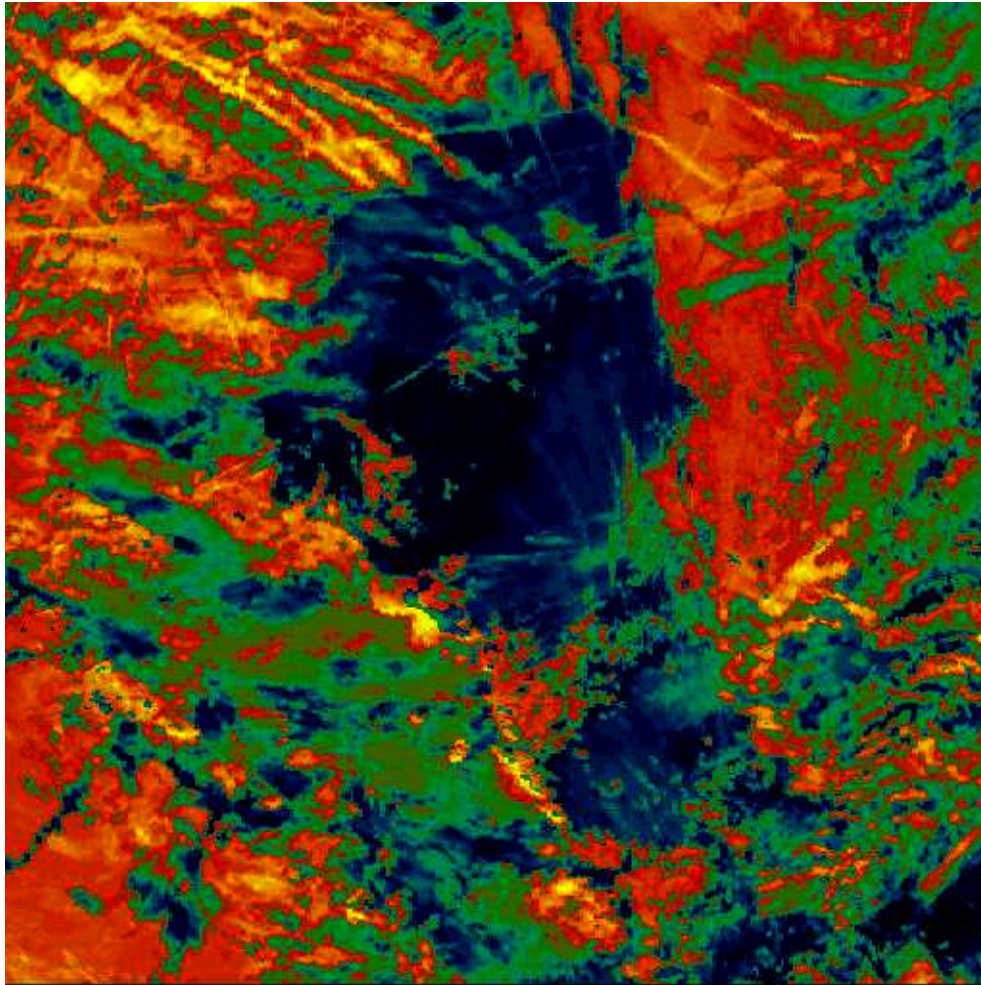


Figure 58. Enhancement of contrails by differences in stochastic from ATSR2

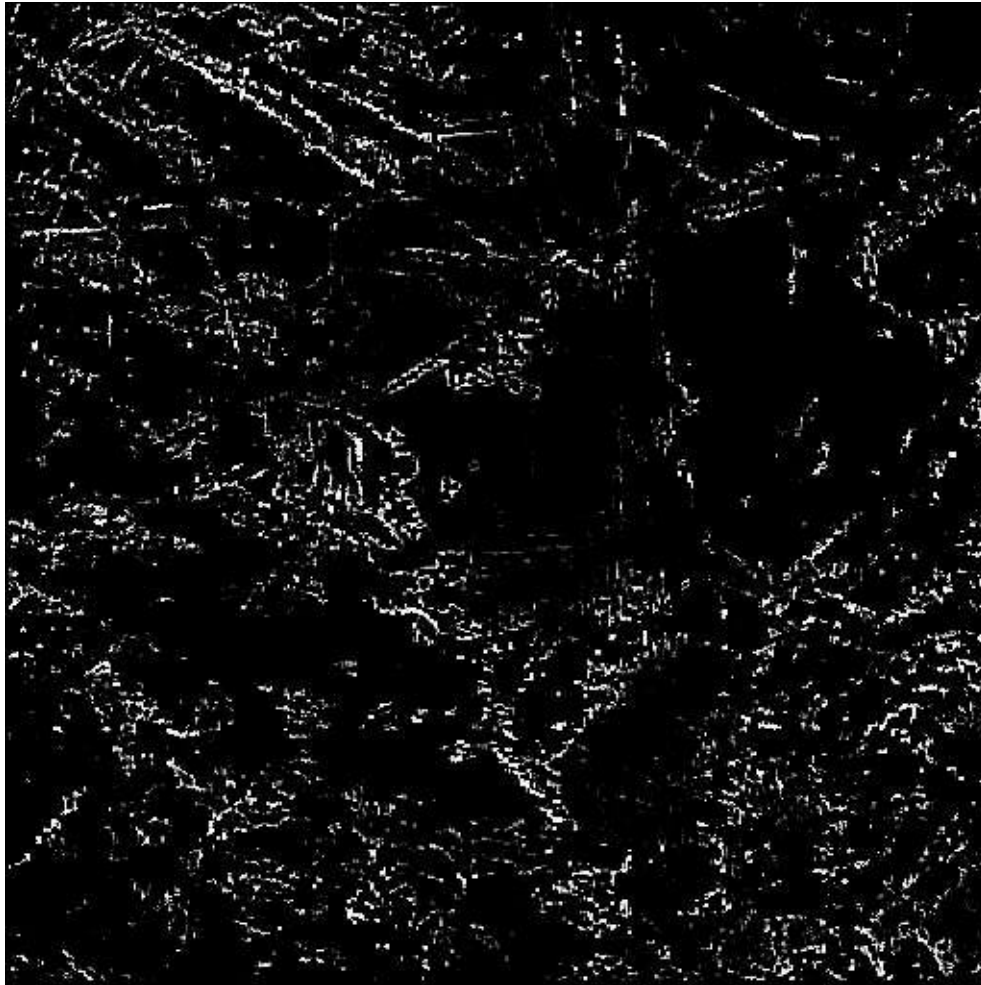


Figure 59. Enhancement of the other region with contrails from ATSR2

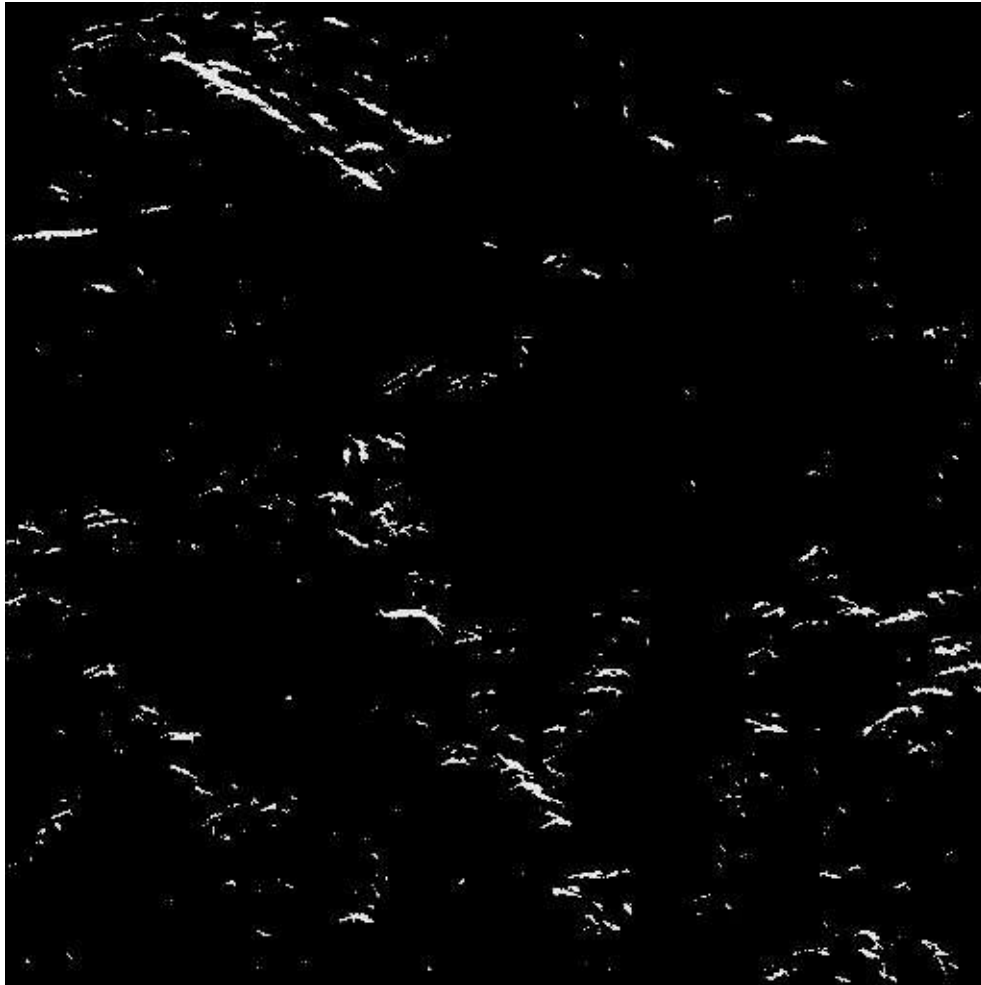


Figure 60. Isolation of the contrails in the ASTER-image

FUB

MOS processing chain

In the second year of the project, the FUB developed a Level-1b and a Level-2 processing software for MOS in the Interactive Data Language (IDL).

Level 1b Processor

The Level 1b processor uses the header information of the original DLR data to produce the complete longitude and latitude array for all pixel. The different spatial resolution of the MOS modules A, B and C requires a re-sampling to a common pixel basis. The FUB level 1b format is based on the spatial resolution of the MOS-B, which is the highest of all modules.

The original MOS data does not contain a geo-location on a pixel by pixel basis. A geo-referencing using coastlines or something similar is not usable for automated procedures since it needs human interaction. A practical solution for defining and finding a common grid uses the facts that: a) the MOS A, B and C imager do not contain mobile parts b) the units are fixed and c) the units have been designed to have

the same field of view. Facts (a) and (b) ensure that a constant relation of the pixel location of the three units exists. These relation p can be used to define MOS B as the common grid and to map MOS A and MOS C on that grid:

$$\begin{aligned}x_{A \rightarrow B} &= p_{X(A \rightarrow B)}(x, y) \\y_{A \rightarrow B} &= p_{Y(A \rightarrow B)}(x, y) \\x_{C \rightarrow B} &= p_{X(C \rightarrow B)}(x, y) \\y_{C \rightarrow B} &= p_{Y(C \rightarrow B)}(x, y)\end{aligned}$$

$p_{X(A \rightarrow B)}$ is the function that evaluates the column number in the MOS A image for a given column (x) and line (y) in the MOS B image. $p_{Y(A \rightarrow B)}$, $p_{X(C \rightarrow B)}$ and $p_{Y(C \rightarrow B)}$ are equivalent functions. Fact (c) allows, that these relations can be approximated by a second order Taylor formula :

$$p(x, y) = a + b * x + c * y + d * (x - x_0)^2 + e * (y - y_0)^2 + f * (x - x_0) (y - y_0) + \epsilon(x, y) \quad (1)$$

where ϵ is the residual term. $(x_0, y_0) = (192, 192)$ is the centre pixel of a MOS B image. Considering the concept of the instrument it is evident that the constant term a and the linear terms b and c dominate the function. They describe a translation (a), scaling and a small rotation (b and c). The quadratic terms d , e and f account for larger rotation angles and non-linear scaling.

Equation (1) is very general. It can be simplified considering that MOS is a nadir looking line scanner. The functions, that evaluate the MOS A and C column number ($p_{X(A \rightarrow B)}$ and $p_{X(C \rightarrow B)}$) can not depend on the MOS B line number y . The parameter c , e and f are therefore zero. The functions, that evaluate the MOS A and C line number ($p_{Y(A \rightarrow B)}$ and $p_{Y(C \rightarrow B)}$) do not depend on the MOS B line number y in a geometric way. Instead they depend on the timing relations between MOS A/C and B which are in fact very accurate. Therefore the parameter c is exactly $128/384 = 1/3$ for $p_{Y(A \rightarrow B)}$ and $384/384 = 1$ for $p_{Y(C \rightarrow B)}$. The parameter e and f are zero for this functions since no non-linearity can occur here. Summing up, equation (1) can be written for each specific case as:

$$p_{X(A \rightarrow B)}(x, y) = a + b * x + d * (x - x_0)^2 \quad (2)$$

$$p_{Y(A \rightarrow B)}(x, y) = a + b * x + 1/3 * y + d * (x - x_0)^2 \quad (3)$$

$$p_{X(C \rightarrow B)}(x, y) = a + b * x + d * (x - x_0)^2 \quad (4)$$

$$p_{Y(C \rightarrow B)}(x, y) = a + b * x + y + d * (x - x_0)^2 \quad (5)$$

Since $p(x, y)$ must be rounded to a fixed number (as column and line numbers are) there is a significance level of required accuracy for each of the coefficients. The accuracy level has been chosen in a way that the sum of the contribution of each inaccuracy is smaller than 0.25 pixel for the worst case. Thereby the inaccuracies can not change the resulting column and line numbers. Since there are three coefficients, the contribution of each coefficient has to be smaller than $0.25/3$. The significant accuracy is listed in Table 7

Table 7. : Significant accuracy level of coefficients a, b and d

coefficient	a	b	d
accuracy	1/12	(1/12)/384 2e-04	(1/12)/192 ² 2e-06

To find the coefficients a, b and d, 100 MOS images of west and middle Europe between 1996 and 1998 have been chosen. The algorithm consists on two steps:

1. All images were edge-enhanced by using the Roberts operator: $roberts(x,y)=|image(x,y)-image(x+1,y+1)|+|image(x+1,y)-image(x,y+1)|$ which is in fact a two dimensional differencing method for edge sharpening.
2. The resulting images of MOS C and MOS A were mapped to the corresponding MOS B image using equations (3)-(5). The best coefficients a, b and d of each equation and of each image combination have been found by using the downhill simplex algorithm of Nelder and Mead (1988). These coefficients maximise the correlation coefficient between MOS A/C and MOS B.

Table 8. Mean value and standard deviation of the parameter of equation (2)-(5)

	a		b		d	
	mean	stdv	mean	stdv	mean	stdv
$p_{X(A \rightarrow B)}(x,y)$	-3.10	0.03	0.3894	0.0005	2.4e-07	0.5e-07
$p_{Y(A \rightarrow B)}(x,y)$	-0.21	0.02	-0.0046	1.5e-06	0.5e-07	1.2e-07
$p_{X(C \rightarrow B)}(x,y)$	45.2	0.05	0.7790	0.0020	6.9e-07	6.0e-07
$p_{Y(C \rightarrow B)}(x,y)$	-8.10	0.05	0.0140	1.9e-06	3.0e-07	5.0e-07

In Table 8 the mean values (*mean*) and the standard deviation (*stdv*) of the parameters are listed. Comparing Table (2) and Table (1) it can be concluded that second order terms are not necessary to describe the relation between MOS A/C and MOS B since the values of *d* are smaller than the corresponding significant accuracy. Equations (2)-(5) can be simplified to:

$$p_{X(A \rightarrow B)}(x,y)=a+b*x \quad (6)$$

$$p_{Y(A \rightarrow B)}(x,y)=a+b*x+1/3*y \quad (7)$$

$$p_{X(C \rightarrow B)}(x,y)=a+b*x \quad (8)$$

$$p_{Y(C \rightarrow B)}(x,y)=a+b*x+y \quad (9)$$

The margin pixels of MOS B and MOS C are outside the viewing range of MOS A. Equations (6) and (8) are used to evaluate the minimum and maximum pixel number of Unit B and C that is seen by all units. The results are listed in

Table 9.

Table 9. Minimum and maximum of column number including the common viewing range of the three MOS units.

	MOS B	MOS C
Minimum	8	51
Maximum	364	329

Classification algorithm

An additional FUB extension is a pixel classification product. A first version of the classification is based on a multispectral threshold approach to distinguish between clouds, desert, vegetated land and ocean. Currently, a more sophisticated classification method is under development. This method uses artificial neural network training to generalize manually derived classifications. The GUI based software tool Training Area Selection Kit (TASK) for manual classification of MOS has been realized with IDL (Figure 61). The main part of the widget is the display of a single MOS scene in a RGB representation. The operator is able to change the appearance of the scene by changing the MOS channels and by applying histogram equalisation or other display enhancement techniques. Map projection and land-sea masking are included for better image navigation. The operator selects image regions with cursor and mouse and assigns the selected pixels to one of the following classes:

1. cirrus cloud over land
2. non-cirrus cloud over land
3. cirrus cloud over ocean
4. non-cirrus cloud over ocean
5. vegetated land surface
6. ice surface
7. desert surface

This tool will be used to build up a data base to create training data for the neural network inversion. This kind of supervised learning will result in an operational classification algorithm which will assign the MOS pixels to the above mentioned classes or to an additional class called »unclassified«.

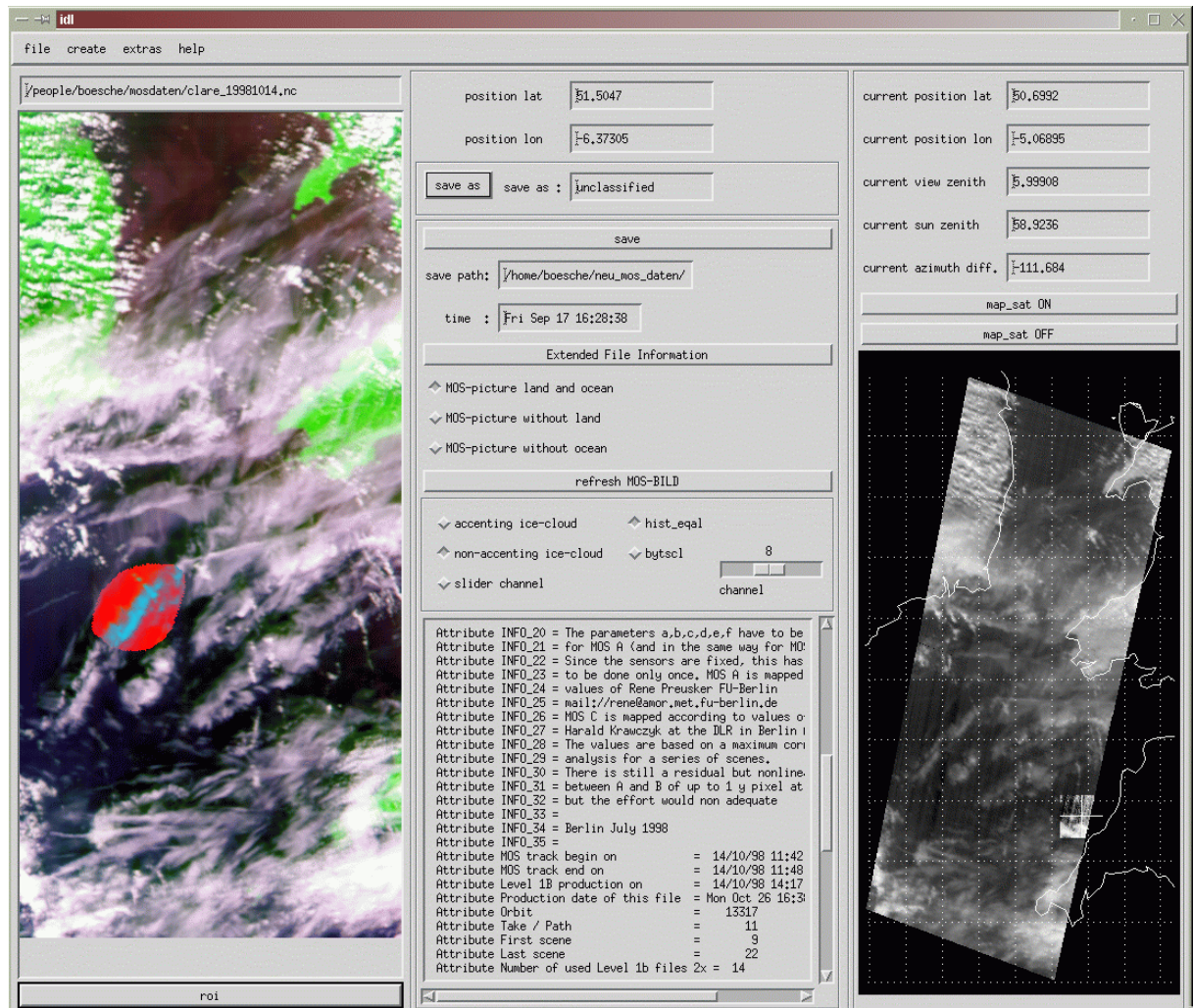


Figure 61: Screenshot of the MOS classification tool for a manual definition of training areas

Level 2 Processor

The newly developed MOS level 2 processor for automatic calculation of the FUB Level 2 products was tested and operated. The different algorithms can be applied to the Level 1b data and the products are then stored in a Level 2 file in NetCDF-Format together with the longitude and latitude information. It is possible to add new products to or update existing products in a Level 2- NetCDF file. The following Level 2 algorithms are included in the Processor up to now:

- cloud top pressure
- cloud optical thickness
- cloud effective radius
- cloud droplet concentration
- cloud albedo

The surface albedo as interpolated from the ISLSCP data set which is needed for the cloud algorithms is also treated as an level 2 product.

Cloud-top Pressure

Re-calculation of inversion matrices

The problem of the absolute value of the derived cloud top pressures was resolved. Within the radiative transfer model MOMO, the treatment of absorption due to atmospheric gases has been significantly improved by the implementation of the » k-distribution method « instead of the »Exponential Sum Fit of Transmission (ESFT)« which produced large errors in the calculation of radiances within the oxygen A band. The simulated radiances are now within the typical range as observed by the MOS instrument. Figure 62 demonstrates that a thin cirrus could be detected over a stratocumulus field and that the retrieval result is consistent with typical cloud top pressure values of cirrus and stratocumulus.

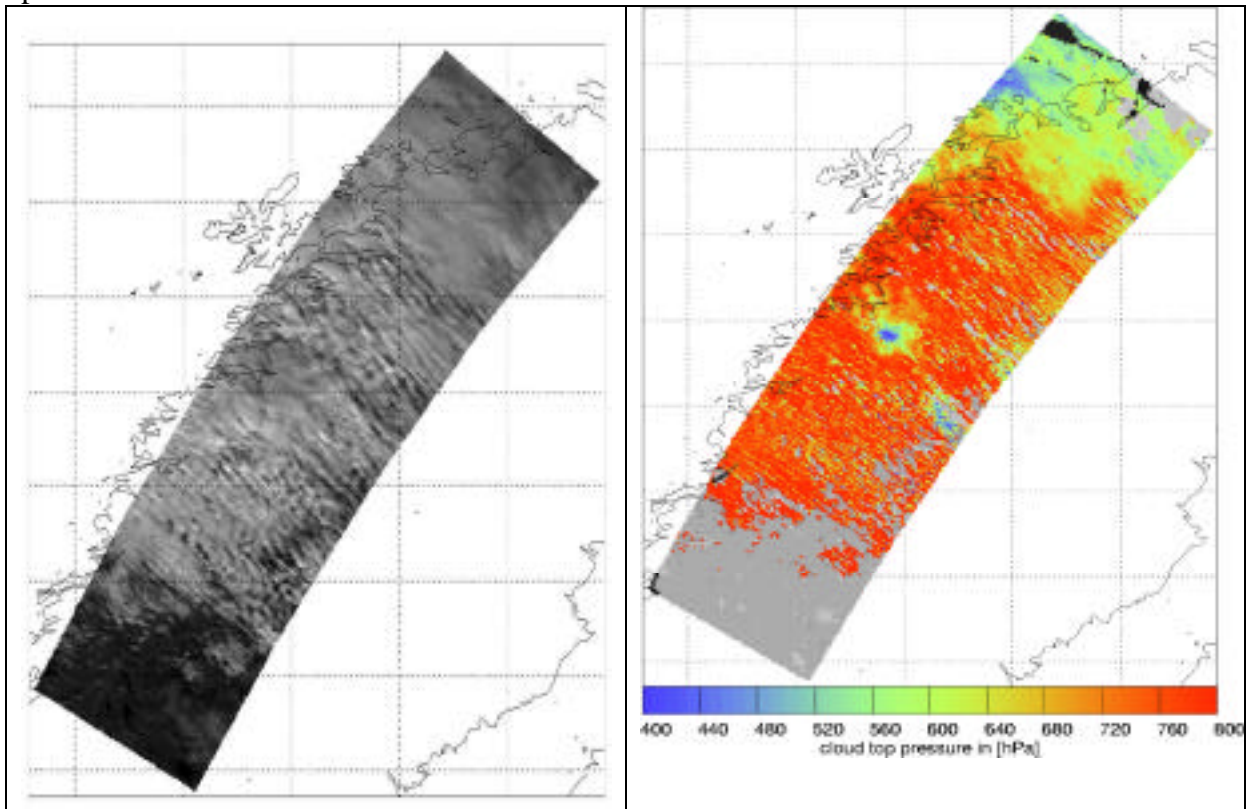


Figure 62. Left: MOS radiance in channel 9 at 750nm. Right: Retrieved cloud top pressure in hPa

Determination of the theoretical limits of the algorithm

The following sections describe the sensitivity of the retrieval on the variation of several parameters. MOS images of a representative swath has been simulated with a specific value of the cloud optical thickness, cloud top pressure etc. The simulated radiances were used as input parameters for the retrieval algorithm. The root mean square error RMSE and the BIAS can be determined by comparing actual and retrieved cloud top pressure. The ill posed nature of the inversion as well as the shortcomings of radiative transfer modelling and instrumental characteristics will affect the accuracy of the cloud top pressure algorithm. The overall *RMSE* is 33hPa for an instrumental Gaussian noise of 0.5%. Sensitivity studies on the influence of

these errors have been performed to acquire the most sensitive properties of the algorithm. The root mean square error *RMSE* and the BIAS are used to characterise the accuracy. All investigations described in the following paragraphs have been made for an instrumental Gaussian noise of 0.5%

Sensitivity to surface albedo and cloud optical thickness

The influence of the surface to the reflectance at the top of the atmosphere and therewith the accuracy of the cloud top pressure algorithm increased with decreasing cloud optical thickness and increasing surface reflection. Especially a combination of thin clouds over bright surfaces leads to an overestimation of the cloud top pressure and thereby to an increasing algorithm error. This is due to the ambiguity of the inverse problem according to cloud optical thickness, surface albedo and penetration depth. For moderate optical thickness and surface albedo the BIAS is negligible. The *RMSE* is below 30hPa for most cloud and surface reflectances which usually occur (Figure 63).

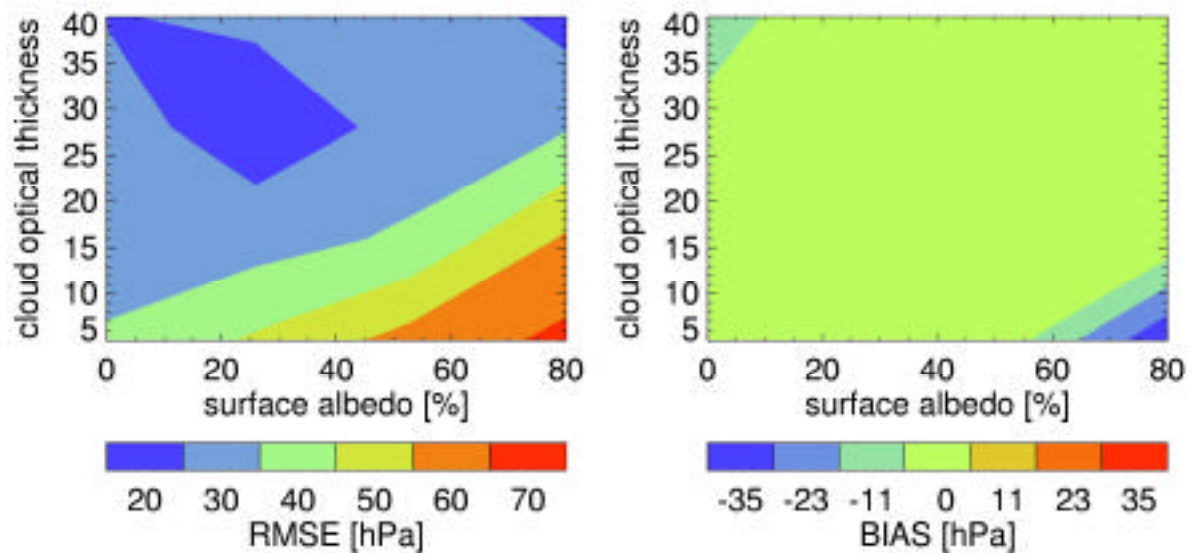


Figure 63: Sensitivity of the ctp algorithm to cloud optical thickness and surface albedo. A negative BIAS (blue) means overestimation of the cloud top pressure

Since the surface albedo can only be known to a certain accuracy the surface albedo of the test data was varied to study this influence. Errors in the albedo of up to 0.2 (*RMSE*) have been simulated (Figure 64) Again thin clouds and bright surfaces are the most sensitive conditions. Considering that the natural occurrence of thin clouds is higher than of thick clouds the precise knowledge of the surface albedo is a key factor for determining the CTP accuracy.

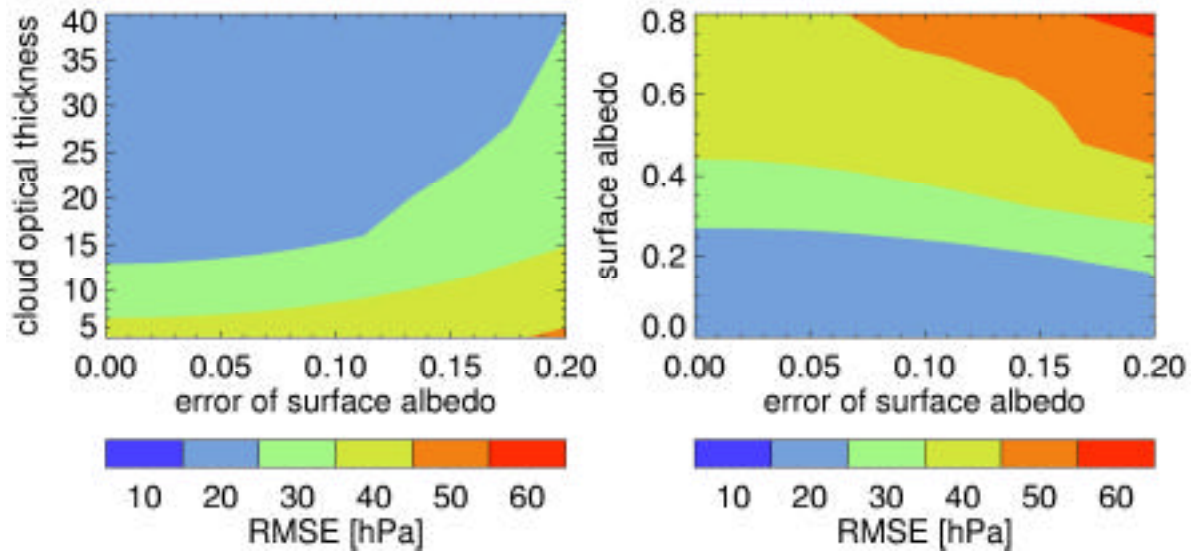


Figure 64: Sensitivity of the ctp algorithm to the error of the surface albedo as a function of the cloud thickness (left) and the surface albedo (right).

Sensitivity to cloud optical thickness and cloud top pressure

As outlined in the last section the accuracy of the CTP algorithm decrease with decreasing cloud optical thickness since the influence of the surface increases. The impact is different for different cloud top pressures. The cloud top pressure of low thin clouds will be underestimated in contrary to higher (between 800 hPa and 700 hPa) thin clouds which will be overestimated (Figure 65 right). As in the previous section the reason is the ambiguity of the inverse problem according to cloud optical thickness, surface albedo and penetration depth. This leads to an *RMSE* of the retrieved CTP of up to 55 hPa (red areas Figure 65 left), which is substantially higher than the overall *RMSE* of 33hPa.

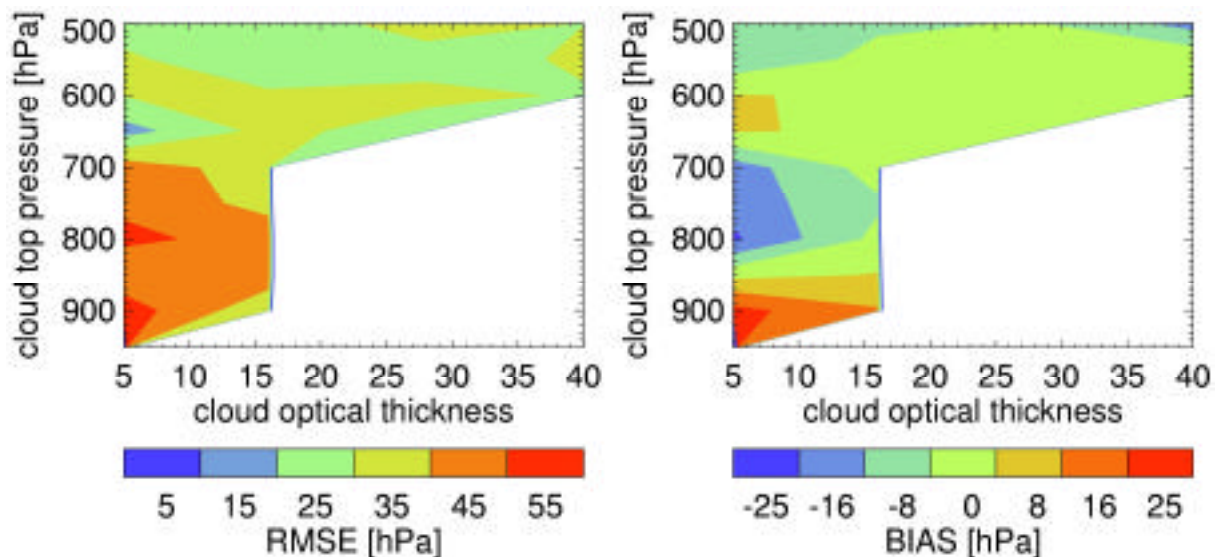


Figure 65: Sensitivity of the cloud top pressure retrieval to cloud optical thickness and cloud top pressure. The white areas are not represented in the test and training database.

Cloud optical thickness

Calculation of regression coefficients

A cloud optical thickness retrieval algorithm has been developed which is based on measurements in channel 10 at 750nm. The inversion is performed by regression of numerous radiative transfer simulations for cloudy atmospheres over ocean as well as over land considering the natural variability of the influencing parameters (droplet radius, cloud top height and geometrical thickness, aerosols, observational conditions, surface albedo etc.).

To estimate the underlying surface albedo at cloudy MOS pixel, the ISLSCP data are used up to now, although it is planned to use other satellite estimates with higher spatial resolution. The dependence of the cloud optical thickness from the measured radiance at 750nm will be approximated with the following function:

$$\tau_c = \exp(b_0 + b_1 \times L + b_2 \times L^2 + b_3 \times L^3) \quad (10)$$

where the coefficients b_0 to b_3 are determined by regression. A separate set of regression coefficients are calculated for each combination of viewing and solar zenith angles, azimuth angle and surface albedo.

Determination of the theoretical algorithm error

The following sections describe the sensitivity of the retrieval on the variation of several parameters. MOS images of an representative swath were simulated with a specific value of the cloud optical thickness. The simulated radiances were used as input parameters for the retrieval algorithm. The root mean square error RMSE and the BIAS can be determined by comparing simulated and retrieval optical thickness

Sensitivity to cloud optical thickness and cloud top height

The sensitivity to cloud optical thickness and cloud top height variations has been analysed with the general finding, that the RMSE (root mean square error) increases with optical thickness. For typical values of $\tau_c = 50$ a RMSE = 9 (Figure 66) has been estimated.

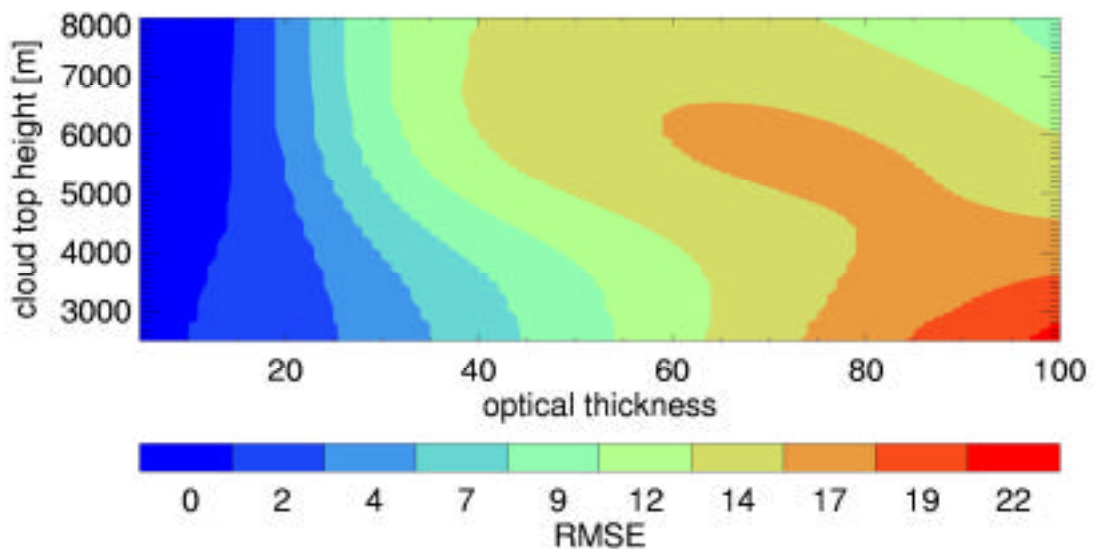


Figure 66: RMSE of cloud optical thickness retrieval as function of cloud optical thickness and cloud top pressure.

The influence of the cloud top height is obvious with a general tendency to higher RMSE values for higher cloud top heights. The BIAS (Figure 67) drastically increases with cloud top heights. Optically thick and low clouds are underestimated with respect to the optical thickness.

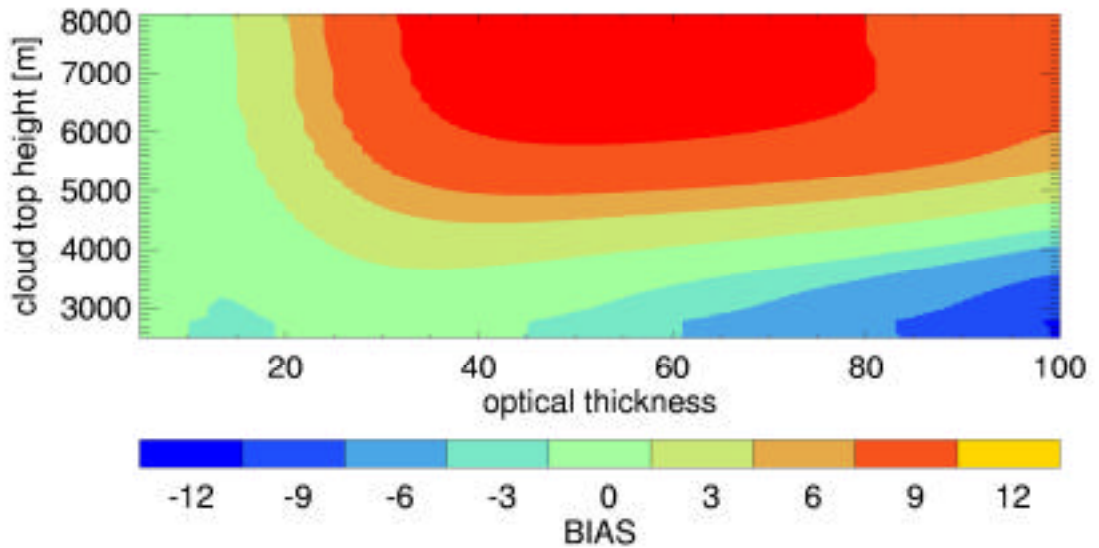


Figure 67: BIAS of cloud optical thickness retrieval as function of cloud optical thickness and cloud top pressure

Sensitivity of cloud optical thickness retrieval to surface albedo

The root mean square error RMSE (Figure 68) is lower at high and low surface albedo values when the optical thickness is smaller than 50. The largest errors occurs at surface albedos of 50% and high optical thickness. These results have to be interpreted with respect to the algorithm development which is driven by the minimisation of the overall errors.

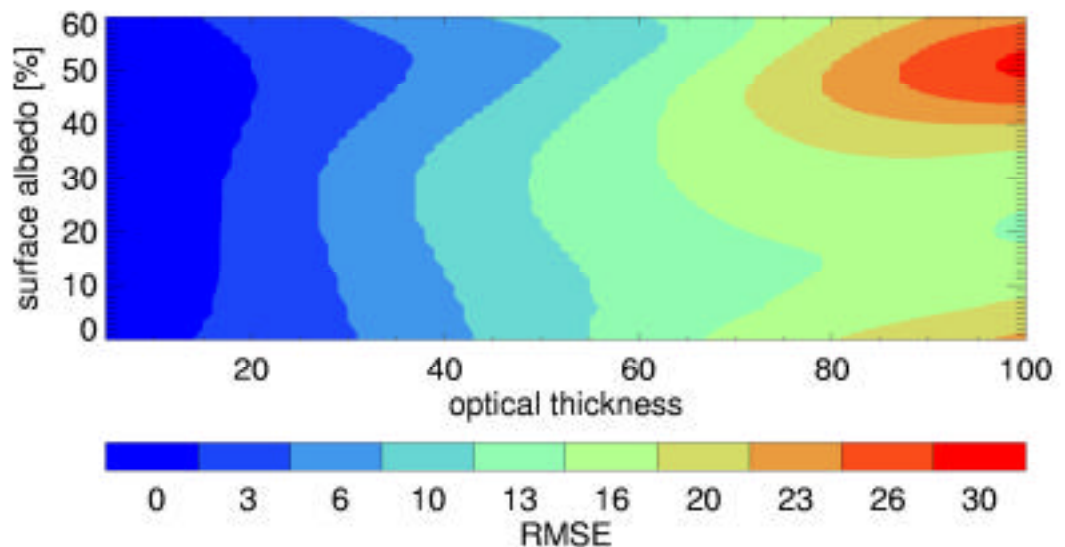


Figure 68: RMSE of cloud optical thickness retrieval as function of cloud optical thickness and surface albedo

Figure 69 shows the BIAS of the retrieved optical thickness. The lowest values for the BIAS are found for optical thicknesses of $\tau_c \sim 50$.

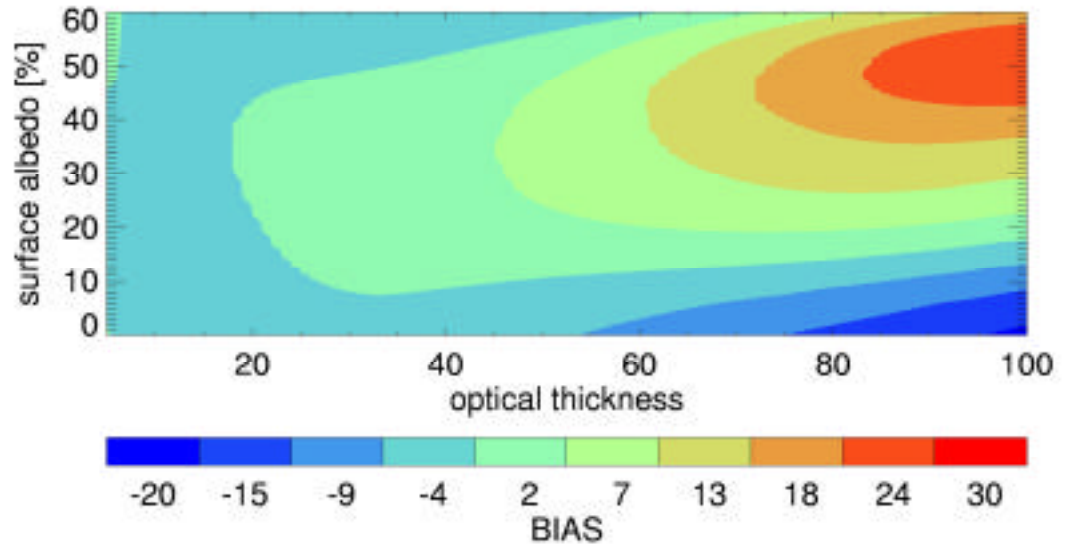


Figure 69: BIAS of cloud optical thickness retrieval as function of cloud optical thickness and surface albedo

Sensitivity to cloud optical thickness and instrumental noise

Figure 70 and Figure 71 show the sensitivity of the cloud optical thickness retrieval to cloud optical thickness and instrumental noise. The sensitivity of cloud optical thickness to instrumental noise is low compared to the sensitivity to other parameters. Within the considered range RMSE values between 0.03 and 0.07 % are found. The BIAS is more important and reaches values up to $\epsilon \sim -12$.

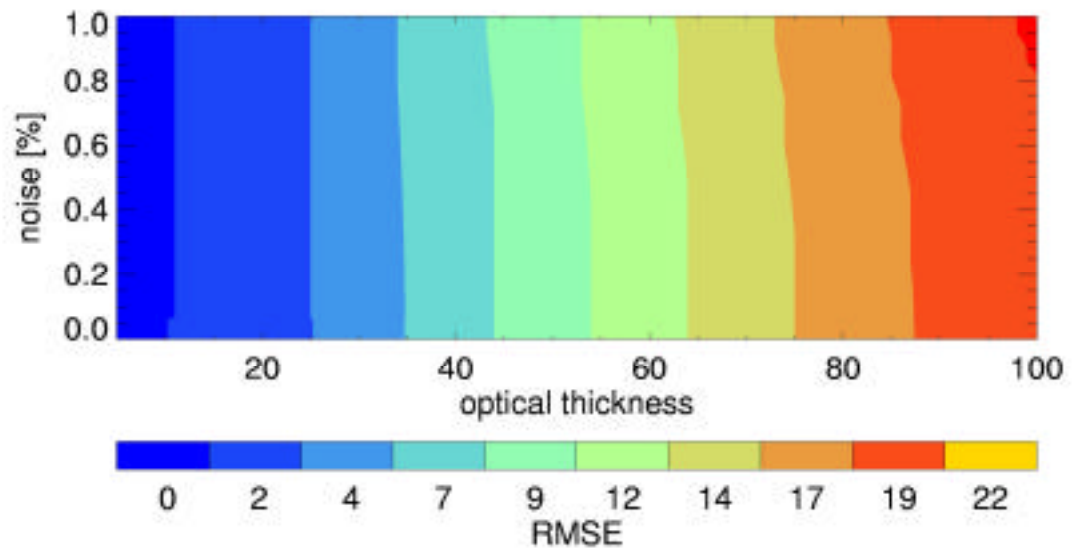


Figure 70: RMSE of cloud optical thickness retrieval as function of cloud optical thickness and instrumental noise.

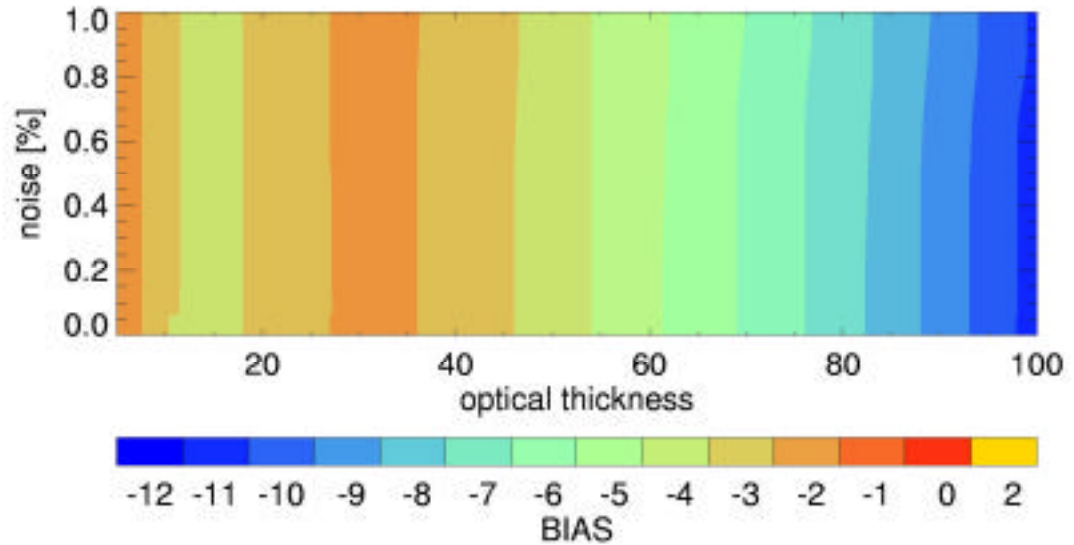


Figure 71: BIAS of cloud optical thickness retrieval as function of cloud optical thickness and instrumental noise

Cloud effective radius and cloud droplet concentration

The algorithms for the retrieval of cloud effective radius and cloud droplet concentration has been adopted to the spectral characteristics of the MOS sensor. The retrieval principle and the structure of the algorithm remains the same as for the OVID sensor (see CLOUDMAP first annual report). The algorithms use measurements with MOS channel at 750nm and at 1.6 μ m.

FUBISS

The Free University Berlin Integrated Spectrometric System FUBISS was operated during the CLARE 1998 campaign from the FALCON aircraft together with a LIDAR system. It consists of up to three spectrometric units covering the UV, visible and near infrared spectral region with different spectral resolution. With its high resolution measurements within the O₂ A band, cloud top pressure can be derived and compared with LIDAR cloud top heights.

The development of an integrated calibration and processing algorithm is completed. The processor converts binary raw data into radiance values and combines them with additional data, e.g. the aircraft navigation.

The retrieval of geophysical parameters from FUBISS measurements has not been implemented in an operational level 2 processor. The adjustment of the MOS algorithms to the spectral characteristics of FUBISS will be completed in the next year of the CLOUDMAP project.

Value-added data production

UCL

ATSR2 Stereo Cloud-Top Height Maps

ESA supplied 80 (51 daytime and 29 night-time) ATSR2 level 1b scenes over the UK which included the Chilbolton Radar site through the ESA data grant and 13 ATSR2 daytime scenes over the Netherlands during the CLARA96 experiment discussed in section 3.1. A full listing is given in section 3.3.2.1.1.

A subset of these during and close to the CLARA96 and CLARE98 field experiment were processed using the automated IDL processing chain described in section 3.3.3.1.1. The results from CLARA96 are shown in section 3.3.1.4. We will focus here on results from 23 October 1998 as ground-based stereo images are available as well as 94GHz radar data from GKSS.

Figure 72 shows the ATSR2 11 μ m stereo pair for 23/10/98 including a blow-up of the area around Chilbolton as an inset.

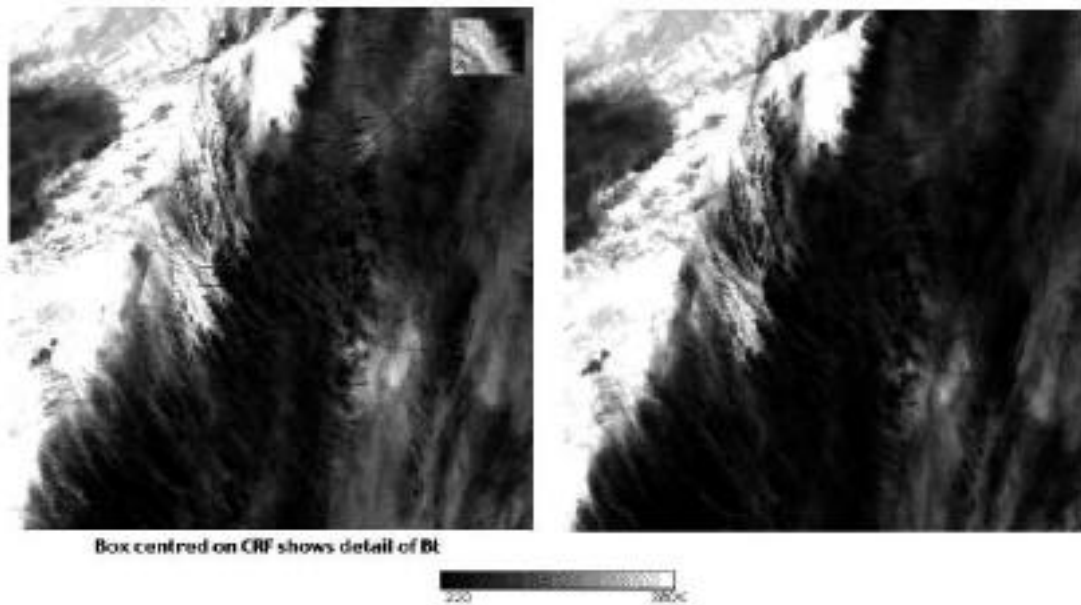


Figure 72. ATSR2 stereo-pair (left- nadir, right-forward) acquired on 23.10.98 over the Chilbolton site including a small inset on the nadir around the Chilbolton site.

Using the IDL processing chain, stereo derived cloud-top heights were obtained which are shown in Figure 73. X marks the position of the Chilbolton radar in the map schematic. Note the predominance of high but broken clouds over most of England with gaps around the position of Chilbolton. Clouds are predominantly high in the stereo which contrasts strongly with the brightness temperature results (not shown here).

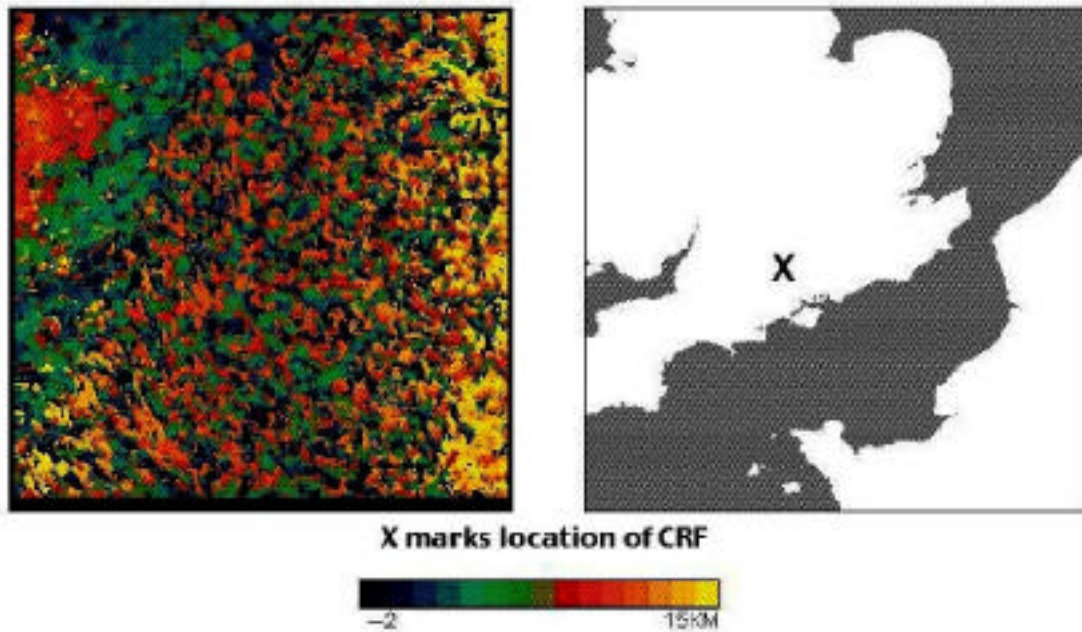


Figure 73. ATSR2 stereo Cloud-Top Heights (left) together with map schematic (right) showing the location of the Chilbolton radar site as a “X”.

AirMISR Stereo Cloud-top heights

The AirMISR processing chain described in section 3.3.1.2 was applied to Run 3 of the AirMISR overpasses acquired on 3rd June 1999.

A number of experiments were carried out to study the characteristics of both the data and the resulting stereo matched Cloud-Top heights.

Firstly, several stereo-pairs were matched in both directions and the resulting distribution of points found by the matcher and the reverses of the matches are very similar eg An to Af and Af to An (referred to below as AnAf and AfAn).

This is illustrated in Figure 74 using histograms of the stereo-matched disparities. Also shown is the fact that the disparities are different between the forward and Aft cameras even though the angles are similar (see later discussion). This is believed to be due to the fact that there was a small error of some 1° in knowledge of the pointing angle for the forward cameras as this was also noticed with the Bf and Cf cameras.

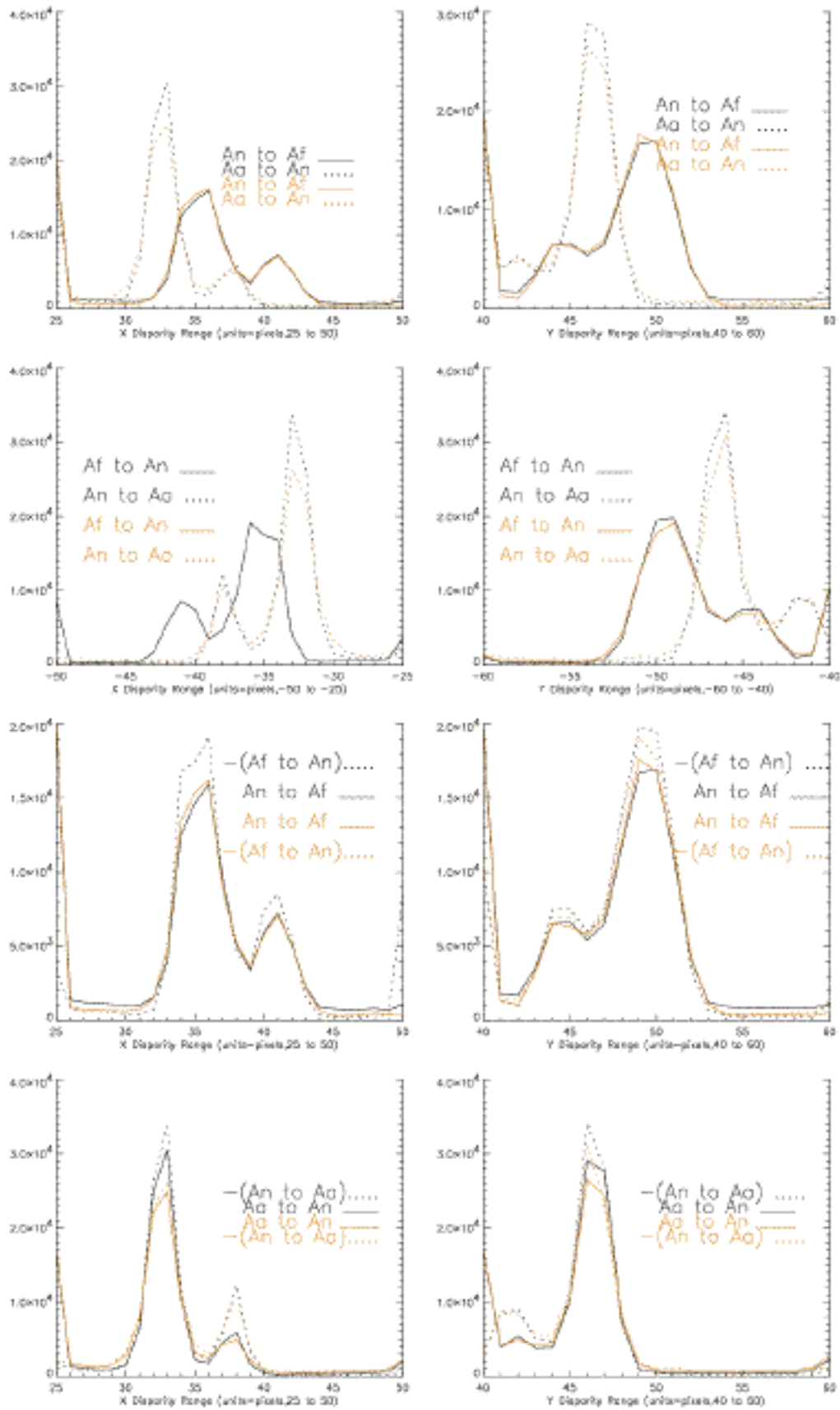


Figure 74. Histograms of stereo matched disparities between AnAf, AfAn, AnAa and AaAn

Stereo-matched heights from the different AirMISR cameras are shown in Figure 75. This illustrates the effect of increasing height as a function of camera angle and the greater heights for the forward cameras compared to the aft due to the uncertainty in the forward angle pointing vector which Dr Marchand (MISR Cloud Validation scientist) has shown is due to an uncertainty of 1° .

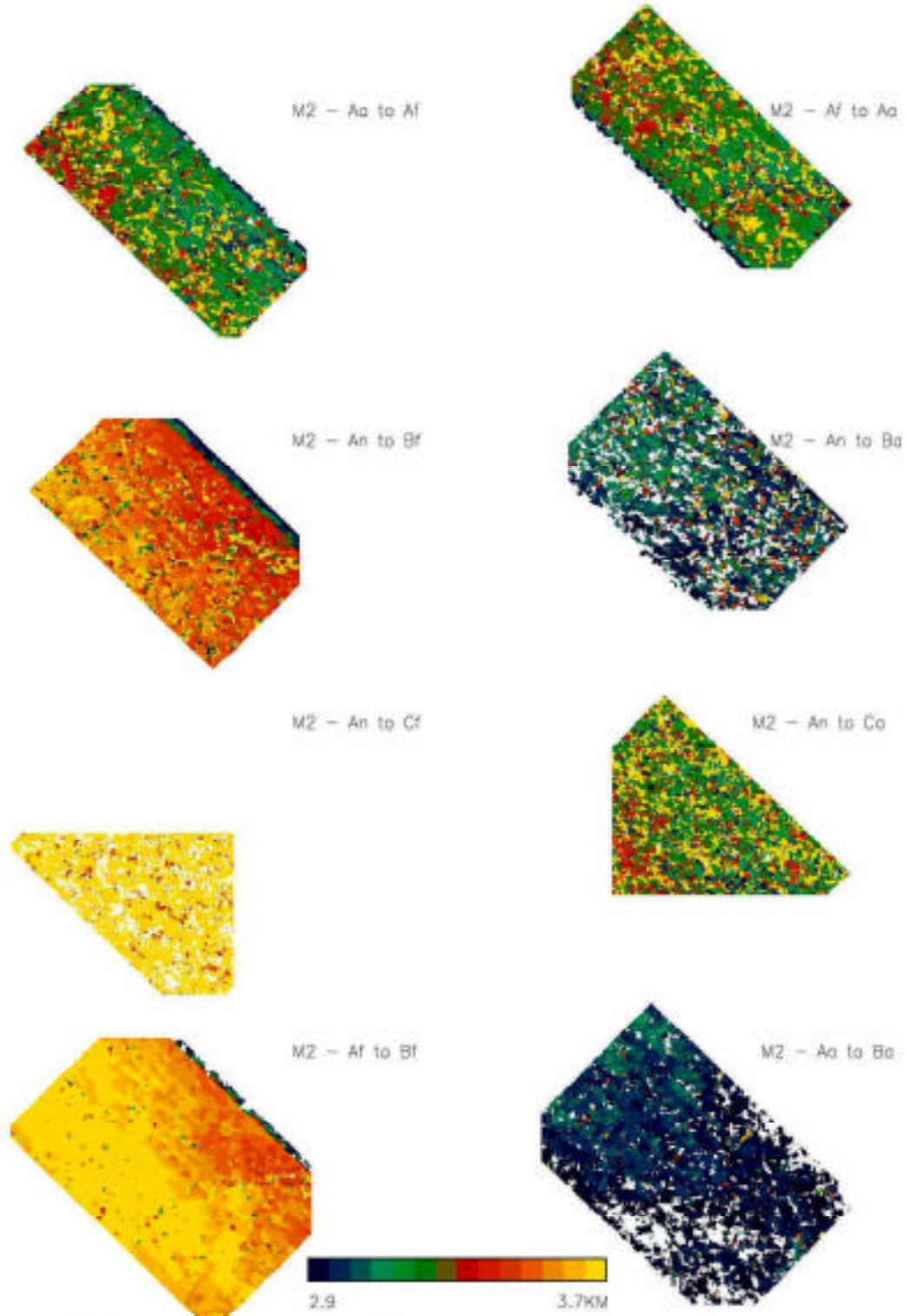


Figure 75. Stereo-matched heights from the A and B forward and after cameras showing the bias in the forward CTHs wrt the aft ones.

Stereo measurements of CBH using Fish-eye lens stereo CCD imagery

Owing to the large change in contrast and brightness between the images due in some part to the lack of a sun occulter, stereo matching experiments with these images were not successful. Results from an inter-comparison of Cloud Base Heights determined from the stereo-pair and the results from the Chilbolton radar at the time of the ATSR2 overpass are discussed in section 3.5.1.2.

DLR-IPE

Initial experience with Cloud-to-Cloud Matching

With the exception of desert areas MOMS image strips generally do contain cloudy areas. This is because there is a time lag of several days between mission decision and mission operation.

In most cases the central parts of optically thick cloud are saturated, since the MOMS gain factors are set for surface imaging. Cloud top height CTH can hence not be inferred for the saturated parts of the MOMS cloud scenes (central parts of clouds).

However, border regions of individual clouds are generally non-saturated and suitable for manual and machined stereo matching.

The derived height values are closer to cloud base height CBT (the meteorological important cloud condensation level) than to CTH.

No special problems arise for manual matching of clouds besides the blocking effect of complex multi-layer cloud fields.

Automated surface matching algorithms can be applied for matching single layer cumulus cloud fields (the dominating case). However, problems arise for machine vision matching of complex multi-layer cloud fields, since these algorithms assume a continuous surface without blocking.

Matching of two stereo channels is often complicated by large differences of the optical thickness of clouds (BRDF-variance).

This problem is much reduced for matching of one (selected) stereo channel with the Nadir view direction by selecting either the (optically thick) blue channel, or the (optically thin) Near Infrared channel as a partner (or even a weighted combination of both channels).

Initial experience with Shadow Matching

At the high spatial resolution of MOMS the border regions of cloud shadows show in most case a gradient of intensity with internal structures of the cloud border region. For that reason, cloud to shadow matching can be performed (in most cases) with algorithms based on area matching and must not be confined to matching of border lines.

However, cloud shadows are generally stronger (optically thicker) than the image of the corresponding cloud, since shadows are caused by the strong (and dominating) forward scattering of the solar irradiation, and the cloud images by the weaker side- or backward scattering in the direction of the spaceborne observation.

Shadow to cloud matching is hence performed in an indirect way, correlating the (best visible) shadow of the NIR channel 4 with the optically most dense cloud image of the other channels.

Cloud to shadow matching is most straightforward over sea. Interference of cloud (and cloud shadow) structure with surface structure over land leads to a larger scatter of the estimated displacement vectors over land.

Machine shadow to cloud matching must be based on inverted images for a proper representation of the shadow areas. For convenience, inverted images are also used to analyse the shadow drift.

The software for matching of stereo images of the Earth surface and for digital terrain modelling is not ideally suited to working with clouds. Cloud image processing quite often requires parameter settings far off from the established values of surface image processing. Experience with new settings accumulates only slowly by some "trial and error procedure".

There is also some lack of suitable visualisation tools for the results of cloud data processing.

The half year delay of the reorganisation of the DLR contribution to CLOUDMAP caused some delay for the PE/OE contribution to be compensated in the remaining time span of the project.

Initial experience with contrail and cirrus matching

Interestingly, MOMS images of contrails show, that the internal structure of persisting contrails (the dominating case of MOMS images with contrails) is stable enough in time to allow stereo matching (also) in the contrail direction.

In some cases contrails cast a clearly discernible shadow with internal structure, allowing to match the contrail with its shadow (also) in the contrail direction.

Cirrus clouds can be matched only over sea. Automated surface matching algorithms can not cope with matching Cirrus clouds over land. In this case even manual matching is difficult (leading to a large variance of estimated positions for the reason, that the operator is expecting flat structures, whereas real Cirrus clouds can have a dominating vertical extension). This problem demonstrates the necessity of the special effort set by DLR Berlin (H. Hetzheim) to base Cirrus to land surface separation on texture modelling.

ETH

No value-added products produced and distributed to partners.

DLR-IPA

Creation of contrail climatology over Europe

An analysis tool to derive averages of contrail cloudiness from large sets of remapped contrail masks was developed. It aims to derive the radiative impact of contrails. The handling of false alarm rate and detection efficiency for the production of contrail coverage data was changed substantially, as it showed up in the data, that not only the detection efficiency but also the false alarm rate depends on the thermal inhomogeneity of the underlying surface. Details of this work will soon be published within the thesis of R. Meyer.

Examples with 2 years of data have been shown in the First CLOUDMAP interim report. The results will be combined into meaningful datasets when 5 years (1995-1999) of processed night and daytime data are available.

Creation of contrail climatology over non-European areas

Work for SE Asia and Japan started. We envisage a dataset represented by the mid-season months of one year including NOAA-14 night overpasses. Results are not yet available.

FUB

Cloud optical thickness regression error

The regression calculates the coefficients for each combination of solar and observational angles and surface albedo on the basis of radiances simulated for a number of cases according to realistic statistics. The root mean square error of the optical thickness regression is defined as the sum of the squared deviations between the “true” optical thickness and the optical thickness calculated with the polynomial expression using the coefficients divided by the number N of simulated cases used for the regression. The RMSEs are calculated in parallel to the regression process and stored in separate data bases with the same angular resolution as the regression coefficients. Similar to the coefficient selection, the RMSEs of a cloudy MOS pixel can be extracted using the pixel value for the sun zenith angle, viewing zenith angle and the azimuthal difference as well as the surface albedo.

As an example, **Figure 76** shows an example of this product addition: the regression error estimated for each pixel as a root mean square error (RMSE). The image in **Figure 77** is the radiance at MOS channel 9, from which the cloud optical thickness (**Error! Reference source not found.**) is derived.

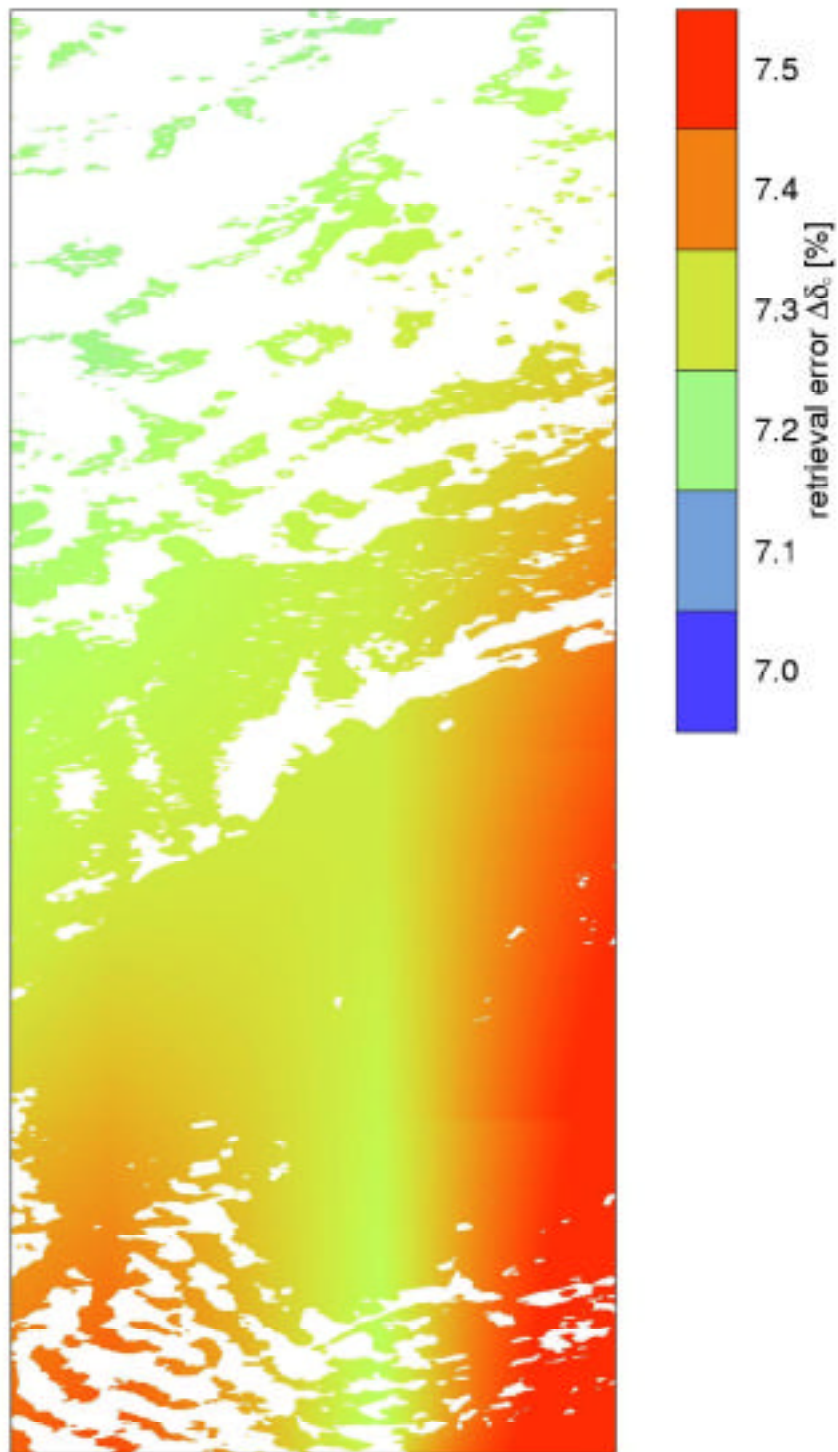


Figure 76: cloud optical thickness retrieval error in percent

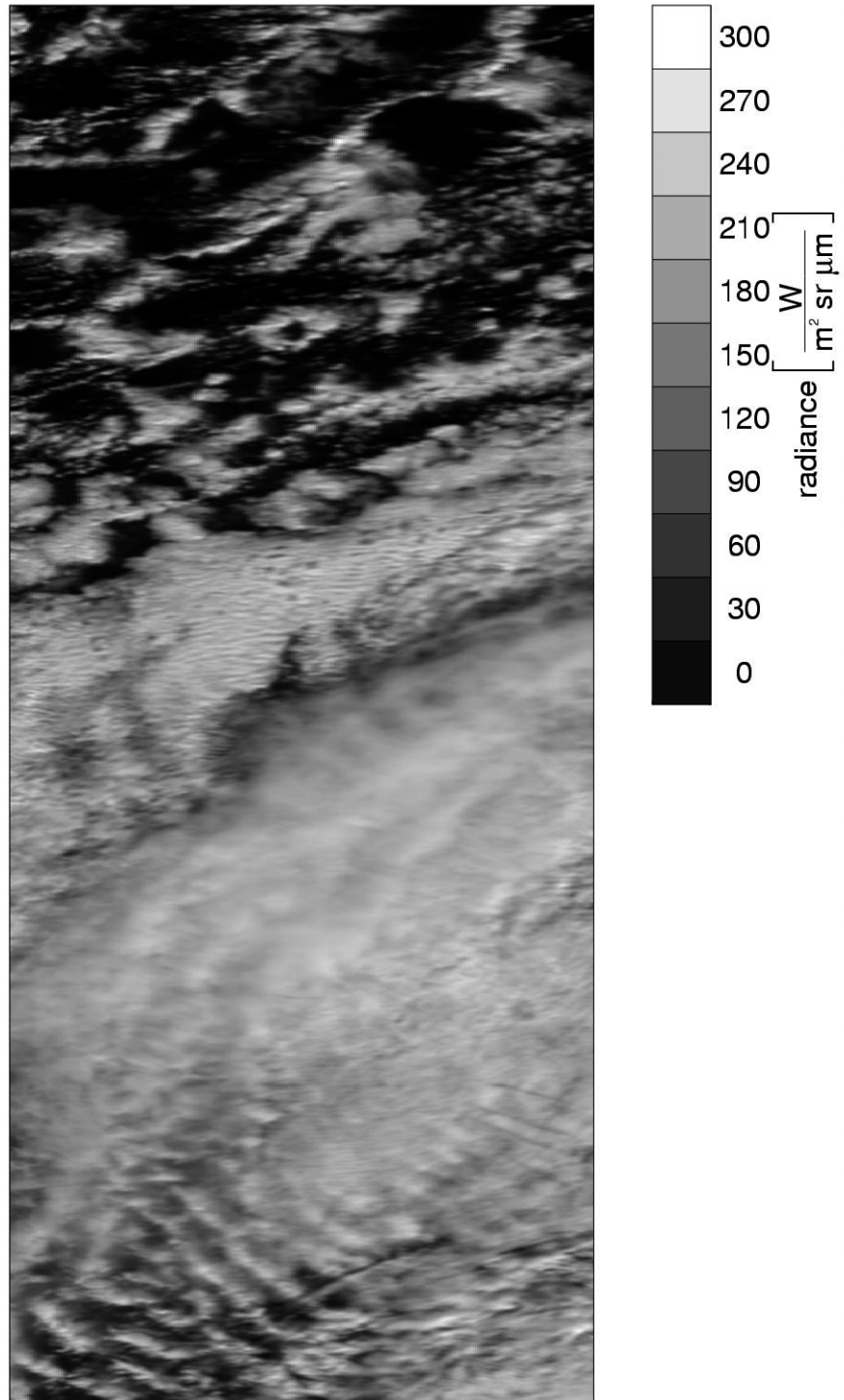


Figure 77: MOS radiance in channel 9 at 750nm

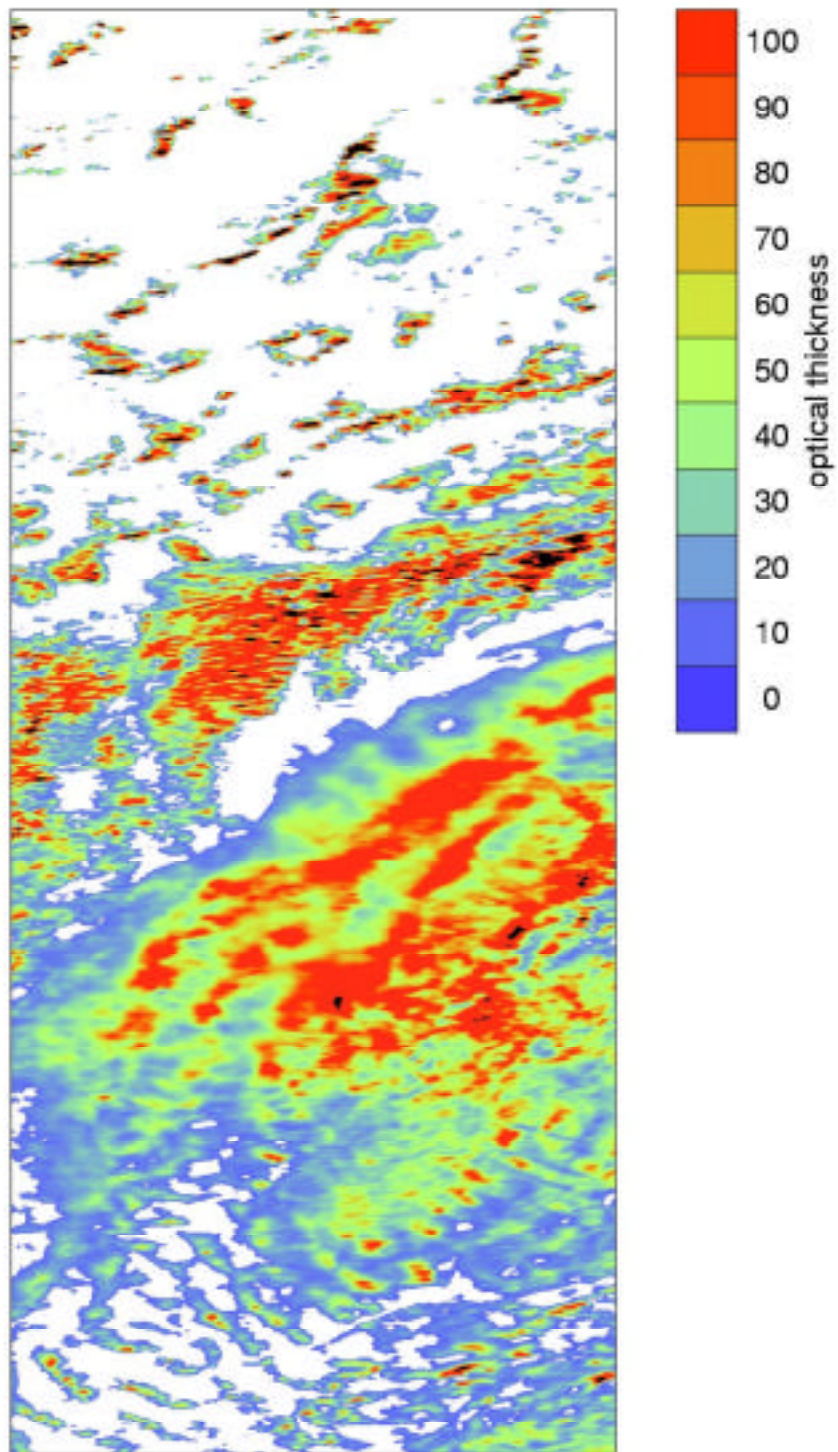


Figure 79: Retrieved cloud optical thickness

Validation and scientific evaluation of products

UCL

Comparison of ATSR2 CTHs with Chilbolton radar

A small window of 12 pixels were extracted from the CTH arrays from 23.10.98 around the Chilbolton radar site, the location of which is shown in **Figure 28** of section 3.4.1.1. This indicates a great deal of scatter of heights due to the broken and multi-level nature of the clouds. Taking the time of overpass and the radar reflectivity browse products from the Chilbolton 35GHz and the GKSS 94 GHz radars shown in **Figure 31**, the heights of the cloud-top heights were compared between those from ATSR2 stereo-CTHs and those from radars. The radars indicate high-level clouds around 10km which is consistent with the stereo-ATSR2 observations, albeit somewhat higher (11.5km)

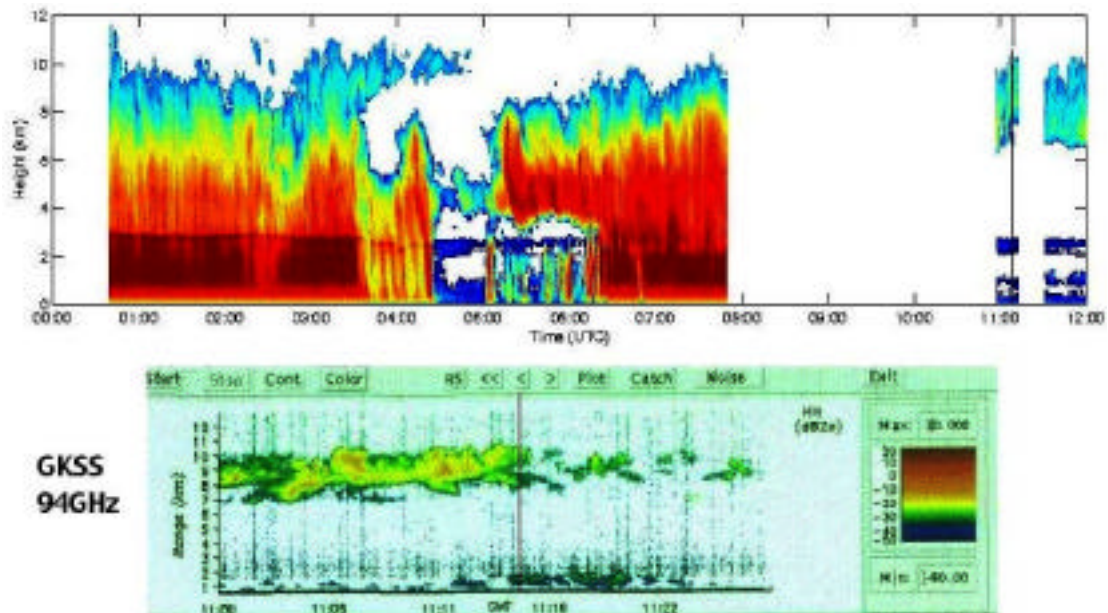


Figure 80. Browse products of the Chilbolton 35GHz (top) and GKSS 94 GHz (bottom) radars showing radar reflectivity in dBs for 23.10.98. A visual inspection indicates a CTH around 1km.

Similar results were produced for the 10th and 16th October 1998 but at the time of writing no quick-look browse images were available.

Comparison of ground-based CBH with Chilbolton radar

The wide angle digital images discussed in section 3.4.1.3 were calibrated using the camera calibration facility in the Department of Geomatic Engineering at UCL to obtain a precise interior and exterior orientation.

This allowed manual measurements to be made using in-house stereo Digital Photogrammetric tools. Using location information on the cameras and the zenith pointing 35GHz radar at Chilbolton it was possible to calculate the location of the

pierce point in the digital camera sensor array. Interactive manual stereo visual measurements were then employed to calculate the cloud base height.

Figure 32 shows a stereo-pair acquired at 11:14Z on 23/10/98 taken coincident with the ATSR2 overpass. **Figure 32** shows a cross superimposed on the 2 images to indicate the position of the pierce point. The Cloud Base Height was calculated as 1.2km at the pierce point compared with approximately 1km calculated from the 35Ghz and 94Ghz radars (see **Figure 14** in section 3.5.1.1).

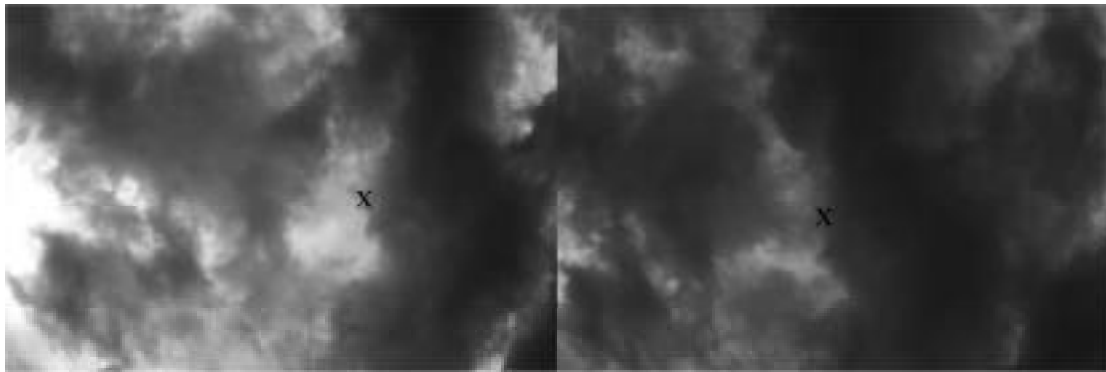


Figure 81. Stereo-pair of Kodak Megaplex camera images acquired at 11:14Z at the time of the ATSR2 overpass

These results suggest that ground-based stereo visible imagers can be used for daytime validation of cloud-base height from mm-radar if and only if the problem of camera synchronisation, solar occulters and variable contrast can be properly addressed. UCL decided to focus its efforts in the last year on other methods of validation and in particular to study the potential of the Chilbolton radar for validation with as many of the ATSR2 stereo-pairs as possible and their inter-comparison with results from the MOS data. ETH continued to address the issue concerned with stereo visible digital camera validation of cloud-base heights (see section 3.5.3).

Comparison of AirMISR CTHs with airborne lidar and ground-based mm-radar

An independent evaluation of the M2 stereo matcher as well as the complete NASA AirMISR processing chain developed at JPL based on the M2 matcher was undertaken by Dr Roger Marchand of Pennsylvania State University [Marchand *et al.*, 2000].

The first step in the AirMISR stereo-height retrieval is to identify common features between image pairs. The MISR approach uses a number of stereo matchers (principally M2 described in section 3.3.1.1.1, M3 which uses medians rather than means and Rank Sort) as well as a variable search window. The search window restricts the size of the target image where a matching feature is sought. If one uses a small search window centered on the correct point in the target image, one is unlikely to misalign the features and of course the retrieval works much faster.

The AirMISR images shown in Figure 9 in section 3.2.1.5 were matched using both the M2 matcher and the full AirMISR processing chain. The heights were then calculated using the approach described in 3.3.1.2. These heights were then compared

against a ground-based 35GHz radar (not shown here) and the NASA Goddard Space Flight Center Cloud Lidar System (CLS) which was being flown on board the ER-2 alongside AirMISR.

Figure 33 compares the AirMISR stereo-derived cloud top heights along the ER-2 ground track, with those measured by the lidar. In this figure, the height retrieval using both the full MISR algorithm and M2 are included.

Figure 33 shows that the lidar and complete MISR algorithm compare very favorably (well within the estimated 500 meter uncertainty). This cloud scene shows little variability in the cloud top and part of the reason the full algorithm works well in this example is that the search window is reduced in size such that it is unlikely that a poor match will be found. Without the reduced search window the matcher still works well using only the M2 matcher with a large search window. However, a number of blunders (or incorrect matches) were encountered. (All those points that do not lie near the lidar cloud top height are blunders caused by incorrect image matching). Many, but not all, of these blunders are detected as blunder by the AirMISR processing chain. software.

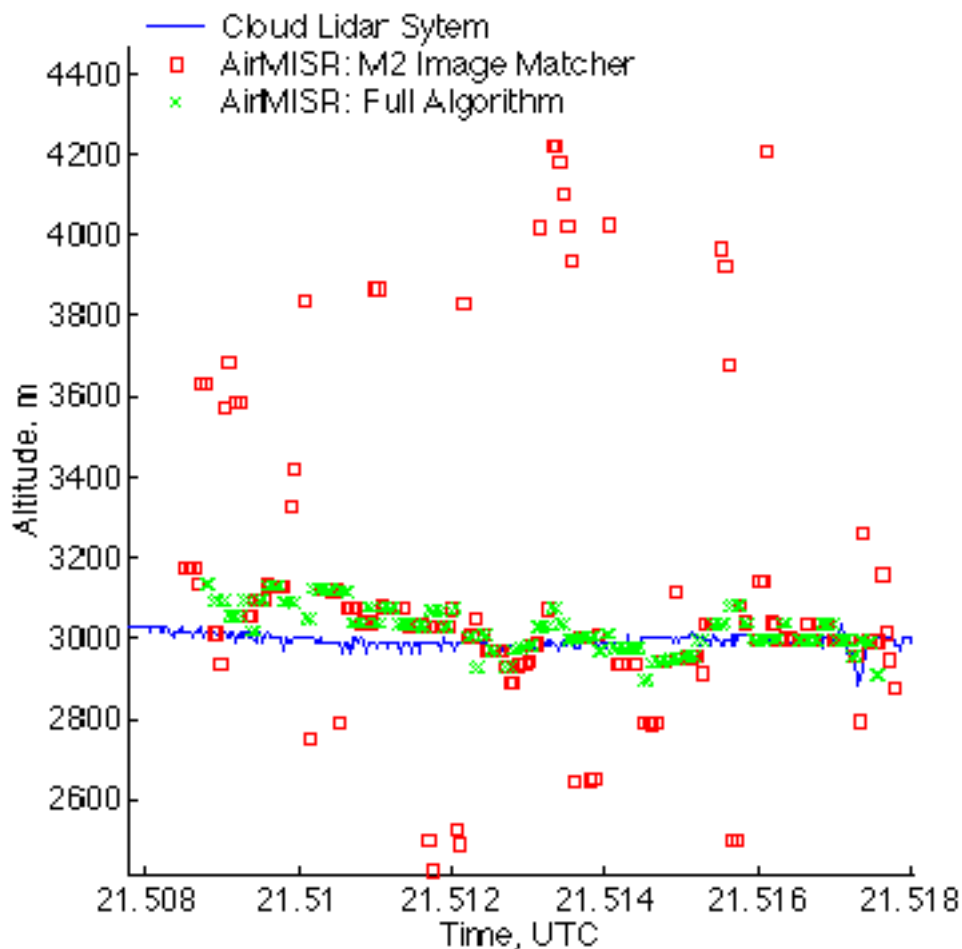


Figure 82. Comparison of stereo-retrieved cloud top height and ER-2 Cloud Lidar System measured cloud top height. Stereo-based results are shown with both the full AirMISR algorithm and M2.

DLR-IPE

Validation Plan for the last period

The following cloud parameters can be derived from MOMS stereo images:

- cross track component of the Shadow Drift Velocity SDVct,
- along track component of the Shadow Drift Velocity SDVat,
- cross track component of the Cloud Drift Velocity CDVct,
- apparent Cloud Base Height CBHa (systematic error proportional to CDVct),
- apparent Cloud Top Height CTHa (systematic error proportional to CDVct),
- true Cloud Base Height CBHt (SDVat-corrected),
- true Cloud Top Height CTHt (SDVat-corrected).

The along track component of the Cloud Drift Velocity CDVat can not be defined from the stereo images of clouds. The CDVat will be replaced by the corresponding shadow drift component SDVat, assuming, that vertical movements of the clouds can be neglected.

The accuracy and reliability of the MOMS high resolution cloud data products can be verified only by a consistency checks and statistical analysis for selected sets of observation conditions.

Mean values of cloud base and top height and of cloud drift vectors derived for larger cloud fields will be compared with contemporaneous data of meteorological satellites and synopsis.

The shadow analysis of MOMS stereo scenes under development at DLR-IPE is assumed to be more accurate than the combined ATSR/MOS-A or MISR/MOS-A method. So validation of the shadow procedure can be accomplished only from a statistical analysis of sufficient data as planned by DLR-IPE towards the end of the project and/or by independent ground based cameras or LIDAR. This independent data must be provided by the CLOUDMAP project. Details of an appropriate work plan are under definition.

ETH

Validation Plan for the last period

Up until now, there are no coincidences between the period acquisition of MOMS and ATRS2 images.

The cloud top heights estimated from these high resolution images will be further used as reference data for matching of re-sampled MOMS images at a resolution of 288 m. In fact the stereo satellite sensors which can be used for cloud-top height estimation often have a resolution in the 250 - 1000 m range.

As ATSR2 measures in 7 spectral bands (0.55, 0.67, 0.87, 1.6, 3.7, 11, 12 microns), the results from the different channels (and of arithmetic combinations thereof) will be compared and analysed. The aim is to detect which channels are more suitable for

cloud detection and to model multilayer clouds, i.e. depending on the cloud type, some clouds are detected well in some channels while they become transparent in other ones, thus permitting modelling of lower clouds.

The results during the MAP-SOP, both satellite-based and ground-based, will be validated by very frequent (3h) radiosonde ascents over the inner alpine region, lidars, cloud observations, very-shortrange weather forecast products and various airplane flights. If coincident MOS overflights occur, they will also be compared to cloud-top heights derived using the Oxygen A-Band.

In addition, the accuracy of the results will be checked with stereo visualisation using digital photogrammetric workstations.

DLR-IPA

Contrail detection False Alarm Rate

The false alarm rate (FAR) of the contrail detection algorithm was better defined. A tool for visual inspection and classification of automatically detected contrails was programmed and applied to datasets with very low contrail coverage over New Zealand. Each object classified as contrail was interactively analysed and confirmed or rejected. FAR reached 0.1 % in the investigated region.

Validation plans for the last period

From October 1997 onward the DWD (German Weatherservice) recorded visual contrail observations with the routine SYNOP observations. It is planned to compare these data to the results of the automated contrail detection algorithm.

In close co-operation with ETHZ we will try to obtain useful sky camera stereo pairs for the validation of contrail coverage and the detection efficiency of the algorithm. If a reasonable amount of ATSR scenes can be processed for contrails the derived average contrail coverage will be compared to values derived from AVHRR for the same area.

DLR-IST

It is planned that validation will be carried out in collaboration with DLR-IPA.

FUB

Comparison of MOS Cloud-top Pressure with radiosonde data

Thirty MOS scenes of the year 1996 over land and ocean surfaces were selected with coincident radio sounding data, where a) an inversion layer was clearly visible and b) the location of the radio sounding was cloudy. The MOS overpass time and the radiosounding launch was up to 4h apart. Radiosounding data is very useful for the validation of the cloud top pressure algorithm, since it has been shown that a strong decrease of relative humidity above a layer of high relative humidity is strongly correlated to a cloud top, if clouds are occurring. (Chernykh and Eskridge, 1996). The altitudes of the inversion levels have been compared with cloud top pressures from MOS images. The cloud top pressure has been calculated in a region of approximately 30 km surrounding of the location of the radiosounding. In Figure 83 the

profile of the dew point temperature and the temperature measured by a radiosonde for a specific case is shown. The layer of nearly 100% relative humidity between 700 hPa and 520 hPa is clearly seen. At 520 hPa the relative humidity decreases rapidly, which is an indication of a cloud top. On the right hand side of Figure 83 the corresponding histogram of the retrieved cloud top pressures is shown.

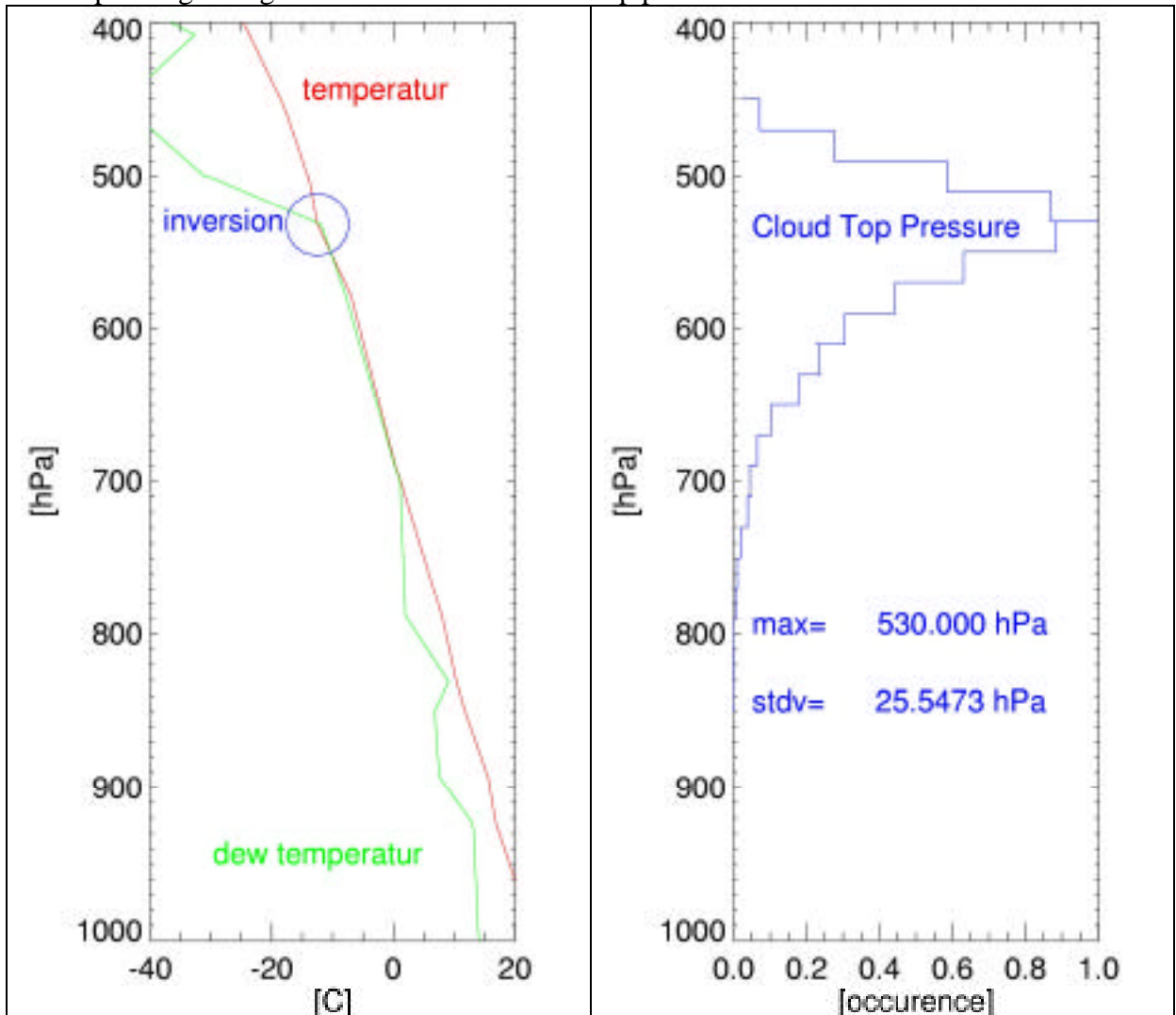


Figure 83: The profile of the dew point temperature and the temperature measured by a radio sond for a specific case (left). On the right hand side the corresponding histogram of the retrieved cloud top pressures is shown

In Figure 84 the retrieved cloud top pressures and the corresponding inversion pressures of all cases are shown. The red points are values where the radiosounding was within the MOS track, the gray points are values, where the radiosounding was close to but not within the MOS track. The Y error bars are the standard deviation of retrieved cloud top pressures within the surrounding area. The X error bar was set to 30 hPa for radiosoundings within the MOS track and to 90 hPa for sounding outside the MOS track. The accuracy obtained from this validation is within the predicted values of 30hPa, although a small BIAS of 10 hPa was found. One reason is that clouds can have a cloud top above the inversion due to the dynamic nature of the updraft region.

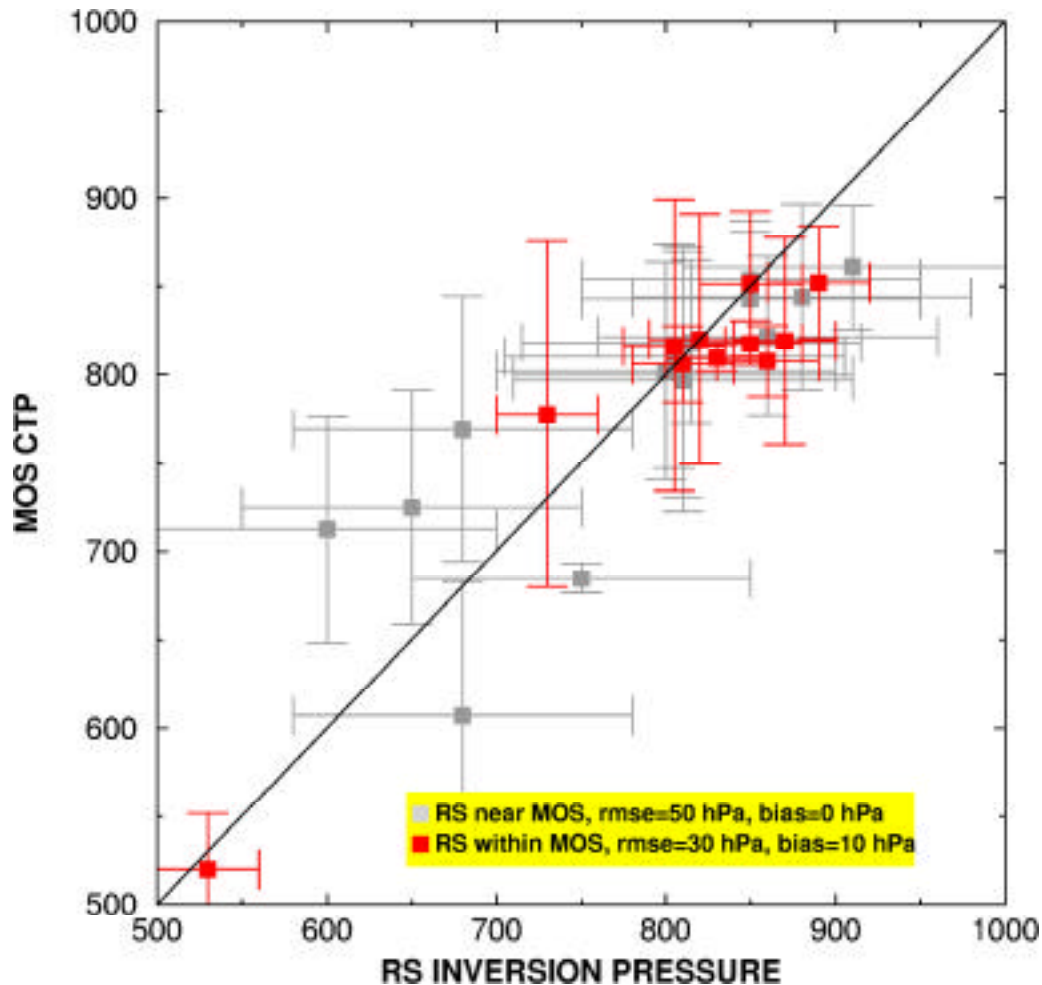


Figure 84: The retrieved cloud top pressures and the corresponding inversion pressures of all cases. The red points are values where the radiosounding was within the MOS track, the gray points are values, where the radiosounding was close to but not within the MOS track.

Validation of cloud droplet concentration

Two scenes with stratocumulus field in the North Atlantic region, recorded on different days (04.03.98 and 24.03.98) were selected to test the new MOS products for cloud microphysical properties. From radiances measured by MOS-A, MOS-C and the MOS-B module, optical thickness, cloud top pressure, effective radius and droplet concentration has been calculated. Most of the pixel show optical thicknesses lower than 10 (**Figure 85** and **Figure 86**).

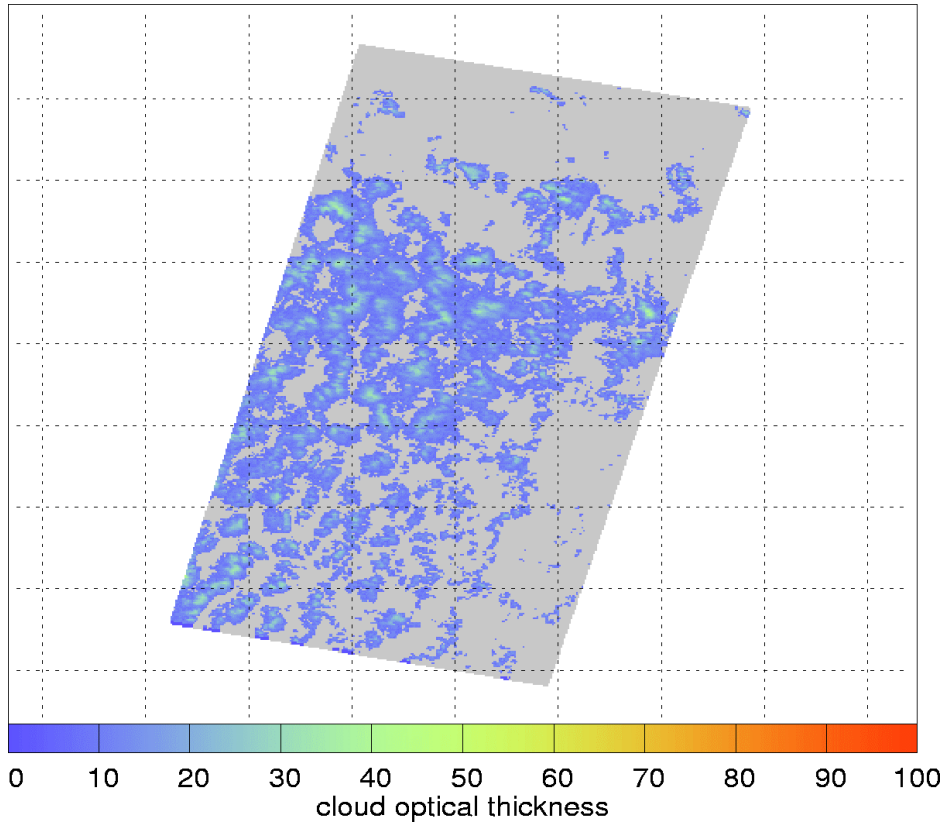


Figure 85: Retrieved optical thickness from MOS image recorded at March, 4th 1998

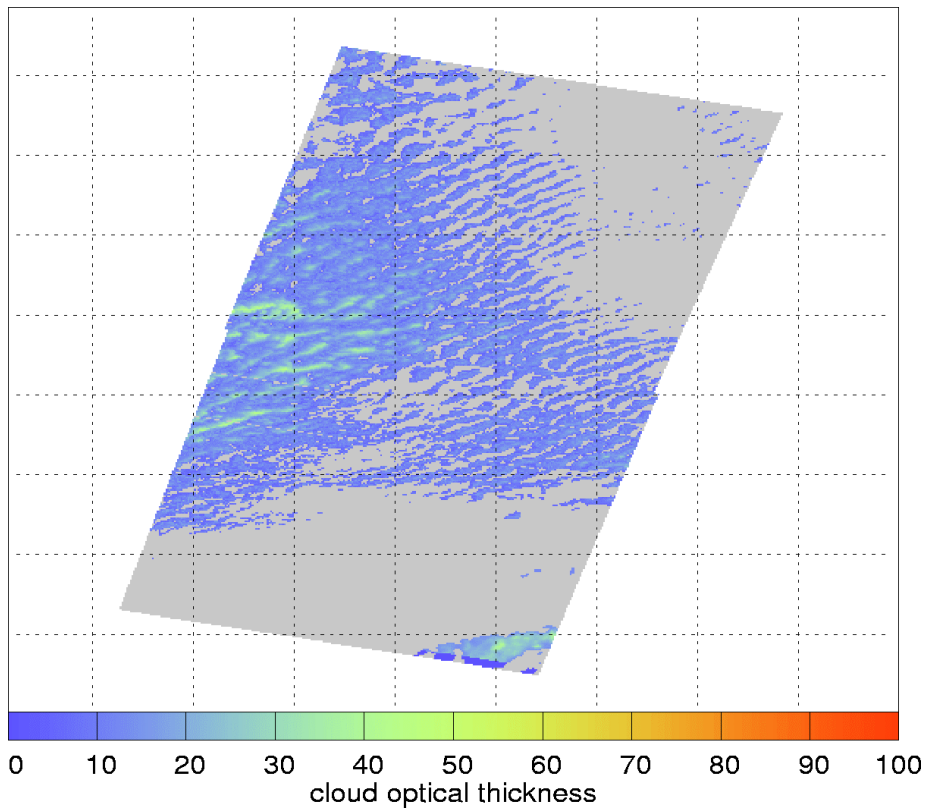


Figure 86: Retrieved optical thickness from MOS image recorded at March, 24th 1998

The pressure at cloud top is larger than 750hPa (**Figure 87** and

). Obviously, the observed clouds are low level optically thin clouds. This distinction is important, since the algorithm to derive cloud droplet concentration can only be applied to such kind of clouds.

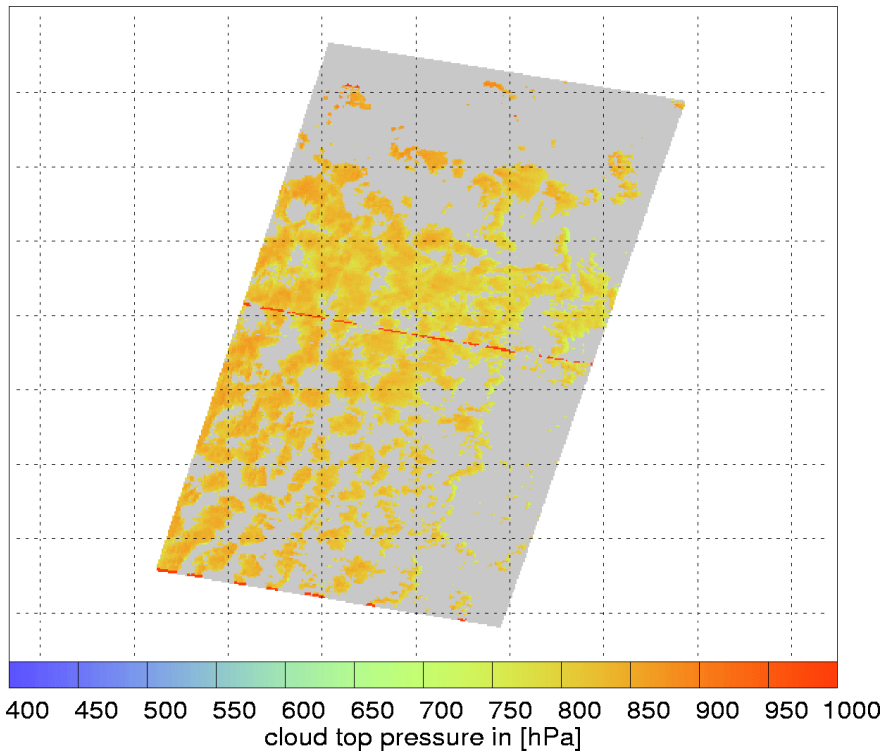


Figure 87: Retrieved cloud top pressure from MOS image recorded at March, 4th 1998

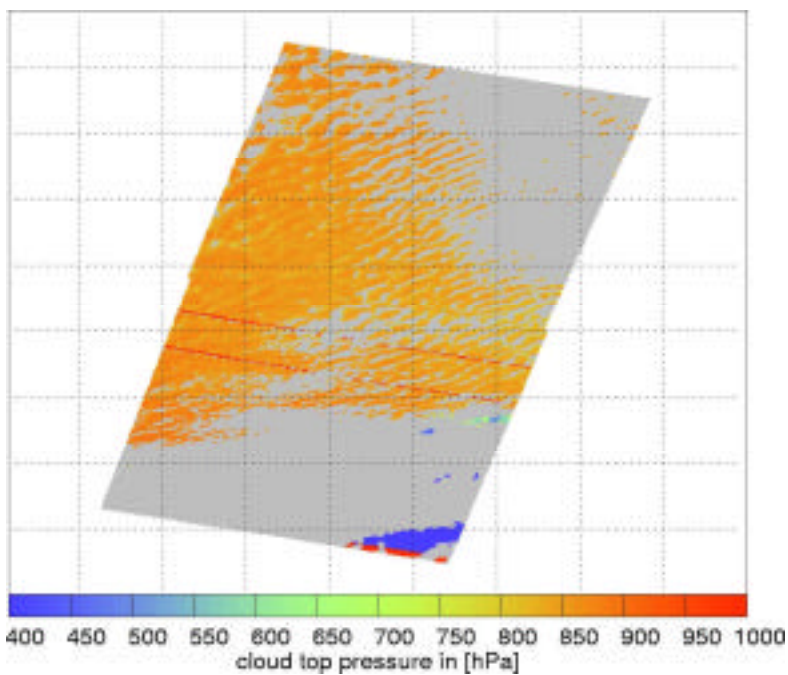


Figure 88: Retrieved cloud top pressure from MOS image recorded at March, 24th 1998

The result of the cloud effective radius derivation (**Figure 89** and

) show only slight differences between the two cases. The values are with in $9\mu\text{m}$ to $15\mu\text{m}$ with larger droplets at March, 4th.

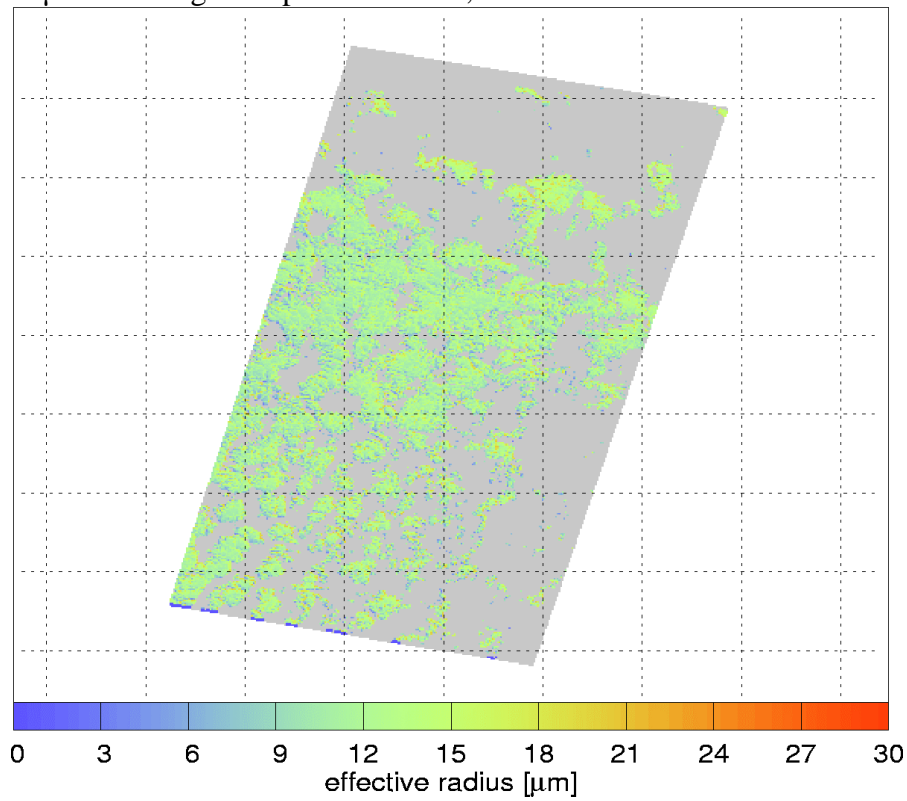


Figure 89: Retrieved effective radius from MOS image recorded at March, 4th 1998

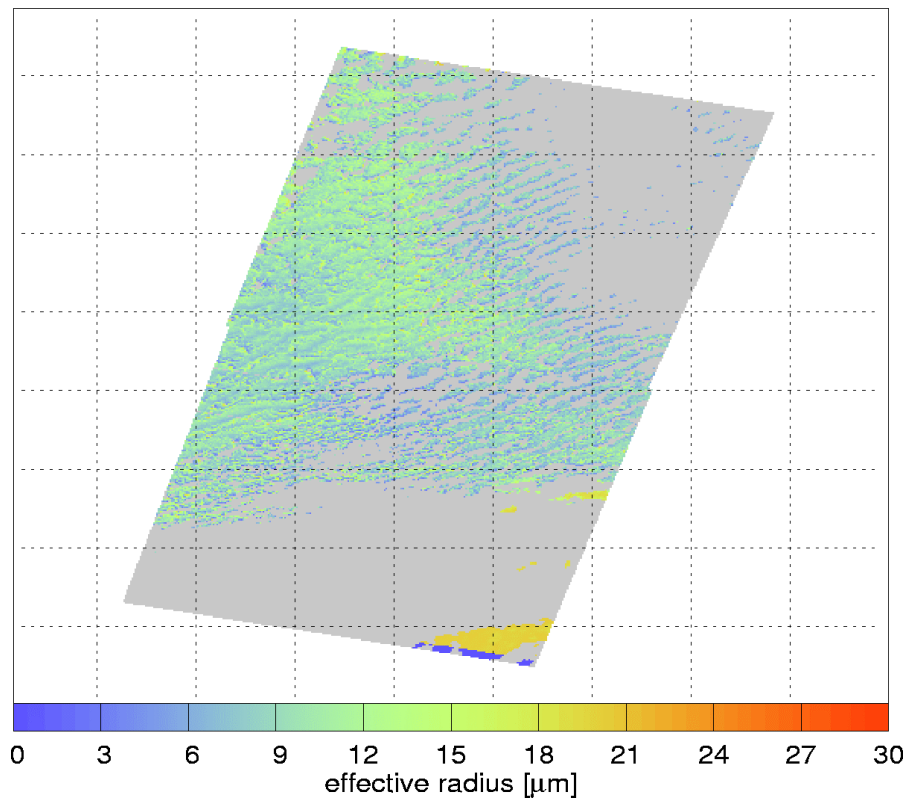


Figure 90: Retrieved effective radius from MOS image recorded at March, 24th 1998

In contrast, the derived droplet concentration (**Figure 91** and **Error! Reference source not found.**) is significantly higher by a factor 5 in the 24.03.1998 case. This confirms the findings of the analysis of OVID data recorded during the ACE 2 campaign (see CLOUDMAP First Annual Report), that the remotely sensed droplet concentration can indicate modification of cloud microphysical structure due to pollution (indirect aerosol effect on climate).

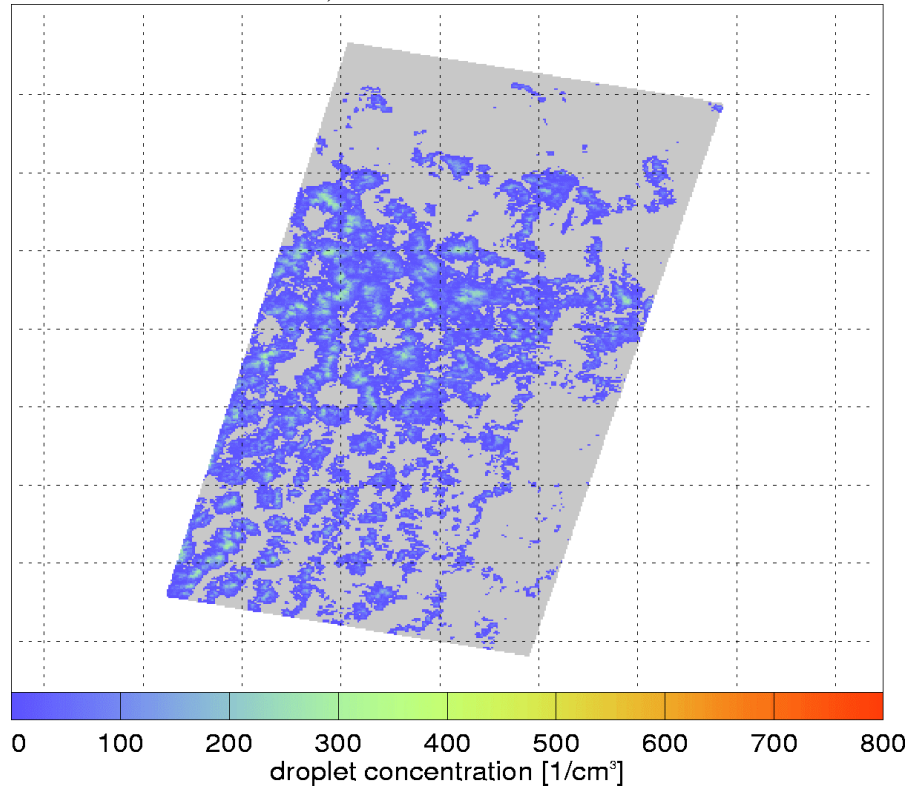


Figure 91: Retrieved droplet concentration from MOS image recorded at March, 4th 1998

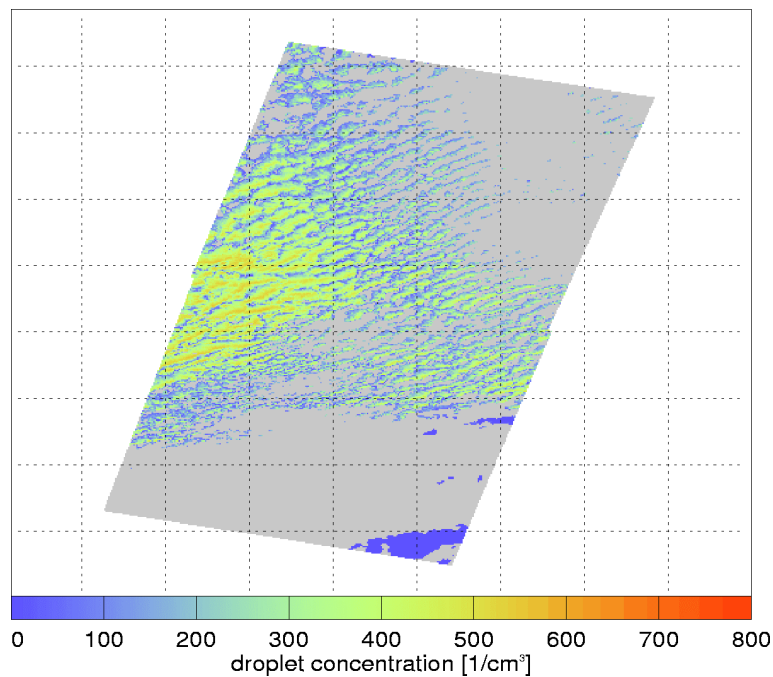
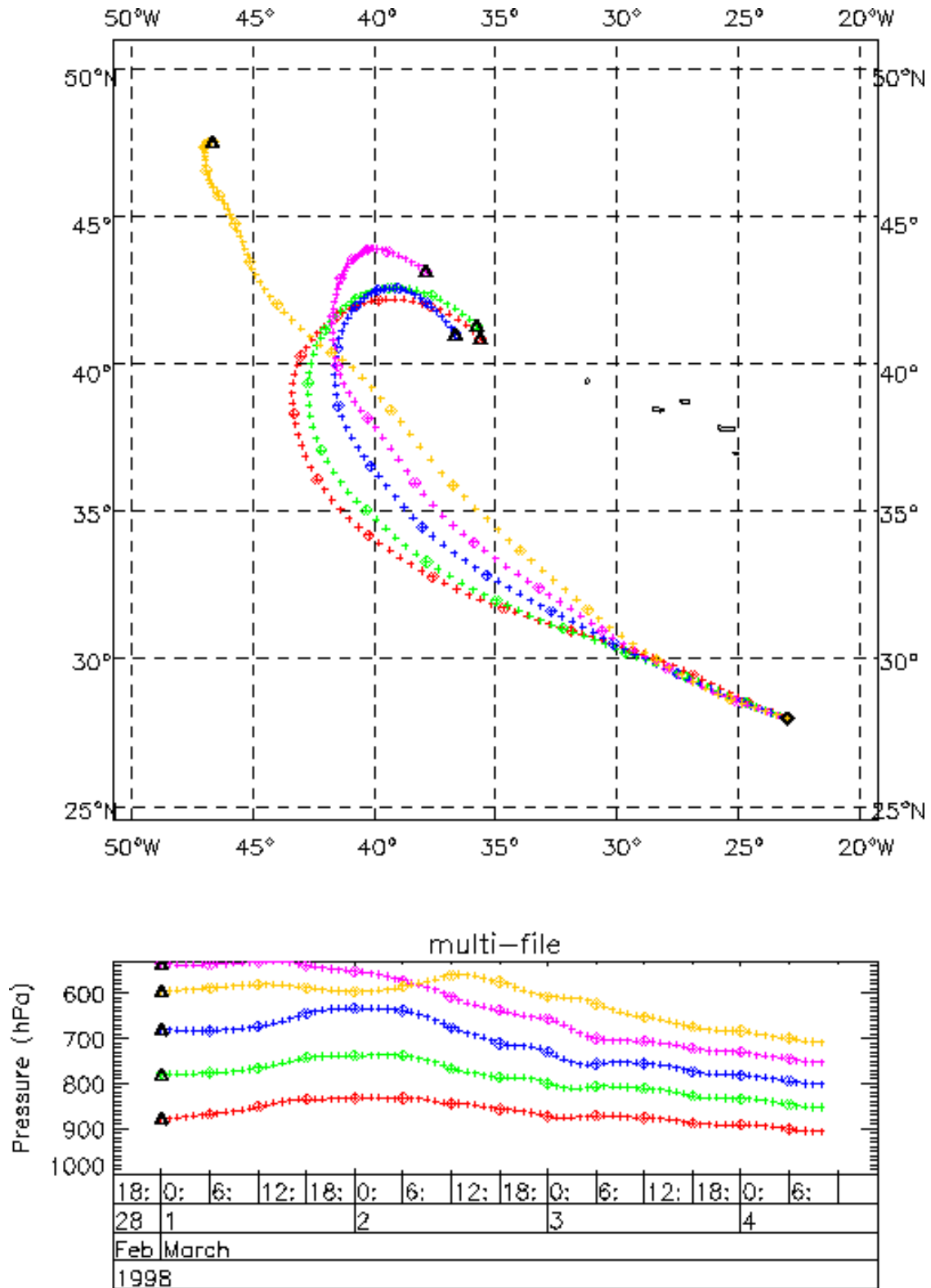


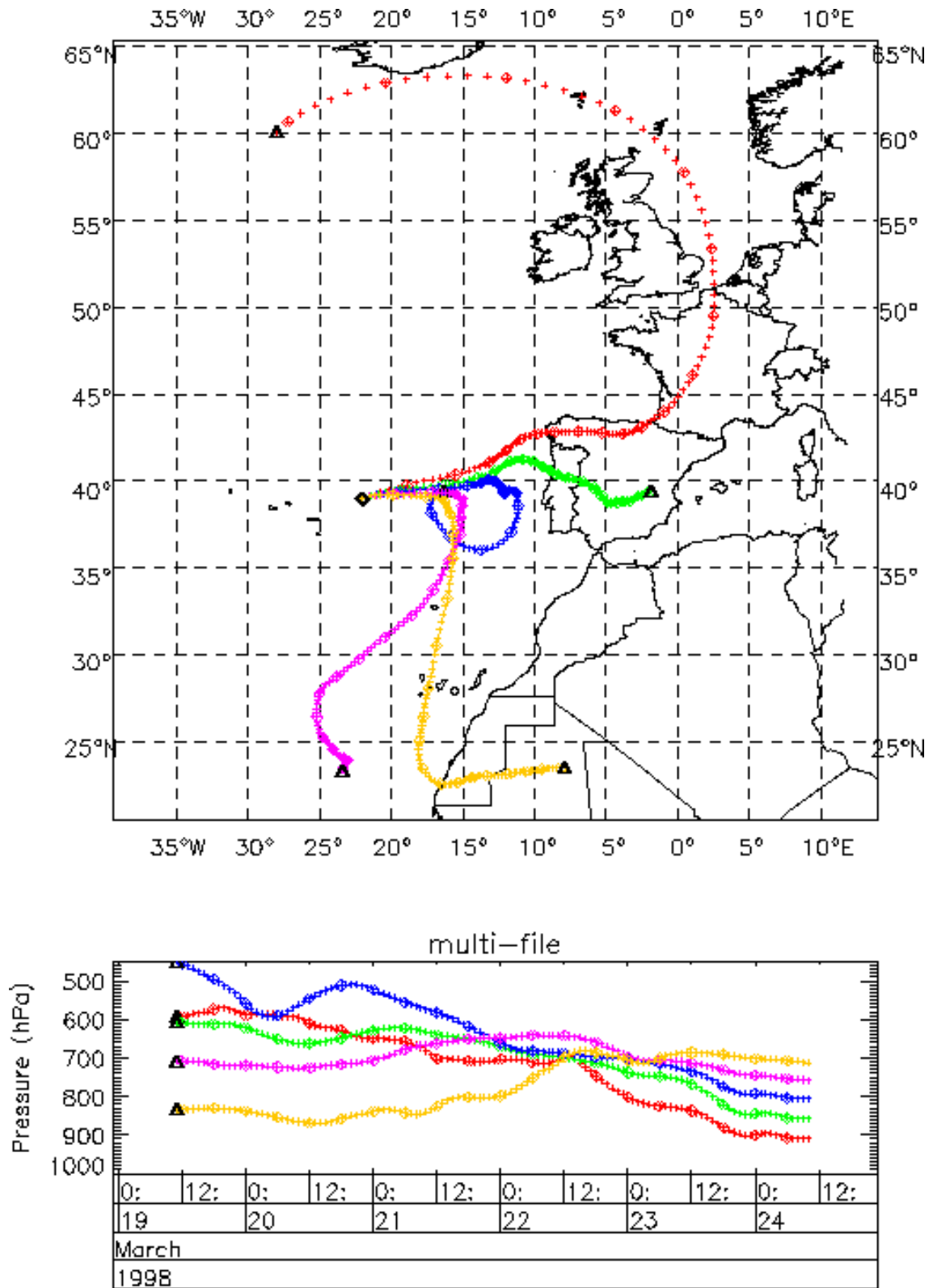
Figure 93: Retrieved droplet concentration from MOS image recorded at March, 24th 1998

Surface weather analysis maps were analysed to identify the origin of the airmasses in which the observed clouds developed. Indeed, the cloud with a low droplet concentration was within a clean maritime airmass, whereas the airmass of the cloud with a high droplet concentration is likely to be polluted, since the air was drawn over the European continent into the observational area. A more precise method to determine the origin of airmasses is the back-calculation of trajectories. **Figure 94** and **Error! Reference source not found.** are the trajectories calculated for the two observation days. Only the trajectory at March 24th at cloud top pressure touches areas of pollution sources (Northern France and Spain). This result demonstrates, that it is possible to observe and investigate the so-called Twomey-Effect with MOS using the combination of different retrieval procedures. It is planned to expand this study to use all available MOS data for the region of interest and to link the remote sensing results to further back-trajectory calculations and to in situ measurements of aerosol on the Izana site at Tenerife Island. A new MOS algorithm is under development, which estimates the integrated shortwave albedo from MOS-A,B and C channels. This would enable us to determine a regional indirect forcing of aerosols due to pollution using MOS data.



file: 980304.ps

Figure 94: Back trajectories from March, 4th 1998



file: 980324.ps

Figure 96: Back trajectories from March, 24th 1998

Departures from Workplan

The failure of the MIR SPECTR module which included BALKAN and the MOMS instrument restricted the use of the latter data and eliminated the supply of the former. The lack of useable non-saturated 3-line imagery over clouds from WAAC eliminated the use of this sensor.

Consequently significant effort was shifted from DLR-IPE to DLR-IPA to focus on generating a longer term contrail climatology from AVHRR, developing a contrail detector for ATSR2 and generating a comparison contrail dataset for the Asia-Pacific region to compare against that derived for Europe.

The delays in the launch of the NASA EOS Terra spacecraft until the end of 1999 changed the emphasis to the use of the AirMISR airborne MISR simulator.

The problems of getting synchronised ground-based wide-angle stereo imagery by UCL switched their efforts onto validation of CLOUDMAP products which was of more central importance to the end users at KNMI.

The delay in the start of ETH's (non-EU) funded efforts switched their emphasis onto looking at developing a more robust ground-based wide-angle stereo imagery based cloud-base height estimation system.

Preliminary Conclusion

Progress towards project objectives

Significant progress was made in defining the requirements of climate modellers through a workshop held at the EGS99 conference in The Hague in April 1999 for CLOUDMAP products and preliminary ATSR2 and MOS products were supplied to KNMI for their own internal evaluation using independent ground-based lidar and radar data.

Significant progress has also been made in developing a processing chain for stereo cloud-top retrieval using ATSR2 and AirMISR as well as Oxygen A-band cloud-top pressure retrieval from MOMS and microphysical products from MOS. Significant progress has also been made in developing camera models for MOMS and stereo cloud-top height retrievals from MOMS.

Significant progress was also made in processing a five year climatological record of AVHRR-derived contrail detection as well as in the development of research algorithms for contrail and cirrus detection based on fuzzy integrals. Significant progress has also been made in modification of the AVHRR contrail detection algorithm for ATSR2.

No progress has been made in METEOSAT or GOES data collection or in the development of automated motion algorithms for geostationary satellite data.

Significant progress has been made in the development of a prototype system for the use of ground-based radars for cloud-top height validation and examples have been demonstrated for a cloud campaign in the Netherlands (CLARA96) and a combined ground-based and airborne campaign in the UK (CLARE98). Significant progress has also been made in the use of radiosonde measurements for cloud-top pressure measurements from MOS. Significant progress has also been made in validating cloud droplet concentration retrieval from MOS using back-calculation of Langrangian tracers which demonstrated the Twomey effect associated with polluted air-masses.

Significant progress has been made in the use of ground-based visible digital cameras for the retrieval of cloud-base information through the innovative use of GPS-synchronised shuttering within the Swiss MAP campaign. Less progress has been made on reducing these data into usable products.

The continuing delay in the launch of the NASA EOS Terra mission has resulted in a shift of emphasis from MISR and MODIS to the use of AirMISR.

Implications for the final period

A substantial effort is required to create more CLOUDMAP products for use by KNMI in their own internal evaluation and for KNMI to get independent assessments of these cloud-top products from other national meteorological agencies. It is planned that UCL will develop a set of example products from ATSR2 and MOS and validation from the Chilbolton radar. This will take the form of a web-page as part of the general CLOUDMAP web-page and include statistics of the CTHs derived from ATSR2 stereo and brightness temperature, MOS (where available and coincident) and the Chilbolton mm-radar (see <http://www.ge.ucl.ac.uk/research/CLOUDMAP.html>).

A roadshow is planned towards the end of the final period at several national meteorological agencies. This will include an analysis of whether the CLOUDMAP products address future user requirements and an on-line questionnaire will be developed in association with the web-page to provide detailed feedback on the CLOUDMAP products.

If the NASA EOS Terra launch goes ahead as planned in December 1999, substantial effort will be directed at UCL to an early evaluation of the MISR stereo CTHs with and without the wind effect removed. This will also include an initial evaluation of CTHs derived from MODIS using the CO2 slicing technique which will be used with the SEVIRI instrument onboard METEOSAT Second Generation geostationary satellite due for launch in 2000/2001.

Emphasis in the final period will be on a quantitative validation of CLOUDMAP products particularly from ATSR2 and MOS using both radiosondes and ground-based radar and lidar at the Chilbolton radar facility. Evaluations will also be carried out of automated wind field retrieval using METEOSAT rapid-scan stereo during the MAP campaign.

Finally, development of methods will continue on improving the accuracy, reliability and speed of the stereo ATSR2 processing and completing the AVHRR-derived

contrail climatology over Europe and Asia.

References cited

Beyer, H.A. Accurate calibration of CCD-cameras. Proc. IEEE Conf. on Computer Vision and Pattern Recognition, Champaign, Illinois, June 1992, pp 96-101, 1992

Chernykh, I.V., Eskridge, R.E. Determination of cloud amount and level from radiosonde soundings. J. Appl. Meteor. 35:1362-1369, 1969.

Hetzheim, H. Using Martingale Representation to Adapt Models for Non-Linear Filtering, Proceedings of ICSP'93, International Academic Publ. , Beijing , pp.32-35, 1993.

Hetzheim, H. Anwendung der Fuzzy-Logic in der Bildverarbeitung, Vision Jahrbuch '93, Sprechsaal Pub., Coburg 1993, pp. 47-53, 1993

Kratky, V. Rigorous photogrammetric processing of SPOT images at CCM Canada. ISPRS Journal of Photogrammetry and Remote Sensing, 44:53-71, 1989

Mannstein, H., R. Meyer and P. Wendling: Operational detection of contrails from NOAA-AVHRR-data. Int. J. Remote Sensing, Vol. 20, No 8, 1641-1660, 1999

Meyer, R. H. Mannstein and P. Wendling: Contrail coverage of Western Europe from 2 years of NOAA-AVHRR data, Proc of "The Conference on Satellite Meteorology and Oceanography", Paris, May 25-29 1998, AMS and EUMETSAT, p 266-269, 1998

Minnis, P., D. F. Young, D. P. Garber, L. Nguyen, W. L. Smith and R. Palikonda: Transformation of contrails into cirrus during SUCCESS, Geophys. Res. Letters, 25/8:1157-1160, 1998

Marchand, R.T., T. Ackerman, C. Moroney, and J.-P. Muller, Multiangle Observations of Arctic Clouds from FIRE ACE: June 3, 1998 Case Study., *J. Geophys. Res., in press*, 2000

Muller, J.-P., R. Dundas, and D. Bower, An automated processing system for cloud-top height and amount from ATSR(2) stereo., in *International workshop on Applications of the ERS Along Track Scanning Radiometer.*, ESA, 23 - 25 June 1999, ESRIN, Frascati, Italy, 1999

Nelder and Mead. Computer Journal Vol.7 pp.308-313, 1988.

Palikonda, R., P. Minnis, D.R. Doelling, P.W. Heck, H. Mannstein and U. Schumann: Potential radiative impact of contrail coverage over continental USA estimated from AVHRR data. In Conference on Atmospheric radiation, AMS, 1999

Prata, A.J., and P.J. Turner, Cloud-top height determination using ATSR data, *Rem. Sens. Env.*, 59 (1), 1-13, 1997.

Sugeno, M. Theory of fuzzy integrals and its application, Doctoral Thesis, Tokyo Institute of Technology, 1974.

Annex A: report on the 2nd CLOUDMAP User Workshop

Date: April 21, 1999

Venue: Congresgebouw, Den Haag, The Netherlands

Participants list:

<i>Name and affiliation:</i>	<i>E-mail address:</i>	<i>Initials:</i>
Dr. Gary J. Robinson (ESSC, UK)	gazza@mail.nerc-essc.ac.uk	GR
Lubomir Sdukup (Utia,Cas,Cr)	soukup@utia.cas.cz	LS
Dr. Stephen Bakan (MPI für Meteorologie)	bakan@dkrz.de	SB
Dr. Tomas Halenka(Dept of Meteorology, Charles University)	tomas.halenka@mff.cuni.cz	TH
Dr. David Chappell (ESSC, UK)	darc@mail.nerc-essc.ac.uk	DC
Dr. K. Pfeilsticker (UNI-HD, De)	klaus.pfeilsticker@ iup.uni-heidelberg.de	KP
Dr. Irina Melnikova (Uni. of Tokyo)	irina@ccsr.u-tokyo.ac.jp (irina.melnikova@pobox.spbu.2u)	IM

CLOUDMAP partners (present at workshop):

<i>Name and affiliation:</i>	<i>E-mail address:</i>	<i>Initials:</i>
Jan-Peter Muller (UCL)	jpmuller@ge.ucl.ac.uk	PM
Hans Roozekrans (KNMI)	roozekra@knmi.nl	HR
Paul de Valk (KNMI)	valkde@knmi.nl	PV
Hermann Mannstein (DLR-IPA) HM	Hermann.Mannstein@dlr.de	
Hartwig Hetzheim (DLR-IST)	Hartwig.Hetzheim@dlr.de	HH
Rene Preusker (FUB)	rene@amor.met.fu-berlin.de	RP
Lothar Schueller (FUB) LSc	lothar@amor.met.fu-berlin.de	
Armin Drescher (DLR-IPE)	armin.drescher@dlr.de	AD

Setting and scope of workshop:

The second user workshop of the CLOUDMAP project was held in Den Haag. The venue was chosen as it coincided with the EGS 24th general assembly. Part of the workshop programme was scheduled as part of Symposium AO30 with the title "Use of satellite data in climate studies". The dedicated CLOUDMAP paper session was scheduled at the end of the day.

After the paper session and a small break (with some snacks and drinks) the real part of the workshop, an interactive discussion with users, was held.

The first CLOUDMAP user workshop, held during the AMS/EUMETSAT Conference in Paris at the end of May 1998, was focused mostly on the use of satellite cloud data in nowcasting and numerical weather prediction modelling. This second workshop was more focused, in line with the setting, on the use in climate

research. The aim of the paper part of the workshop was to inform the audience on the work done in the CLOUDMAP project. The aim of the discussion part was to get feedback from the audience on their opinion on the use of satellite cloud data in climate studies in general and of CLOUDMAP products in particular.

Programme of workshop:

- 17.00 *J.P. Muller*: CLOUDMAP evaluation of new macroscopic and microphysical cloud parameters from earth observation sensors for climate modelling.
- 17.15 *A. Drescher, B. Schreiner*: Application of high resolution MOMS/MIR data for CLOUDMAP validation.
- 17.30 *H. Mannstein, R. Meyer*: Automated contrail detection from AVHRR data.
- 17.45 *H. Hetzheim*: Mathematical theory and algorithms for detection of contrails.
- 18.00 *L. Schueller, R. Preusker, J. Fischer*: Retrieval of cloud optical and microphysical parameters from spaceborn imaging systems (MOS and MERIS).
- 18.15 *R. Preusker, L. Schueller, J. Fischer*: Cloud top height retrieval from measurements within the O2A band with the satellite imaging sensors MOS and MERIS.
- 18.30 Break
- 19.00 Discussion
- 20.00 Close of workshop

Report of discussion:

The discussion was guided by a 12 statements given with the aim to provoke discussion.

1. *Satellite data ↔ other data*

Are satellite data of clouds more useful than other data sources for application to climate research?

GR:Global coverage of satellite data is very helpful but the major problem is the calibration of the data on the long term.

Satellite data start to get useful for climate studies at time scales of a decade or more.

Satellite data can be useful to study the diurnal variation of clouds.

SB: It depends on the time scales under study.

HM:In the long term contrail study of DLR a NOAA satellite change always introduces sensitivity problems.

IM:Measurements in narrow spectral bands are required, this facilitates parametrization of models.

Information on day to day variability but also vertical profile information obtained by aircrafts can be useful for climate research.

AD:Spatial resolution is very much related to radiometric accuracy.

2: *Need for independent data*

Do climate researchers require satellite cloud products which are independent of additional (e.g. NWP model, synops, etc.) data sources?

GR:Yes, keep it as clean as possible! Cross-correlation of data sources is a big problem in climate research.

HM:Independent data sources are useful to control model results.

3: Operational satellites

Are the present and future operational satellite cloud data sets (METEOSAT, MSG, NOAA) sufficient for use in climate research (eg ISCCP data set)?

GR: The big problem with the operational satellites is the calibration of data and products. The temporal resolution of the NOAA-AVHRR (3 hr) is sufficient.

SB: The quantity of the data in terms of spatial and temporal resolution is sufficient. However, the quality of the derived data sets is not sufficient. We have to realise that different climate research subjects have different demands.

4: Experimental satellites

Do cloud data derived from experimental satellites (ERS, MOS, ENVISAT, EOS, ADEOS, etc.) have potential scientific value when used in climate research?

GR: Yes!

SB: The value is evident for case studies. For process studies they only have value if the calibration of data is stable for 10 years or more. Equal quality of data for 50 years would be a big step forward.

PM: We have to set realistic goals, no satellite programme has long term continuity funding.

5: How to increase satellite data use

What is the priority order for increasing the use of satellite data in climate research?:

- better horizontal resolution,
- better vertical resolution,
- better temporal resolution.

IM: Again this depends on the scope of the research (e.g. temporal resolution has priority if the scope is to study the diurnal cycle). The priority is also related to its contribution to solve the calibration problem (which is the main drawback for use of satellite data in climate research).

GR: The highest priority should be set to data continuity for the purpose to create longer time series.

SB: First we have to assess in which way we make optimal use of satellite data:
-in a climate model,
-direct assimilation of observed cloud top radiances in a model,
-optimise the analysis for climate research,
-create long term consistent radiance data sets.

6: Cloud top height

Is cloud top height (CTH) information important in climate research?

If so, for which application? Which parameter has priority?:

- cloud top height (meter)
- cloud top pressure (hPa)
- cloud top temperature (K)

SB: CTH can be used to estimate the convection strength and associated rain intensity.

GR: CTH can be useful for validation of models.

The choice of parameter does not matter because they are strongly related to each other.

Do you see the clouds move?

PM: Yes, but not when the clouds move in the along track direction.

7: Cloud type

Is cloud type information relevant for climate research?

If so, in which way should cloud types be classified?:

-traditionally

-based on physical characteristics of a cloud (phase, optical depth, etc)

GR: Yes, both ways.

SB: Is this relevant for climatology studies? Clouds have a variable appearance, this 3D variability affects the radiation field.

The question arises how much information is required to obtain significant climatological parameters?

8: Contrails

What is the role and potential of information on contrails for climate research?

-parameterization of climate models?

-impact of aviation induced cloudiness on the greenhouse effect?

SB: The effect of contrails is quite well known: they change to cirrus or processed contrails. Coverage of contrails is sufficiently known. Still there are some unclear questions

9: Cloud particle size

Is cloud particle size distribution important for climate research?

If so, for which application(s)?

GR: This is fundamental information, in order to distinguish clouds from aerosols and its effect on radiation processes.

SB: The cloud particle size distribution has an important effect on radiation transport. It enables to distinguish between old contrails and cirrus.

10: Cloud optical thickness/geometrical thickness

Is cloud optical depth and/or thickness important for climate research?

If so, for which application(s)?

GR: Yes, optical thickness is very relevant for radiation transport models.

11: Cloud top phase

Is cloud top particle phase important for climate research?

If so, for which application(s)?

GR: Yes, this parameter is relevant; see 10

12: Polar vs geostationary

Are polar orbiting satellites relevant for climate research?

GR: They are both required as they are complementary, which is a necessary evil.

SB: Information about the ice coverage at the poles is most relevant for climate research.

Concluding remarks

Probably due to the very unfavourable time of day, the number of climate researchers participating in the workshop discussion was rather low. Nevertheless, the output of the workshop can be considered as very valuable for the CLOUDMAP project. The excellence of the participants resulted in a few very clear conclusions on the usefulness of satellite derived cloud information in general and of the CLOUDMAP products in particular:

- For the purpose of process studies, climate research badly needs long time series of unambiguous data of cloud parameters. The operational meteorological satellite programmes provide this long term data continuity. Therefore, the focus in climate studies is very much set to the use of the World Weather Watch satellites (METEOSAT, GOES, TIROS, etc.). However, the unambiguous calibration of the sensors on board of these satellites still forms a large drawback of their use in climate studies. CLOUDMAP products might help to derive better calibration of meteorological satellite data.
- The CLOUDMAP products provide helpful information for a better understanding of the role of clouds in global climate change that still is very much unclear. Independent information on cloud top height and optical thickness (the main CLOUDMAP products) is very useful and valuable to improve the cloud parameterisation in climate models.

The CLOUDMAP project partners would like to thank all participants for their valuable contributions to the workshop and the EGS Congress organisation for hosting the workshop.